THE UNIVERSITY of ADELAIDE

Starbursts and Star-forming Galaxies as the sources of Cosmic Neutrinos measured by the IceCube Neutrino Observatory

Alexander Luke Kyriacou
B.Sc. (Honours), Physics

A thesis submitted to the University of Adelaide in fulfilment of the requirements for the degree of Master of Philosophy

School of Physical Sciences,
Department of Physics,

March, 2018

Acknowledgements

It has been a long road and I have been lucky enough to have had good guidance along the way. Foremost I would like to thank my supervisors Gary Hill and Bruce Dawson for providing direction, guidance and constant support over the last two and a half years, and for giving feedback on this thesis. I also owe a special debt to Benjamin Whelan and Mark Aartsen, who jointly built the code infrastructure upon which I constructed my analysis and were an invaluable help whenever it came to programming or general technical issues.

I have been very privileged to have been a part of the Adelaide High Energy Astrophysics Group. I have had great company over the last two and a half years and want to thank my office mates Sally Robertson, Natasha Atkins, Alex Wallace, Mark Aartsen, Luke Biggins and Brayden Pullen.

None of this research would have been possible without the hard work of my fellow "IceCubers", from the Point Source Analysis Group to the researchers at Aachen University who simulated the muon-neutrino events I used for my analysis to the people who built the detector and keep it running.

Finally I would like to thank all my family and friends, especially my mother Alison, my father Steve and my sister Stephanie for supporting me throughout this whole time and encouraging my studies.

Declaration of Originality

I, Alexander Kyriacou, certify that this work contains no material which has been accepted for the award of any degree or diploma in any university or tertiary institution and, to the best of my knowledge, contains no material previously published or written by another person except where due reference has been made in the text. Additionally, I certify that no part of this work shall in the future be used in a submission of any other degree or diploma in any institution without the prior approval of the University of Adelaide and, where applicable, any partner institution responsible for the joint-award of this degree.

I give consent to this copy of my thesis, when deposited in the University Library, being made available for loan and photocopying, subject to the provisions of the Copyright Act of 1968.

I also give permission for the digital version of my thesis to be made available on the internet via the University's digital research repository, the Library catalogue and also through web search engines, unless the University has placed restrictions on access for a period of time.

Signed: _____

Alexander Kyriacou

Abstract

The origin of the astrophysical neutrino flux detected by the IceCube Neutrino Observatory remains unknown. Numerous analyses have attempted to distinguish point sources in the arrival direction data. To date no significant point sources have been discovered. The isotropic distribution of high energy neutrinos suggests that the neutrinos are extra-galactic in origin. Additionally the measurements of the energy spectrum and flavour composition suggest that the neutrinos are produced in the interactions of high energy cosmic rays with surrounding gas and background radiation. Among the most likely proposed sources of neutrinos are starburst galaxies, galaxies with a star-formation rate at least an order of magnitude above that of a normal star-forming galaxy like the Milky Way. The enhanced star-formation rate correlates with enhanced rates of supernovae and gamma-ray bursts, which produced cosmic rays, as well as dense gas and ambient radiation, making them ideal locations for cosmic ray interactions. Such cosmic ray interactions should also produce high energy γ-ray emission that may be useful in guiding our search for neutrino sources.

In this thesis we examine the hypothesis that starburst galaxies produce the majority of the astrophysical neutrino flux in two principal ways. First we derive an upper limit on neutrino emission per starburst galaxy using local infra-red and γ-ray emission, and sum the predicted emission over the co-moving starburst number density up to a red-shift of $z_{max} = 5$. The estimated energy flux is highly sensitive to the assumed spectral index and the assumption of hadronic γ-ray production. We find that only for a very hard spectral index $\Gamma \sim 2$ could starburst galaxies produce the majority of the neutrino flux at $E > 100$TeV. Such a hard spectral index is disfavoured by most analyses of the IceCube diffuse flux and measurements of high energy γ-rays in local starburst galaxies M82 and NGC 253. Additionally, under this scenario the majority of the flux would originate in distant sources ($z \sim 2$), with only $\sim 2\%$ of the flux produced in the local Universe ($D < 200\,\mathrm{Mpc}$).

The second method is to search directly for a neutrino signal originating from nearby starburst galaxies which would manifest as clustering of neutrino arrival directions around the positions of the brightest starbursts. We implement a stacked point source analysis, using the positions of starburst galaxies in the IRAS Revised Bright Sample to define the locations of point source while using their infra-red emission to weight the sources assuming a spectral index of $\Gamma = 2$. We measured the sensitivity of the analysis to a collective point source flux distributed amongst the IRAS starburst galaxies. We find that our analysis is sensitive to a point source energy flux of $E^2 d\Phi_{\nu,SB}/dE = 3 \times 10^{-12}\,\mathrm{TeVcm^{-2}s^{-1}}$ at a confidence level of 90%. This corresponds to around 3.2% of the astrophysical neutrino flux associated with local starburst galaxies in the IRAS Revised Bright Sample, slightly above the value of the theoretical upper limit ($\sim 2\%$) found in chapter 6.

We find that the analysis is sensitive to the neutrino flux of starburst galaxies only under the most optimistic assumptions of a hard starburst spectral index $\Gamma \sim 2$ and near 100% correspondence of neutrinos to γ-rays ($\nu/\gamma \sim 1$). Overall we find it unlikely that starburst galaxies produce the majority of the astrophysical neutrino flux and conclude that we only expect to distinguish a starburst signal with our point source analysis if starbursts did account for the majority of the flux. However the analysis sensitivity may improve with increased statistics from later neutrino data sets obtained by IceCube.

Contents

Chapter 1

Neutrino Physics

1.1 History

Neutrinos (represented with the Greek letter ν) are fundamental particles of the Standard Model and is the second most Standard Model particle after the photon. Neutrinos belong to the lepton family and come in three flavours associated with the electron (ν_e), muon (ν_μ) and the tau particle or tauon (ν_τ). Neutrinos have no interaction wvia the electromagnetic or strong forces, interacting only via the weak force and gravity. Since they have infinitesimal but finite mass ($m_\nu \ll m_e$) it is the weak force that makes their detection possible.

The existence of neutrinos was postulated by Wolfgang Pauli in 1930 to preserve conservation of energy, momentum and spin in β-decay. He dubbed this new particle the "neutron" (not to be confused with the current neutron) and hypothesized that this particle was ejected from the nucleus together with the electron or positive β-particle [69]. In 1932 James Chadwick discovered a more massive neutral particle inside the nucleus and also named it neutron, although it was not clear at the time that the two particles with the same name were distinct from one another. The name "neutrino" was coined by Enrico Fermi in 1932, coming from the Italian for "little neutral one". In 1934 Fermi introduced a model of β-decay which united Pauli's neutrino with Dirac's positron and Heisenberg's neutron-proton model. Fermi's theory described the process by which a neutron could decay to a proton by ejecting an electron and anti-neutrino.

$$n \rightarrow p^+ + e^- + \bar{\nu_e} \tag{1.1}$$

Pauli lamented that he had discovered a particle whose existence could never be confirmed experimentally. However only 22 years later neutrinos were measured in a nuclear reactor in the famous Cowan-Reines experiment [74]. Anti-neutrinos produced via nuclear fission reacted with protons in a water tank adjacent to the reactor, producing positrons which annihilated with surrounding electrons to produce γ-rays that were measured. Additionally the neutrons produced in the β-decay were absorbed by cadmium which then decayed to its ground state, emitting γ-rays.

$$\nu + p^+ \rightarrow n + e^+ \tag{1.2}$$

$$n + {}^{108}\mathrm{Cd} \rightarrow {}^{109m}\mathrm{Cd} \rightarrow {}^{109}\mathrm{Cd} + \gamma \tag{1.3}$$

1.2 Neutrinos in the Standard Model

The Standard Model is a theory which seeks to explain all physical phenomena, excluding gravity, through the interaction of twelve fermions, four gauge bosons and the Higgs Boson. The fermions constitute the three generations of matter and are further divided into the quark and

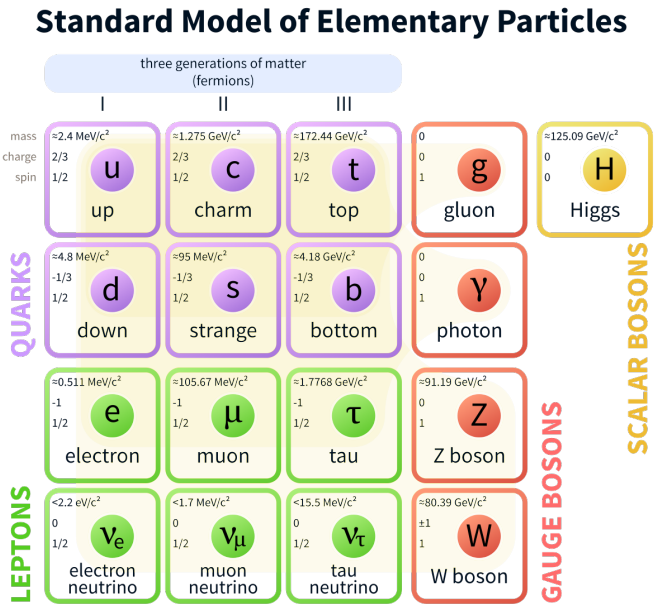

Figure 1.1: A table of the fundamental particles of the Standard Model and some of their properties: mass, charge and spin. The table lists six quarks, six leptons (including the three flavours of neutrinos), four gauge bosons (mediating three of the fundamental forces) and one scalar boson: the Higgs Boson, which provides the mechanism for giving mass to the fundamental particles.

lepton families. Quarks are the building blocks of protons and neutrons and a vast array of particle configurations collectively known as hadrons. Quarks are half-spin particles that exist in three generations of matter (or in six different flavours). The six different types of quarks: up, down, charm, strange, top and bottom are summarized in figure 1.1. In addition to flavour and electrical charge, quarks exhibit a property known as "color" or "color charge" (note that the American spelling is used for "color" as a property of quarks, while the British spelling is used for all other instances of "colour" in the text). Quark color; red, green, blue or their anti equivalents couple them to gluons (which also have color and can self interact) which mediate the strong force. Due to a property known as confinement, color charge cannot be directly observed, all particles observed in a nature must be "white" i.e. all colors balanced. As such quarks are never isolated and exist in quark-antiquark pairs known as mesons (i.e. red and anti-red) and triplets known as baryons (red, green and blue or their equivalent anti-colors). The lowest mass and most stable baryons are protons and neutrons which are made of up and down quarks but a vast menagerie of short-lived baryons exists. More exotic configurations of quarks remain largely hypothetical, although there is some evidence for a pentaquark [2]. Baryon number is a conserved quantity in all known particle interactions, but some Grand Unified Theory extensions to the Standard Model allow for baryon-lepton couplings, which would result in proton-decay over time-scales much longer than the current age of the Universe. Searches for proton-decay placed lower limits on proton half-lives from 10^{31} years to 10^{34} years depending on the decay mechanism [84].

Leptons do not exhibit color charge and hence only interact via their electric charge and flavour. The three generations of leptons include electrons and their heavier cousins: muons and tauons (usually called tau particles). These three particles each have an associated neutrino. In addition these particles have their associated anti particles. In particle interactions, lepton number

is conserved, i.e. in negative β-decay.

$$n \rightarrow p^{+} + e^{-} + \bar{\nu_e} \tag{1.4}$$

All particles in the Standard Model have some fundamental properties including spin (the quantum mechanical equivalent of angular momentum), electrical charge, parity and coupling constants. Fermions, by definition, have half integer spin, a property owing to the Pauli Exclusion principle. All Standard Model fermions, including neutrinos, have a spin of $s = 1/2$ and the gauge bosons have $s = 1$ while the Higgs boson has $s = 0$.

1.3 Neutrino Interactions

In the Standard Model neutrinos interact solely via the weak force (also known as the flavour interaction). The weak interaction exists via the coupling of leptons or quarks to virtual W^{+}, W^{-} and Z^{0} bosons. The two W bosons are electrically charged and are each other's anti-particles while the Z boson acts as its own anti-particle. The W and Z bosons are relatively massive, 80.39 MeV and 91.19 MeV respectively, and due to the Heisenberg uncertainty principle have half lives of around 3×10^{-25} seconds. The short life of W and Z bosons limits the range of the weak force to $\sim 10^{-18}$ metres, 0.1 % of the charge diameter of a proton. The distinction of being *weak* owes to the effective strength of the force per lepton being several orders of magnitude weaker than the strong force and electromagnetism, although it is still vastly stronger than gravity. The weak interaction allows quarks and leptons to exchange flavour. The β-decay of a neutron to a proton can be explained through the transformation of a down-quark in the neutron into an up-quark through the release of flavour and charge via the W^{-} boson. The boson itself decays into an electron and anti-electron-neutrino, with charge and lepton-number conserved as depicted in figure 1.2.

$$q_d \rightarrow q_u + W^{-} \tag{1.5}$$

$$W^{-} \rightarrow e^{-} + \bar{\nu}_e \tag{1.6}$$

Weak interactions mediated by the W bosons are called charged-current (CC) interactions, as they require an exchange of charge as well as flavour, while Z-bosons mediate neutral-current (NC) interactions. An example of CC and NC interaction between an electron and electron-neutrino is shown in figure 1.3. The low range and strength of the weak force of neutrinos to matter means that even dense configurations of matter such as stars and planets are essentially transparent to neutrinos at low energies. The cross-section of neutrinos with leptons and quarks grows with energy according to a power-law ($\log \sigma_\nu \propto \log E_\nu$) [28]. Models of cross section predict the electron-neutrino cross section as 10^{-31} mb for relic neutrinos at 1 K to 10^{-7} mb for astrophysical neutrinos at PeV energies [28]. At high energies the Earth becomes opaque to neutrinos. Observation of atmospheric neutrino attenuation through the Earth by IceCube was used to find the neutrino cross section up to 988 TeV, which was found to be ~ 1.3 times that expected from the Standard Model [11]. However large uncertainties mean this value is still consistent with the Standard Model. A resonant production of W bosons by anti-electron-neutrinos at 6.3 PeV is known as the Glashow resonance [33] but has not yet been observed by IceCube [19].

1.4 Oscillations and Neutrino Mass

Neutrinos are known to exist in different flavour states when observed at different times. Oscillation between flavours implies directly that neutrinos have a non-zero mass, an observation that contradicts the Standard Model which predicts that neutrinos should be massless. Oscillation results from the mixture of mass and flavour eigenstates in a population of neutrinos. As a given

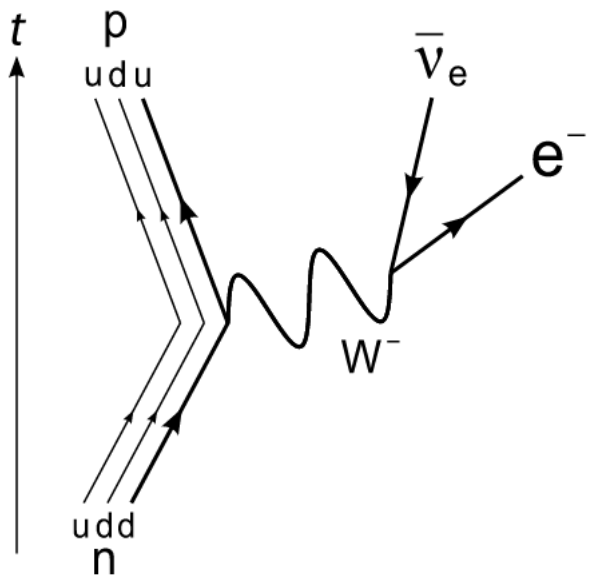

Figure 1.2: A Feynmann diagram depicting β^--decay of a neutron into a proton. A neutron is made of two down-quarks and an up-quark while the proton is made of two up-quarks and one down-quark.

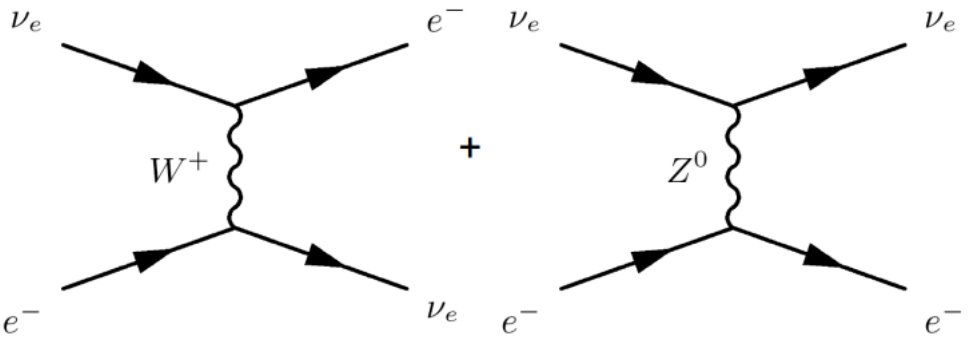

Figure 1.3: A pair of Feynmann diagrams respectively depicting CC and NC scattering between a neutrino and an electron [28].

neutrino propagates through space the phase of the three mass states (simply labelled 1, 2 and 3) change at different rates since the masses are not equal. The changing mixture of mass states results in a change in the flavour mixture.

The rate of change of flavour composition is a function of distance over energy ($R_{\nu_\alpha \to \nu_\beta} \propto D/E$), so that higher energy neutrinos oscillate at a slower rate and over greater distances. In the case of extra-galactic neutrinos, the propagation distance is at least a few orders of magnitude greater than the oscillation distance ($L \sim$ 100kpc for $E =$ 1PeV) allowing the flavour mixture to approach an equilibrium state dependent on the initial mixture [87]. Consequently, careful measurement of the flavour composition by neutrino observatories such as IceCube can help to reveal the production mechanisms of cosmic neutrino sources. A more detailed discussion of experimental constraints on flavour composition is given in chapter 3.

The value of the three neutrino mass states is unknown, indeed the ordering of the three mass states is an unresolved question. From cosmological measurements the sum of the 3 mass states is found to be much smaller than the electron mass such that $\sum_{i=1}^{3} m_{\nu,i} < 10^{-6} m_e$ [63]. There are constraints on the differences of the masses from measurements of solar and atmospheric neutrinos by Super Kamiokande and other experiments [63].

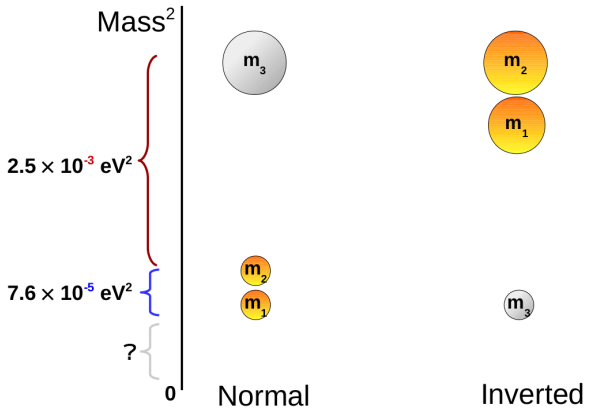

Figure 1.4: Illustration of the normal and inverted mass hierarchy, with the difference in squared masses based on measurements by Super Kamiokande (http://www.hyper-k.org/en/physics). While the squared difference between the mass states is well known, the ordering and absolute masses are not.

1.5 Neutrino Astronomy

In the decades since the Cowan-Reines experiment, neutrinos have been detected from numerous sources, both natural and artificial. In an analogy to the vast electromagnetic spectrum of photons, we can describe the neutrino spectrum across at least 24 orders of magnitude of energy, from the cosmic neutrino background at temperatures on the order of one kelvin to cosmogenic neutrinos at energies comparable to the most energetic known cosmic rays (see figure 1.5).

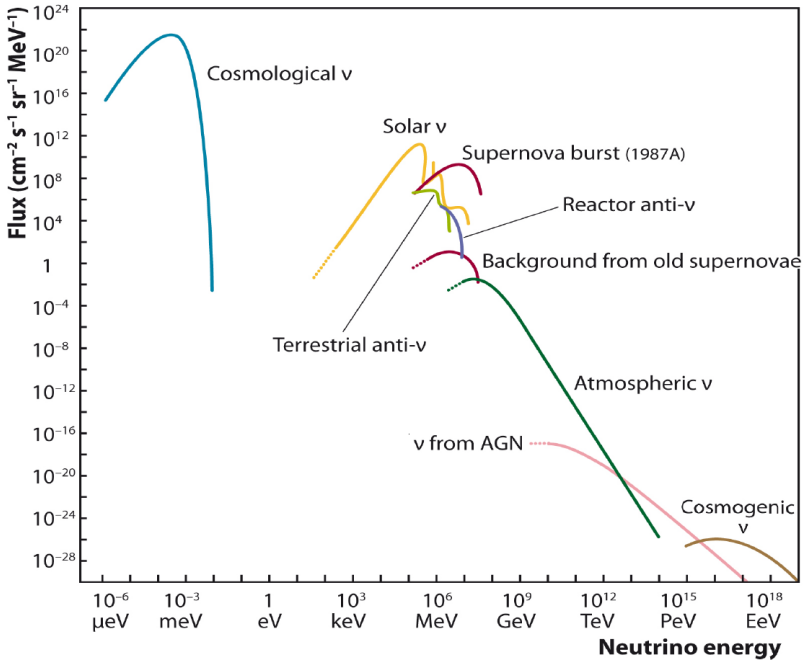

Figure 1.5: The measured and theoretical fluxes of neutrinos from various origin scenarios across 24 decades of energy [49].

1.5.1 Relic Neutrinos $\mu\text{eV} \lesssim E \lesssim \text{meV}$

Relic neutrinos comprise the Cosmic Neutrino Background $C\nu B$, a leftover signature of the Big Bang. Their spectrum is expected to obey a black-body distribution of energy in an analogy to the Cosmic Microwave Background (CMB). In the first second following the Big Bang, the Universe was composed of neutrinos, electrons, positrons and photons in thermal equilibrium with each other. When the temperature dropped to below $10^{10}\,\text{K}$ or 2.5 MeV, neutrinos decoupled from photons as the electroweak symmetry collapsed, but the two species remained in thermal equilibrium as the Universe expanded. However when the temperature dropped to below 0.511 MeV (the mass of the electron), the majority of positrons and electrons annihilated, greatly increasing the energy density of radiation and transferring heat and entropy to the newly created photons, increasing the overall photon temperature [36]. As a result we can estimate the temperature of the $C\nu B$ from the temperature of the CMB ($T_{CMB} = 2.725\text{K}$) by assuming that the entropy of the Universe was conserved during the epoch of annihilation. From the entropy relation $S \propto gT^3$ where S is the entropy, g the degrees of freedom we find:

$$(\frac{g_0}{g_1})^{1/3} = \frac{T_1}{T_0} \tag{1.7}$$

where T_0 and T_1 denote the temperature before and after annihilation respectively. The degrees of freedom are determined by the types of particles: $g_1 = 2$ as the products of annihilation were photons (as they are bosons) while g_1 is found from the sum of fermion degrees of freedom ($2 \times 7/8$ for leptons) and photon degrees of freedom. Hence we find the temperature of the CνB.

$$\frac{T_\nu}{T_\gamma} = \frac{T_{C\nu B}}{T_{CMB}} = (\frac{2}{2 + 2 \times 7/8 + 2 \times 7/8})^{1/3} = (\frac{4}{11})^{1/3} \rightarrow T_{C\nu B} = 1.95\,\text{K} \tag{1.8}$$

Relic neutrinos would have a density 56 ν_e per cm^3 and an average energy of $E \sim 3 \times 10^{-4}$ eV [36]. The extreme low energies of the neutrinos make them extraordinarily difficult to distinguish from other background radiation. However if detected, relic neutrinos would be the most distant

source of radiation measured so far and would be another verification of the Big Bang theory. Detection via induced beta decay of tritium has been proposed using the KATRIN experiment in Karlsruhe, Germany [25] [26] where the following interaction is searched for:

$$\nu_e + {}^3\mathrm{H} \rightarrow {}^3\mathrm{He} + e^- \tag{1.9}$$

Indirect evidence for the $C\nu B$ comes from primordial helium and deuterium abundances and the CMB anisotropy measured by the Planck spacecraft [72].

1.5.2 Solar Neutrinos eV $\lesssim E \lesssim$ MeV

The sun is powered by continous nuclear fusion in the core that transforms hydrogen into helium through a multi-reaction process made possible by the intense temperature of 15 million K in the core. The initial proton-proton reaction is only possible via the weak interaction and is responsible for 86 % of solar neutrinos

$$p + p \rightarrow d + e^+ + \nu_e \tag{1.10}$$

the produced deuterium (d or ${}^2\mathrm{H}$) will fuse with an additional proton producing helium-3 ,

$$p + d \rightarrow {}^3\mathrm{He} + \gamma \tag{1.11}$$

subsequently the helium-3 fuse to produce helium-4,

$${}^3\mathrm{He} + {}^3\mathrm{He} \rightarrow {}^4\mathrm{He} + 2p \tag{1.12}$$

alternatively, the isotopes helium-3 and helium-4 fuse to produce beryllium

$${}^4\mathrm{He} + {}^3\mathrm{He} \rightarrow {}^7\mathrm{Be} + \gamma \tag{1.13}$$

where the berylium isotope contains four protons and seven neutrons. Light elements prefer symmetry between their proton and neutron numbers. ^{7}Be can capture an electron creating ^{7}Li

$${}^7\mathrm{Be} + e^- \rightarrow {}^7\mathrm{Li} + \nu_e \tag{1.14}$$

alternatively the berylium isotope can absorb one of the abundant protons to produce boron,

$${}^7\mathrm{Be} + p \rightarrow {}^8\mathrm{B} + \gamma \tag{1.15}$$

^{7}Li produced thereafter may interact with a proton to produce helium,

$${}^7\mathrm{Li} + p \rightarrow {}^8\mathrm{Be}^* \rightarrow {}^4\mathrm{He} + {}^4\mathrm{He} \tag{1.16}$$

while the boron isotope will remove its excess proton via β^+-decay,

$${}^8\mathrm{B} \rightarrow {}^8\mathrm{Be} + e^+ + \nu_e \tag{1.17}$$

and the resulting beryllium disintegrates into two helium nuclei (as per equation 1.16). Apart from the initial *pp* reaction neutrinos (1.10) another 14 % are produced in the beryllium electron-capture (1.14) while the boron decay contributes only 0.04 (1.17) % [58]. In total the solar neutrino particle intensity at the Earth's surface is $I_{\nu,\mathrm{sol}} \sim 7 \times 10^{10}\mathrm{cm}^{-2}\mathrm{s}^{-1}$. The sun is a pure electron-neutrino source, but the flavour ratio approaches parity due to neutrino oscillations. Consequently measurements of the solar neutrino flux using chlorine neutrino capture ($\nu_e + {}^{37}\mathrm{Cl} \rightarrow {}^{37}\mathrm{Ar} + e^-$) measure only 1/3 of the flux predicted by solar models, the so-called solar neutrino paradox. This paradox was ultimately resolved by introducing neutrino oscillations. At the time of writing the sun is the only identified steady neutrino source beyond the Earth [36].

1.5.3 Supernova Neutrinos $\mathrm{MeV} \lesssim E \lesssim \mathrm{GeV}$

Supernovae are the end stage of the life cycle of massive stars. Over the star's lifetime the initial gravitational collapse of the star is offset by outward radiation pressure from the core powered by nuclear fusion. Massive stars phase through fusion of successively heavier elements, initially converting hydrogen to helium, helium to carbon and oxygen. The cycle continues through oxygen, neon, silicon, sulphur and finally iron, the element with the highest binding energy per nucleon. At this point, fusion of iron cannot generate additional energy and hence provide sufficient radiation pressure to keep the star in equilibrium and the star resumes its initial collapse. The core eventually approaches nuclear densities and temperatures of 10^{11} K (10 MeV) at which point electrons merge with protons to form neutrons. The core is transformed into a neutron star with a radius around $r \sim 10$ km. The de-leptonization initiates a tremendous burst of neutrinos,

$$e^- + p \rightarrow n + \nu_e \tag{1.18}$$

In the high temperatures of the collapse, the thermal photons produce electron-positron pairs which are immediately absorbed by the surrounding matter. Only Z bosons produced in weak interactions,

$$e^+ + e^- \rightarrow Z^0 \rightarrow \nu_\alpha + \bar{\nu}_\alpha \tag{1.19}$$

allow heat to escape from the core in the form of neutrinos [58], produced "democratically" across flavours (1:1:1). In total the neutrino burst produces 10^{58} neutrinos and accounts for 99 % of all energy generated by the supernova ($E_{SN,\nu} \sim 10^{53}$erg). At the Earth, the neutrino emission from a supernova can be observed before the photon emission as the neutrinos escape from the core and travel through the stellar interior whilst it may take hours or days for the shock wave from the core to reach the stellar surface initiating the photon burst. In 1987 neutrinos from a supernova in the Large Magallenic Cloud ($D_{LMC} = 51.4$ kpc) were detected by the Kamiokande and IMB (Irvine-Michigan-Brookhaven) experiments 3 hours before the supernova was seen by conventional telescopes. Today several neutrino telescopes including IceCube, Antares, Super-Kamiokande, Baikal and others form the SuperNova Early Warning System (SNEWS) whose purpose is to broadcast a supernova alert to astronomers if separate neutrino bursts are detected within seconds of each other [79]. Currently IceCube has the sensitivity to detect a supernova within the Milky Way and the Large Magellenic Cloud [52].

1.5.4 Astrophysical and Atmospheric Neutrinos $\mathrm{MeV} \lesssim E \lesssim \mathrm{EeV}$

High energy cosmic rays produce neutrinos via charged pion decay via pp and $p\gamma$ reactions. This may take place in regions of high gas and radiation densities, either at the sources of cosmic ray acceleration or in surrounding environments over the path of the cosmic ray. Indeed assuming that some fraction ($\sim 10\%$) of cosmic ray power is lost at the source to photohadronic and proton-hadronic interactions, one can derive a model-independent upper bound on the possible neutrino flux [89]. Proposed astrophysical neutrino sources include supernova remnants, gamma-ray bursts, active galactic nuclei and star-forming regions. A similar process occurs in the Earth's atmosphere, where cosmic-ray interactions with the air generate pions, kaons and other charmed mesons, producing the atmospheric neutrino spectrum. These processes are discussed in greater detail in chapters 2, 3 and 4.

1.5.5 Cosmogenic Neutrinos $E \gtrsim \mathrm{PeV}$

The cosmic ray energy spectrum extends to $E \sim 10^{20}$ eV based on current measurements [71]. At $E \sim 60$ EeV, CMB photons are blue-shifted to the threshold of pion production in the rest-frame of the proton. Thus the presence of the CMB renders the Universe opaque to the highest energy

protons at cosmological distances, whilst higher mass cosmic rays would suffer similar extinction due to photo-disintegration. The proton decays into a neutron, emitting a charged pion which subsequently decays into μ^+ & ν_μ.

$$p + \gamma_{CMB} \rightarrow n + \pi^+ \rightarrow \nu_\mu + \mu^+ \tag{1.20}$$

The muon and neutrons will subsequently decay:

$$\mu^+ \rightarrow \bar{\mu}_\nu + e^+ + \nu_e \tag{1.21}$$

$$n \rightarrow p^+ + e^- + \bar{\nu}_e \tag{1.22}$$

such that the final flavour ratio is (1:1:0) at the production site. The primary proton loses 20 % of its initial energy per interaction. This is known as the Greisen-Zatsepin-Kuzmin (GZK) effect. The same interaction can also produce high energy photons [55] via neutral pion decay.

$$p + \gamma_{CMB} \rightarrow p + \pi^0 \rightarrow 2\gamma \tag{1.23}$$

The GZK effect gives rise to cosmogenic neutrino and photon flux, neither of which have been detected by observatories such as Pierre Auger and IceCube [1] [54]. The cosmogenic neutrino energy flux has been limited to below $E_\nu^2 \Phi_\nu(E_\nu) < 6.4 \times 10^{-9} \mathrm{GeV cm^{-2} s^{-1} sr^{-1}}$ for an energy range of $10^{17}\,\mathrm{eV} < E_\nu < 10^{19}\,\mathrm{eV}$ assuming an energy spectrum of E^{-2} at 90 % confidence. The upper limit approaches the the upper-limit derived by Waxmann and Bahcall [89].

1.6 Summary

Neutrinos are weakly interacting neutral particles of the Standard Model. They have a small but non-zero mass and therefore oscillate between mass and flavour states. Despite the difficulty of detection, neutrinos have been measured across several orders of magnitude in energy, from GeV energy solar neutrinos up to PeV energy astrophysical neutrinos. The origins of astrophysical neutrinos are still unknown but may be related to the production of cosmic rays in extra-galactic sources. The origins of neutrinos and cosmic rays will be examined in chapter 2.

Chapter 2

High Energy Astrophysics

High energy astrophysics (or particle astrophysics) is the study of the most powerful and violent processes in the Universe. These processes generate high energy electromagnetic radiation, γ-rays with energies in the MeV regime or higher as well as other messenger particles such as cosmic rays and neutrinos. Recently gravitational-wave astronomy has emerged as a probe into objects such as binary neutron stars and black holes, which are also thought to emit high energy particles. In general high energy γ-rays follow an inverse-power law distribution in energy, which differentiates them from thermal radiation at lower energies. The power-law distribution is taken as evidence that high energy γ-rays are generated by cosmic ray collisions which also generate neutrinos. Thus a key goal of particle astrophysics is to find coincident emission between cosmic rays, neutrinos and γ-rays. Unfortunately this task is complicated by the different responses of these particles to magnetic fields, radiation backgrounds and gas clouds that permeate space on galactic and extra-galactic scales. Each "messenger" comes with certain advantages and disadvantages (illustrated in figure 2.1).

1. Cosmic rays have their travel paths bent by magnetic fields as they are electrically charged. Deflection increases with charge and decreases with energy, so for the special case of proton cosmic rays at $E \gtrsim 10^{19}$ eV it may be possible to trace their paths to their origins.

2. γ-rays are electrically neutral, so their paths are unaffected by magnetic fields. However they interact with interstellar gas and radiation, which progressively limits their maximum range with energy.

3. Neutrinos are neutral and weakly-interacting, meaning they suffer no significant deflection and absorption, but these properties make them difficult to detect in sufficient numbers for astronomical observations.

Since particle-media interactions are proportional to the medium's density, it becomes useful to define an "interaction depth" X measured in units of column density [g/cm^2] to use in place of interaction length l, removing density ρ from the discussion. Note that X is defined as the integral of the medium's density over any path traced by a particle in space over distance l.

$$X(l) = \int_0^l \rho(l')dl' \text{ [g/cm}^2\text{]} \tag{2.1}$$

2.1 Cosmic Rays

Cosmic rays are a form of ionizing radiation originating from beyond the solar system (ionizing particles from the Sun are called the solar wind), high energy charged particles that bombard the Earth's atmosphere across twelve orders of magnitude in energy. This radiation may be modified across galactic and extragalactic distances, galactic cosmic rays traverse a depth of 6 g/cm^2 on

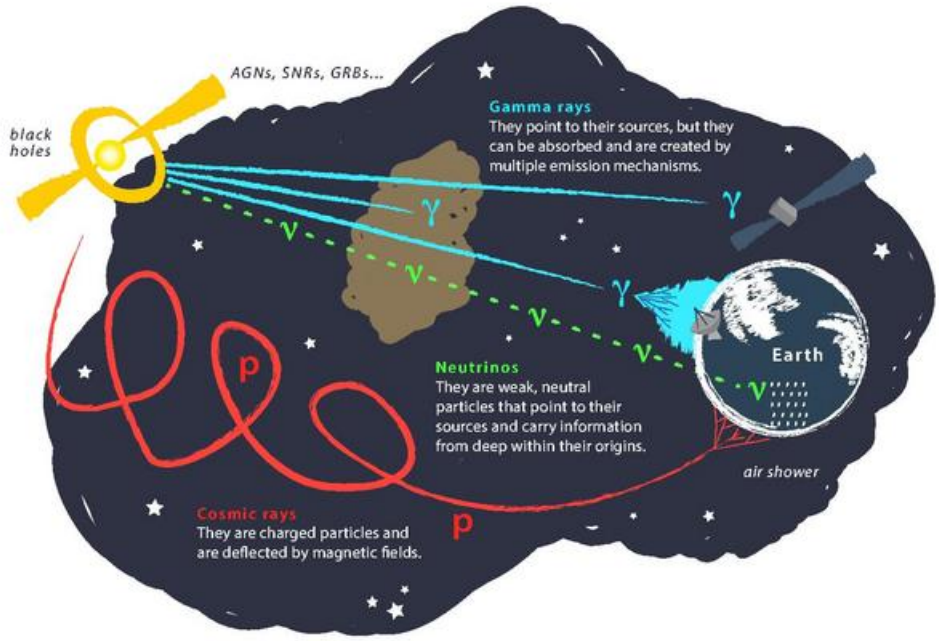

Figure 2.1: A graphical comparison of the properties of cosmic messengers: cosmic rays, gamma-rays and neutrinos (graphic designed by Jamie Yang of the IceCube Collaboration).

average before reaching the "top" of the Earth's atmosphere [58], arbitrarily defined as being at 40 km in elevation [58]. Cosmic rays are generated in the acceleration of charged particles due to Lorentz forces, predominantly protons and electrons. However as the entire periodic table is present in interstellar media, higher mass nuclei up to iron are accelerated giving rise to the mass spectrum of cosmic rays. In the course of interactions in their sources or in the surrounding space (or in the atmosphere) cosmic rays lose energy and generate secondary particles. The unstable mesons (primarily kaons and pions) generated in these collisions subsequently decay into stable particles including photons ($\pi^0 \to 2\gamma$) and neutrinos ($\pi^{\pm} \to \mu + \nu_\mu$). These secondary particles reach Earth carrying information about their sources. When primary cosmic rays arrive at the Earth's atmosphere they interact with the air to eventually produce showers of high energy particles: mesons, muons, neutrinos, electrons and photons which are sometimes also called *secondaries*.

2.1.1 Cosmic Ray Spectrum and Ultra High Energy Cosmic Rays

The cosmic ray spectrum for protons and higher mass ions can be described well across more than ten decades of energy with an inverse power law spectrum with an index of $\Gamma = 2.7$ (figure 2.2). The form of the spectrum indicates a non-thermal origin [30]. Indeed the energy spectrum has been used to draw conclusions on cosmic ray origins in lieu of conventional astronomical observations. The spectrum is described with the differential cosmic ray flux $\frac{d\Phi_{CR}}{dE_{CR}}$:

$$\frac{d\Phi_{CR}}{dE_{CR}} \propto E_{CR}^{-\Gamma} \, [\mathrm{cm}^{-2}\mathrm{s}^{-1}\mathrm{sr}^{-1}\mathrm{eV}^{-1}] \tag{2.2}$$

where E_{CR} is the cosmic ray energy. At higher energies the shape of the spectrum changes, giving rise to three important features of the spectrum: the "knee", the "ankle" and the suppression of the spectrum. The "knee" occurs at $10^{15.5}$ eV where the spectrum softens to $\Gamma = 3.1$. The cause

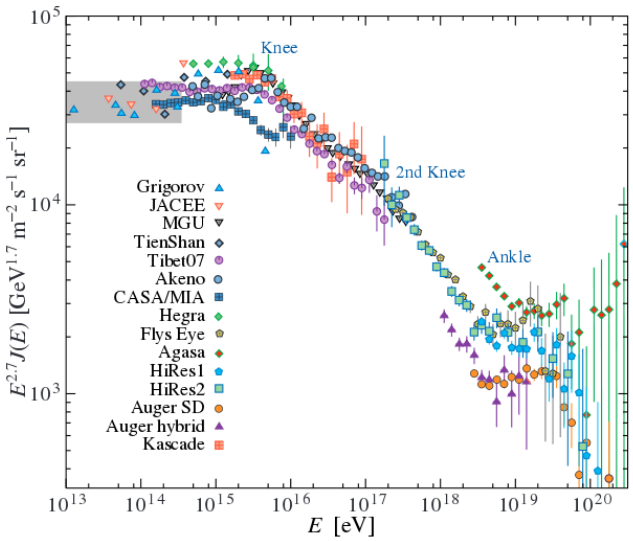

Figure 2.2: The all-mass cosmic ray energy spectrum measured by multiple cosmic ray observatories [15].

of the "knee" is unknown but it possibly marks the maximum acceleration ability of supernova remnants [58]. The spectrum hardens to $\Gamma = 2.7$ at 10^{18} eV, the "ankle". Cosmic rays above the ankle are known as "ultra-high-energy cosmic rays" (UHECRs) and are suspected to be extra-galactic in origin [58]. Recently, cosmic ray observatories including HiRes [40], Pierre Auger [70] and the Telescope Array [81] have observed a suppression of the flux around $E = 10^{19.6}$eV (40 EeV). The abrupt cut-off of the spectrum is thought to be due to attenuation by photons the cosmic microwave background through the Greisen-Zatespin-Kuzmin (GZK) effect with protons or photo-disintegration of nuclei. Both effects become significant at these energies [35] [91].

2.1.2 Mass Composition

The mass or chemical composition of cosmic rays is of great importance in determining their origins. Below 10^{14} eV cosmic rays can be measured directly by particle detectors on satellites and high altitude balloons (some measurements are shown in figure 2.3). Their composition is different from that of the solar system's chemical distribution [58] containing a higher abundance of heavier nuclei. Additionally low energy cosmic rays have an unusually high abundance of rare nuclei such as lithium, beryllium and boron due through collisions with the interstellar medium, a process known as spallation.

At high particle energies $E > 10^{14}$ eV the cosmic ray flux becomes too low for direct detection of the primary, so mass composition must be inferred from air shower features. The usual parameter used in mass reconstruction is depth of the shower maximum X_{max}, the depth at which shower particles fall below the energy threshold for pair production and lose energy to ionization. X_{max} is proportional to the log of the primary's energy before its first interaction E_0, divided by its mass number A:

$$X_{max} \propto \ln(E_0/A) \tag{2.3}$$

The reason for this is that a multi-nucleon cosmic ray will disintegrate into its constituent nucleons upon first interaction, each of which will initiate parallel particle showers which dissipate sooner as each of them has an energy of E_0/A on average. The evolution of X_{max} with energy is called the elongation-rate, which can be used to observe changes in cosmic ray mass composition

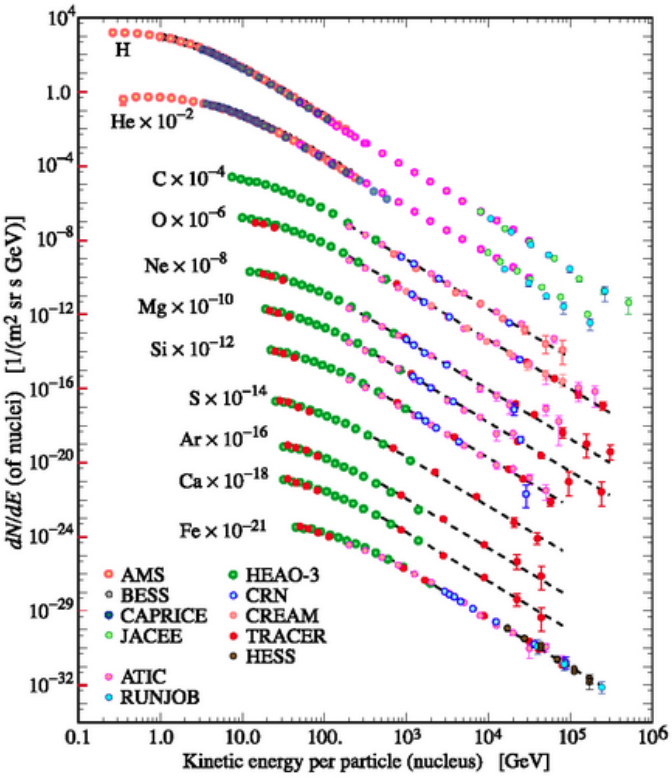

Figure 2.3: Mass composition of low energy ($E < 10^{15}$ eV) cosmic rays from various satellite and balloon detectors, plot created by P. Boyle and D. Muller [16].

with energy. The measured elongation rate by Pierre Auger is consistent with a mixed mass composition with heavier composition at higher energies, in contrast to previous expectations of a pure proton composition [73]. Additionally the number of muons in the shower is dependent of the primary's mass, such that measurements of muon flux at ground level can be used in mass composition analysis.

2.1.3 Production Mechanisms

Any cohesive theory of cosmic ray acceleration must explain the mass composition and spectrum of cosmic rays across different energy regimes. The Fermi mechanism predicts the inverse power-law feature of the cosmic ray energy spectrum from particle acceleration in magnetized clouds. Interstellar space is permeated with turbulent clouds of plasma and their associated magnetic fields. These magnetized clouds have random velocities of $v \sim 15\,\mathrm{ms}^{-1}$ [16] and charged particles interacting with these clouds would be scattered and gain energy on average, since head on collisions are more likely tail-on collisions [30]. The power law spectrum can easily be derived from the Fermi Mechanism: the mean fractional gain $\Delta E = fE_0$ in energy per interaction is proportional to the original energy E_0, so after n collisions we find:

$$E_n = E_0(1+f)^n \tag{2.4}$$

In real world cosmic ray acceleration the Fermi mechanism is usually amplified by additional processes that lead to more efficient particle acceleration. A notable example is shock acceleration from the ejecta of supernovae (see chapter 4) which can account for most cosmic ray acceleration below 10^{15} eV [30]. Other accelerator environments include turbulent interstellar media, pulsar wind nebulae, radio lobes of active galaxies and active galactic nuclei (AGN).

Supernova Remnants are thought to be the source of most galactic cosmic rays as is suggested by observations of TeV γ-rays [86]. Above the ankle, where the extra-galactic flux dominates, the situation is unclear. Studies by the Pierre Auger Collaboration [71] found a correlation of ultra-high energy events with AGN, a result in slight tension with the heavy mass composition indicated by the elongation rate. However subsequent measurements found this result to be less significantas more data was obtained [22].

The accelerating power of cosmic ray accelerators is dependent on their size L and their magnetic field strength B. Pulsars are small sources ($L \sim 10\,\mathrm{km}$) with intense magnetic fields $B \sim 10^{12}\,\mathrm{G}$, whilst the radio lobes of galaxies are very large but have weaker magnetic fields. A source of cosmic rays cannot accelerate a particle with a gyro-radius r_L greater than L. Using the Fermi mechanism the maximum energy E_{max} of cosmic rays generated by a source is given by Hillas relation [39]

$$\frac{E_{max}}{E\mathrm{eV}} = \frac{\beta Z}{2}\frac{B}{\mu G}\frac{L}{\mathrm{kpc}} \tag{2.5}$$

where β is the shock wave velocity in units of the speed of light c and Z is the atomic number of the cosmic ray. Different types of sources can be shown graphically with the Hillas plot (figure 2.4), which displays the size (x-axis) and magnetic field strength (y-axis).

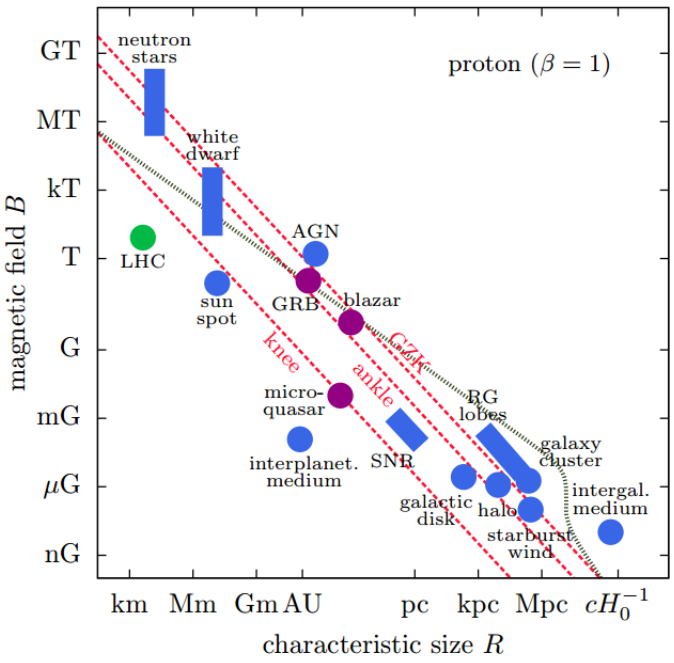

Figure 2.4: In the Hillas plot the range of possible sizes (x-axis) and B field strengths (y-axis) of possible cosmic ray accelerators is shaded with colours [39]. Compact but magnetically intense sources (i.e. neutron stars) are shown in the upper left, while enormous sources with weak fields (galactic halo) are shown in the bottom right.

2.1.4 Propagation

Cosmic rays are subject to electric and magnetic forces as they propagate through space making directional astronomy difficult except perhaps at the higest energies [71]. Galactic and inter-galactic space is permeated with magnetic fields which perturb the trajectories of cosmic rays in an unpredictable manner, destroying origin information. Spallation at low energies suggest that

low energy cosmic rays travel many galactic radii without leaving the galaxy and the arrival directions detected on Earth are largely isotropic. If cosmic rays are indeed originating from point sources, then at high energies it might be possible to measure anisotropy in arrival directions.

A measure of the ability of magnetic fields to change cosmic ray trajectories is the magnetic rigidity (ρ) of cosmic rays [16]

$$\rho = \frac{pc}{Ze}[\mathrm{V}] = Br_{\mathrm{gyro}} \tag{2.6}$$

$$r_{\mathrm{gyro}} = \frac{\rho}{Bc} = \frac{E}{ZeB} \tag{2.7}$$

where B is the magnetic field, p is the cosmic ray momentum, Z is the atomic number and r_{gyro} is the cosmic ray's gyro-radius. In intergalactic space magnetic fields are small ($B \simeq$ nG), so protons at $E = 10^{21}$ eV travel in nearly straight lines across local cosmological distances ($D \leq 100$ Mpc). In addition to experiencing deflection from magnetic fields, the propagation of extra-galactic cosmic rays is limited by attenuation from radiation fields, most importantly by the ubiquitous cosmic microwave background. In the rest frame of an ultra-high-energy proton, the photons of the CMB are blue-shifted to be above the energy threshold for pion production, allowing the following reactions:

$$p + \gamma_{CMB} \rightarrow n + \pi^{+} \tag{2.8}$$

$$p + \gamma_{CMB} \rightarrow p + \pi^{0} \tag{2.9}$$

In the former case the pions generated will decay into neutrinos which should be detectable on Earth with current observatories whilst in the latter, photons are produced which soon cascade to lower energies. On average 20 % of the original proton energy is lost in the interaction [16], leaving the proton more susceptible to magnetic fields. Heavy cosmic rays are photo-disintegrated by the blue-shift CMB, and the energy of ultra high energy cosmic rays dissipates at large distances (~ 100 Mpc).

2.2 Neutrinos

High energy neutrinos are thought to be the by-products of cosmic rays (although alternative models exist), generated in the collisions of cosmic rays with ambient radiation and gas clouds in their production regions or in other environments. These include the Earth's atmosphere where they produce the atmospheric neutrino background observed by IceCube (see chapter 3).

For proton cosmic rays, neutrinos are produced in charged pion decays resulting from p-p and p-γ collisions. In the former, one or more charged pions are emitted which subsequently decay into muons and muon-neutrinos:

$$p + p \rightarrow \pi^{\pm} \rightarrow \mu^{\pm} + \nu_{\mu}(\bar{\nu}_{\mu}) \tag{2.10}$$

The muon then decays into an electron (or positron) and electron-neutrino (or its anti-particle):

$$\mu^{\pm} + \nu_{\mu}(\bar{\nu_{\mu}}) \rightarrow e^{\pm} + \bar{\nu_{\mu}}(\nu_{\mu}) + \nu_{e}(\bar{\nu}_{e}) + \nu_{\mu}(\bar{\nu_{\mu}}) \tag{2.11}$$

which leaves a final flavour ratio of 1:2:0. For p-γ collisions a similar cycle of decay follows:

$$p + \gamma \rightarrow n + \pi^{+} \rightarrow \mu^{+} + \nu_{\mu} \rightarrow e^{+} + \bar{\nu_{\mu}} + \nu_{e} + \nu_{\mu} \tag{2.12}$$

leading to identical flavour ratios. In both cases the produced lepton (muon or electron) will undergo interactions in the environment which may produce electromagnetic radiation (see section 2.3) that can be observed as evidence of cosmic ray acceleration. Note that both interactions

can also produce neutral pions which in turn decay to γ-ray photons (Also discussed in section 2.3).

$$p + p \rightarrow \pi^0 \rightarrow 2\gamma \tag{2.13}$$

$$p + \gamma \rightarrow p + \pi^0 \rightarrow p + 2\gamma \tag{2.14}$$

This simple model of neutrino production holds assuming some level of reactant protons and lack of pion-interactions within the decay time. The latter assumption depends on the interaction environment. The pion-proton cross section is $\sigma_{\pi p} \sim 0.142\,\text{mb}$ (or $1.42 \times 10^{-30}\,\text{m}^{-2}$) and its mean life is $t_{\pi^\pm} = 2.6 \times 10^{-8}$ s. Even in relatively dense environments like the starburst regions of a galaxy (i.e. $\rho_H = 10^6\,\text{m}^{-3}$ in Arp 220 [67]), the interaction length l would be immense i.e. ($l \sim 23\,\text{Mpc}$ in Arp 220) compared to the decay length (6.8×10^{-3}pc at $E_{\pi^\pm} = 10^{21}\,\text{eV}$) for even the highest energy cosmic rays. This means that there is effectively no chance for interactions within the pion life time in even the densest conceivable accelerator environments. However in the Earth's atmosphere, the pion interaction depth is $\lambda \sim 120\text{gcm}^{-2}$ [62] and significant pion interaction occurs within the decay life which effects the energy spectrum of atmospheric neutrinos (discussed further in chapter 3).

2.3 High Energy γ-rays

As mentioned in section 2.2, high energy γ-rays are produced in neutral pion decays resulting from cosmic ray collisions with target gas and photons. These are known as hadronic γ-rays. Additionally γ-rays are also created in leptonic processes; inverse-compton scattering, synchrotron radiation and bremstrahlung scattering. All of these processes can be considered special cases of Compton scattering, as bremstrahlung and synchrotron process can be thought of as the scattering of an electron off of *virtual photons*.

2.3.1 Leptonic Production Mechanisms

Inverse Compton Scattering

Inverse Compton (IC) scattering is the scattering of a high energy electron off a low energy photon. One can think of IC as simply as Lorentz boosted Compton scattering, where in most experimental examples a high energy photon scatters off an electron bound in an orbital. IC is also used to refer to e-γ interactions in environments with high radiation densities and lower matter densities, like interstellar space, as opposed to low radiation densities and high matter densities present under laboratory conditions on Earth. In this case high energy electrons up-scatter ambient photons (such as from the infra-red stellar background) to high energies. The power produced via IC is dependent on the energy density of the target photons U_γ and the lorentz boost γ between the rest frame of the electron and the observer [20]:

$$\dot{E}_{\text{IC}} = -\frac{4}{3}\sigma_T c U_\gamma \beta^2 \gamma^2 \tag{2.15}$$

where σ_T is the Thompson cross section, β is the electron velocity as a fraction of the speed of light c and γ is the lorentz boost factor. This formula is derived by considering the interaction of an electron with a photon field in the rest frame of the electron and lorentz shifting to the observer frame.

Synchrotron Radiation

In presence of a magnetic field an electron will spiral along the lines of the field due to the induced Lorentz force, emitting photons as it decelerates. The emitted radiation is called "cyclotron" radiation. At relativistics energies ($\gamma = E_e/m_e c^2 \gg 1$) the radiation is amplified by relativistic

beaming, and the radiation is described as "synchotron". The process is often in competition with IC to drain the energy of the target photon field, indeed the energy-loss formula are very similar [20]:

$$\dot{E}_{\text{synch}} = -\frac{4}{3}\sigma_T c U_B \beta^2 \gamma^2 \tag{2.16}$$

where U_B is the energy density of the magnetic field. The similarity between formulae 2.15 and 2.16 is no accident. Both describe the acceleration of an electron in the presence of an electric field that it observes in its *rest frame*. Synchrotron radiation is emitted across a broad range of frequencies from Radio to X-ray and γ-ray radiation. Observed synchrotron radiation is indicative of strong magnetic fields, thus associated X-ray or radio emission is taken as evidence of a magnetic field in the presence of a γ-ray source.

Relativistic Bremsstrahlung

The bremsstrahlung ("braking radiation" in German) process involves the deceleration of an electron in the presence of an electric field, in this case the field in the presence of an atomic nucleus. The energy loss rate for electrons in the presence of some atomic/ionic gas of density n_Z [20] is:

$$\dot{E}_{\text{brems}} = -E_e \frac{n_Z Z(Z+1.3)e^6}{8\pi^2 h \epsilon_0^3 c^4 m_e^2} [\ln(\frac{183}{Z^{1/3}}) + \frac{1}{8}] \tag{2.17}$$

It is usually difficult to infer which of these mechanisms, leptonic or hadronic, produces γ-ray emission in a given source and is the subject of much study. For example synchrotron radiation is produced across the electromagnetic spectrum, so coincident X-ray emission in a γ-ray source may be taken as evidence of leptonic emission. Finding the γ-ray production mechanism is crucial in the search for astrophysical neutrinos.

2.4 Detection Methods

The detection methods for high energy cosmic rays, γ-rays and neutrinos share similarities. Most methods involve a massive but transparent target medium, such as the atmosphere, a large body of water or ice. High energy particles react in this medium and emit electromagnetic radiation they can be measured over a larger area. A brief summary of these methods is made in this section.

2.4.1 Extensive Air-Showers

Cosmic rays entering the Earth's atmosphere will interact with nuclei in air molecules producing secondary charged particles which themselves undergo interactions that generate more particles leading to an extensive air shower (EAS). The EAS can be divided into three distinct components: the hadronic core, the muonic shower and the electromagnetic shower. The process of the reaction is similar across the mass range; if the primary has mass number $A > 1$ the first reaction disintegrates the nucleus into its constituent nucleons all of which will undergo interactions similar to a proton primary, just at a smaller interaction depth due to the larger cross-section. For a proton primary the interaction with an air nucleus initiates a hadronic shower as various different mesons are produced.

$$p + N \rightarrow \kappa^{\pm} + \kappa^0 + \pi^{\pm} + \pi^0 \rightarrow ... \tag{2.18}$$

The mesons themselves may interact with the surrounding air before they decay producing more mesons. The charged mesons decay into muons and neutrinos creating the muonic component, whilst neutral mesons decay into photons. A given photon will pair produce a positron and

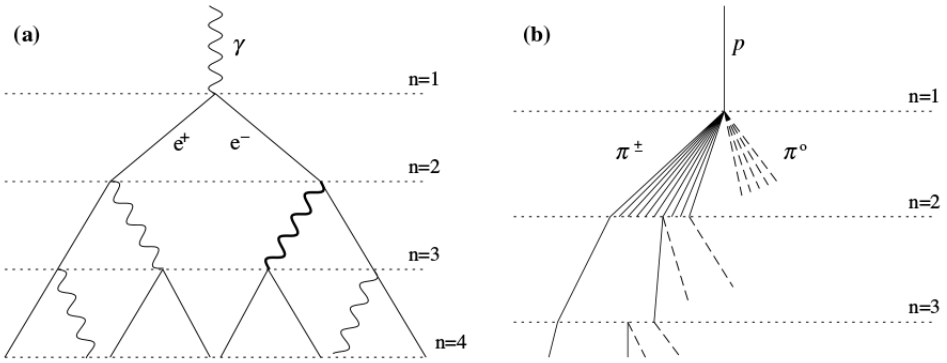

Figure 2.5: A diagram describing the chain of particle production in electromagnetic (a) and hadronic air-showers (b) [62].

electron, each of which produce an additional photon via the bremsstrahlung process (see section 2.3.1), which in turn pair produce and so on.

$$\gamma \rightarrow e^+ + e^- \rightarrow e^+ + e^- + 2\gamma \rightarrow e^+ + e^- + 2 \times (e^+ + e^-) \rightarrow ... \tag{2.19}$$

See figure 2.5 for a graphical description of electromagnetic and hadronic showers in the Heitler model. Each step doubles the numbers of particles per interaction depth λ until the individual particle energy falls below the threshold for losses due to ionization [62] dissipating the electromagnetic shower. Air shower neutrinos are the source of the atmospheric neutrino flux (see chapters 1 and 3) which along with muons are the source of the background measured by neutrino observatories such as IceCube.

At energies greater than 10^{14} eV the cosmic ray flux is too low for primary cosmic rays to be detected directly by satellites or high altitude balloons, instead ground based detectors measure the air shower and reconstruct the cosmic ray properties from features of the air shower. Cosmic ray observatories utilize optical telescopes which measure fluorescent light or surface based particle detectors which measure the secondary particles at a given altitude. A hybrid method combining fluorescence detection and surface detection is employed by the Pierre Auger Observatory in Argentina and the Telescope Array in the United States.

High energy γ-rays entering the Earth's atmosphere will initiate a similar shower of particle through pair-production in proximity of an atmospheric nucleus, with an electromagnetic air shower forming as described by the Heitler model. Air showers initiated by γ-ray photons can be distinguished from cosmic-ray air showers by their lack of a muonic or hadronic component and typically are initiated at lower depths than cosmic rays at the same energy. Secondary particles can be measured at a given elevation to reconstruct the properties: energy and arrival direction of the primary γ-ray. This approach is used by the HAWC observatory in Mexico.

2.4.2 Cherenkov Radiation

The air-showers induced by cosmic rays and γ-rays in the atmosphere produce many trillions of high energy charged particles travelling at speeds very close to the speed of light c in a vacuum. However these particles travel through media: air, water or ice where the effective speed of light is reduced from c by a factor n, the refractive index. The refractive index in air is 1.003, 1.33 for water and 1.309 for ice, meaning that light travels at $0.997c$ in air, $0.75c$ in water and $0.76c$ in ice, values that can easily be exceeded by air shower particles.

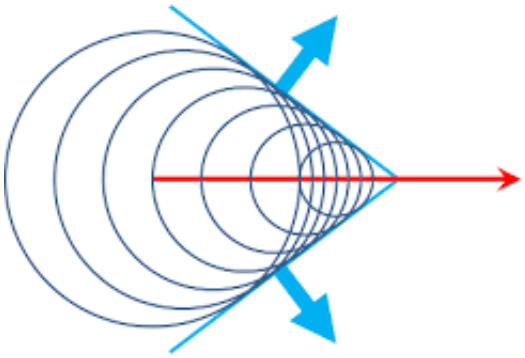

Figure 2.6: The Cherenkov light cone following in the wake of a high speed charged particle.

When a charged particle travels through a dielectric material, the particle's electric field polarizes the molecules in the medium. If the particle is travelling slowly through the medium, the molecules depolarize and the material returns to its equilibrium state. However if the particle is travelling faster than the response speed of the medium given by c/n, there is not enough time for the molecules to depolarize as the particle passes through. This disturbance remains in the the medium, and the material releases the stored energy as a coherent shock wave of light. The shock front of light trails behind the initiating particle as cone described by the critical angle θ_c. This effect can be described as the photonic equivalent of a sonic boom when an object travels faster than the speed of sound. For particles moving very close to c, the critical angle is given by:

$$\cos(\theta_c) = \frac{1}{n} \tag{2.20}$$

For denser media, θ_c is more compact and the cone is more compact and directional. The effect scales up for large numbers of charged particles travelling at $v > c/n$, where their Cherenkov cones combine to form a collective light cone that reaches the surface in a pool of light. High energy γ-ray observatories such as H.E.S.S, MAGIC and VERITAS use Cherenkov emission from electromagnetic air-showers to detect photons at TeV scale energies.

2.4.3 Neutrino Detection

Neutrino interactions with matter are far rarer than for cosmic rays or γ-rays. To detect neutrinos, the detector volume must be sufficiently large that a sufficient number of neutrinos interact within. Neutrino detectors are typically built in water or in ice, materials which are both dense and transparent to light and have refractive indices that allow for the detection of Cherenkov emission.

Neutrinos interact with an atomic nucleus in the water molecules through a charged-current interaction, where it produces its corresponding charged partner (e, μ or τ) which will initiate an electromagnetic shower and produce a cone of Cherenkov light. The propagation of the Cherenkov light differs between liquid water and ice. Liquid water has a higher absorption coefficient than ice, so the light propagates over a shorter distance. Cherenkov photons travelling through ice are subject to Mie scattering, so coherent light from a Cherenkov cone is scattered and diffuses through ice at a slower rate, travelling a greater distance compared to liquid water. The pattern of the Cherenkov emission measured in a detector can be used to reconstruct the energy and direction of the lepton. Since these interactions necessarily occur at high energies, there will be very little change between the trajectory of the neutrino and its successor lepton due to Lorentz boosting. Thus reconstructing the lepton properties goes a long way towards

inferring the properties of the neutrino. This issue is illuminated in the following chapter when discussing neutrino reconstruction methods employed by the IceCube Neutrino Observatory.

2.5 Summary

High energy astrophysics allows us to explore some of the most energetic and violent processes in the Universe. However each of the messenger particles considered; cosmic rays, γ-rays and neutrinos come with their own advantages and problems from this perspective. Cosmic rays are subjected to Lorentz forces from magnetic fields along their travel paths, so cosmic rays measured at Earth will not point back to their sources except for the special case of protons at energies above that expected for the GZK limit. High energy γ-rays travel in straight lines but may be absorbed by interstellar gas and radiation fields. These effects are proportional to energy, so the effective horizon for γ-rays decreases with energy. Additionally the abundance of hadronic and leptonic mechanisms for γ-ray production makes it difficult to infer cosmic ray acceleration at a γ-ray source.

Neutrinos are neutral and weakly interacting, so experience neither deflection nor absorption, but the latter property makes them difficult to detect in useful numbers for astronomy. Consequently neutrino detectors must have very large ficudial volumes to detect large numbers of neutrinos. An observation of significant coincident γ-ray and neutrino emission from the same location in space would be very strong evidence for the presence of cosmic ray acceleration, but to date, none have been observed.

Chapter 3

IceCube Neutrino Observatory

3.1 Overview

The IceCube Neutrino Observatory is a gigaton scale neutrino detector located at the geographic South Pole in Antarctica adjacent to the Amundsen-Scott South Pole Station. The primary goal of the experiment is to identify high energy astrophysical neutrinos and investigate their origins. However the detector is also at the forefront in the study of neutrino oscillations, the mass hierarchy problem, searches for extra-Standard Model particles including Dark Matter and Sterile Neutrinos and mapping of the Earth's density profile. This chapter looks at the design and operation of the detector as well as efforts to identify astrophysical neutrinos and trace their origins to point sources.

3.2 Design

The detector utilises a cubic kilometre of glacial ice as an enormous target volume for neutrinos and the optical properties of the ice are ideal for detection of the induced Cherenkov light. The detector is an array of 5600 digital optical modules (DOMs) deployed along 86 strings over a depth of 1.5 km to 2.5 km below the surface of the ice shelf [7]. The ice at this depth is some of the purest in the world and highly transparent to Cherenkov photons (absorption length $D_{\text{abs}} \sim 200\text{m}$). The depth of the detector serves to reduce the background muon rate from cosmic ray air-showers. Along each string the DOMs are separated by 17 metres and neighbouring strings are separated by 125 metres. The DOMs absorb incoming Cherenkov photons, converting the energy into an electric current. The signals are transmitted via the strings to be processed and stored as data at the IceCube Laboratory (ICL) at the surface. IceCube was built around its predecessor the Antarctic Muon and Neutrino Detection Array (AMANDA) which operated during the late 1990s and early 2000s. Construction on IceCube began in January 2005 with the deployment of the first string and was completed in December of 2010. AMANDA was enveloped within the corner of IceCube and was switched off in 2009. The role of AMANDA was superseded by the in-fill DeepCore array which has a DOM to DOM spacing of 10 metres, allowing it to be sensitive to lower energy neutrinos $E \sim 10\,\text{GeV}$ [12]. There are no DeepCore DOMs between 1850 and 2107 metres of depth, due to the presence of a dust layer which scatters Cherenkov light. See figure 3.1 for a schematic diagram of the IceCube observatory.

IceTop is a complementary detector on the surface of the ice sheet directly above the IceCube array. IceTop is made of 162 frozen water tanks [44], each containing two DOMs which measure Cherenkov light in the same way as the rest of the detector. IceTop can measure cosmic ray air-showers in a similar fashion to the surface detector of the Pierre Auger Observatory.

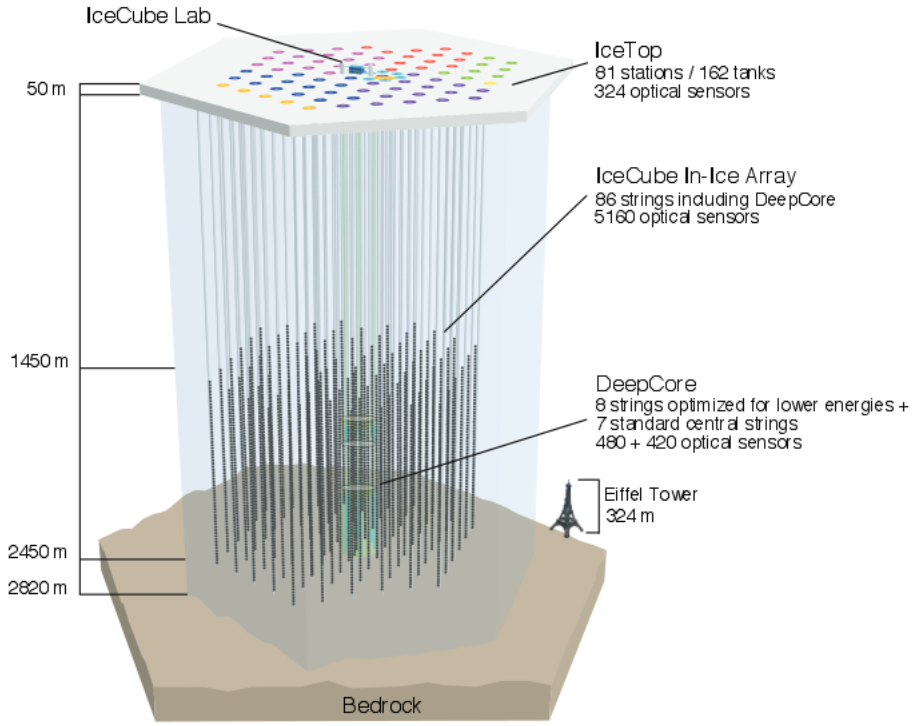

Figure 3.1: A schematic diagram of the IceCube Neutrino Observatory, with the in-ice IceCube array, IceTop and DeepCore displayed [7]. The Eiffel Tower is shown for scale.

IceTop provides a useful cross-check on the origins of events measured in the array. If a muon enters the array from outside and at the same time IceTop measures an air-shower one can assume the muon is formed from the air-shower and not from an astrophysical neutrino. On the other hand if the muon begins inside the in-ice array, one can be confident that it was produced by an interacting neutrino.

3.2.1 Digital Optical Modules (DOMs)

Each of the 5600 in-ice DOMs contain a large photo-multiplier tube (PMT) in the lower hemisphere connected to a printer circuit board potted in a clear glass sphere 330 millimetres in diameter, insulated with a transparent silicon gel [66] (see figure 3.2). A cable running from the upper hemisphere connects the device to the power source and electronic controls in the ICL.

The PMTs contain a negatively charged photo-cathode, a series of 10 dynodes of progressively higher potential and a positively charged anode. When the photo-cathode is struck by a Cherenkov photon the energy releases an electron from the cathode material. This photo-electron (PE) is accelerated by the electric field towards the first dynode. When the electron strikes the dynode, the energy it has gained causes multiple electrons to be ejected from the first dynode towards the second. These secondary electrons gain more energy as they accelerated towards the second dynode at higher potential, releasing more electrons upon collisions. The process repeats until a very large number of electrons arrives at the anode. The number of generated electrons depends on the potential difference between the cathode and anode. For an IceCube PMT the potential difference is $V \sim 1300$ V, resulting in a gain of 10^7. In other words the initial photo-electron eventually produces around 10^7 electrons at the anode, resulting in a powerful signal.

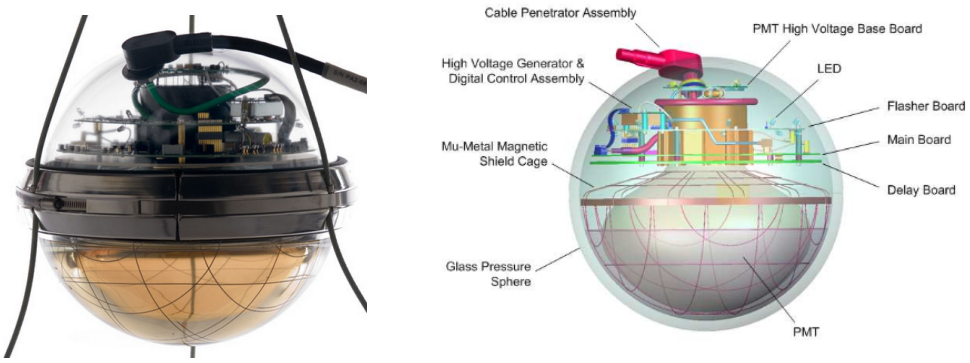

(a) (b)

Figure 3.2: (3.2(a)) A photograph of a DOM from the University of Wisconsin-Madison Physical Sciences Lab [66]. 3.2(b)A schematic diagram of an IceCube DOM [45].

The arriving electrons at the anode are measured as a current proportional to the intensity of the Cherenkov light. The distribution of the current over time is described by the DOM's waveform. By combining the waveforms from multiple DOMs for a single neutrino event, the direction, energy and flavour of the primary neutrino (or muon) can be reconstructed. This is achieved through numerical methods, whereby the waveforms across DOMs are predicted beforehand for a given set of particle parameters through simulations accounting for ice properties and other factors. A likelihood function is maximized until the input parameters of the simulation match with the observed DOM waveforms, a process known as event reconstruction.

Data Acquisition (DAQ)

Before the DOM's signal can be used for event reconstruction it must be determined what proportion of it is genuine signal and how much is simply background noise. Since current can also be present in the PMT without any input photons, the waveform must be calibrated to remove as much background noise as possible. When current is generated, the increase in voltage is registered as a digital signal. The digital signal is sampled via four channels on the PMT circuit board: three for the Analogue Transient Waveform Digitizer (ATWD) and one for the flash Analogue to Digital Converter (fADC or ADC). The ATWD had a sample rate of 300 MHz, or a sample interval of 3.3 ns. Each ATWD has ten-bit resolution, meaning each will record a digital voltage as an integer between 0 and 1024 (2^{10}). The ATWD conducts 128 measurements over a total sample time of 422 ns. Faint signals will only activate one or two channels. If either channel exceeds the digitized value of 768, the third channel is activated.

The ATWD typically measures the first arriving Cherenkov light, triggered when the incoming charge exceeds 0.3 PE at the cathode. The light could be direct from a nearby muon, or it could have been produced earlier in the track and was scattered. The signal from late arriving photons is measured using the fADC with a slower sampling rate of 40 MHz, or a sampling interval of 25 ns. This digitizer makes 256 measurements, resulting in a longer measuring time of 6.4 μs, allowing it to record broader waveforms [37]. The signal from the four channels is called the raw data. The raw data is fed into a wave calibrator where the count integers are converted into a signal measured in mV (see figure 3.3 for illustrated waveform in both digitizers). Each channel has a non-zero baseline voltage which is subtracted by the wave calibrator. Each count in the fADC corresponds to a known voltage gain. The baseline subtracted counts are multiplied

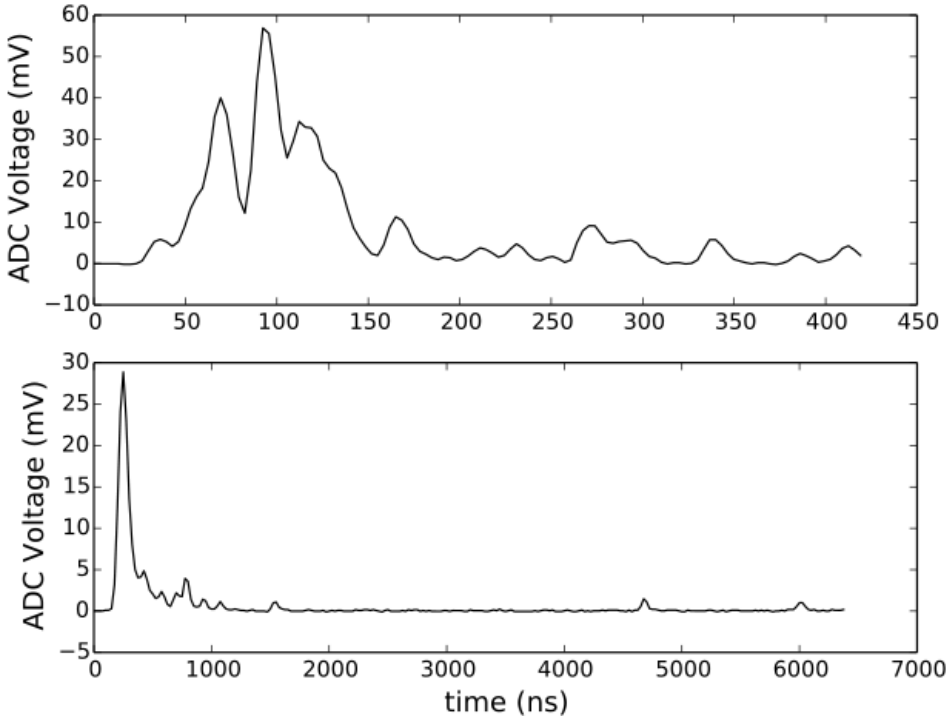

Figure 3.3: An example signal measured by ATWD (top) measured over 427 ns and fADC (bottom) over 6.4 μs. Events are reconstructed from the distribution of charge over time (waveform). [7]

by the gain to produce the corresponding voltage.

The timing of the new waveform must be corrected to allow for the delay from the time taken for the signal to propagate through the PMT. The waveforms are then corrected for the "droop" in the DOM's transformer. The transformer acts as a high pass filter which attenuates the waveform following the first peak, lowering the peak from its true value. This is compensated for by adding voltage at each point of the waveform. Finally the three ATWD waveforms are averaged into the overall ATWD waveform for the DOM.

After calibration, the waveform is analysed by a feature extractor which searches for strong peaks (pulses) above the noise. The feature extractor searches for a local maximum at each time along the waveform. The slope leading up to the maximum is used to extrapolate a line down to the baseline noise. The point at which this line intersects the baseline is taken as the starting time of the pulse. The voltage per bin is summed up from the start time until the voltage falls below the baseline or until it starts to rise again signalling the beginning of another pulse. The sum determines the number of photoelectrons present in the pulse which defines the pulse's charge. The pulse width is simply defined by the time difference between the start and the end of the pulse. The pulse series across multiple DOMs is then used to reconstruct the particle parameters.

3.2.2 IceCube-Gen2 and PINGU

IceCube-Gen2 is a next generation neutrino detector proposed as an extension to the existing IceCube observatory. It would extend the instrumented volume to $\sim 10\,\mathrm{km}^3$ (see figure 3.4), with a string to string distance of 240 metres, although 300 metres has also been proposed [46], and next generation DOMs with higher quantum efficiencies. IceTop would also be complemented

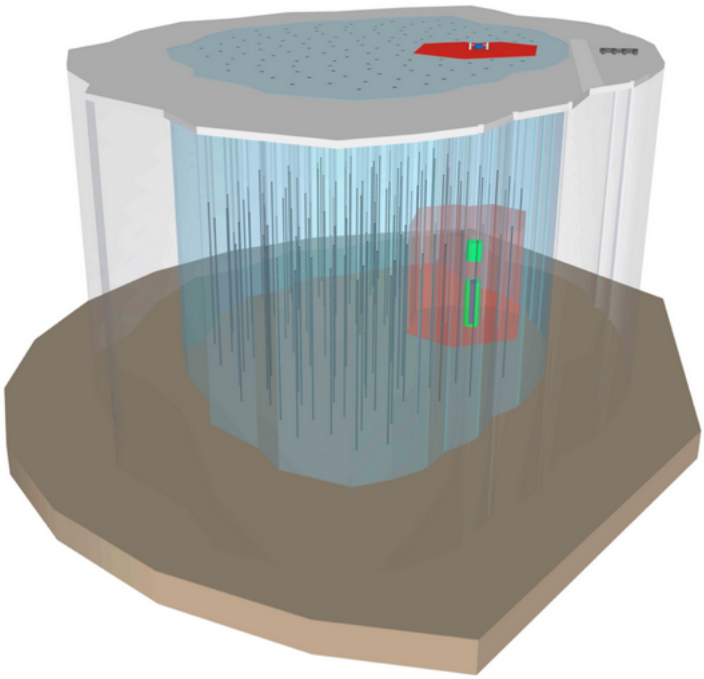

Figure 3.4: The proposed layout of IceCube-Gen2, existing detector volume highlighted in red with DeepCore in-fill in green and the extension in blue.

by an extended array of 6.7 km in radius, increasing air-shower detection and veto ability [83]. The increased measuring volume would increase overall event statistics and increase the detector's sensitivity to the diffuse flux and point sources as well as extend the maximum energy of measured events.

Additionally, an additional string containing 60 DOMs spaced apart by 5 metres would be embedded within DeepCore to increase the detector's sensitivity to lower energy events. This proposed experiment: the Precision IceCube Next Generation Upgrade (PINGU) would provide the largest effective area for detection of GeV energy neutrinos and would be used to constrain neutrino mixing parameters.

3.3 Detection

IceCube measures Cherenkov light induced by charged decay products of neutrinos and cosmic ray muons. Passing neutrinos undergo deep-inelastic scattering with atomic nuclei in the ice or rock in the detector vicinity. The signature of the events is defined by the Cherenkov emission morphology; the main two event types are "cascades" and "tracks". Cascades are caused by CC scattering by ν_e and ν_τ and NC interactions of all flavours. Tracks are caused by ν_μ CC-scattering, in which the primary decays into a muon which may propagate for several kilometres, emitting a cone of Cherenkov light along the way.

A third of interactions are NC-scattering in which a third of the neutrino kinetic energy in transferred to a quark in the nucleus, triggering a hadronic particle shower propagating over 5 m. If the vertex is contained within the detector the DOMs can measure the Cherenkov light. The remaining two thirds of the interactions are CC, in which the neutrino is converted to lepton of the same flavour while still losing energy to the nucleus.

The ability to reconstruct the vertex position, energy and direction relies crucially on the flavour.

An electron will induce a short range EM shower, whose energy can typically be reconstructed to $\frac{\Delta E}{E} \sim 0.1$ at $E > 10\,\text{TeV}$. Reconstructing the direction comes with fitting the spatial and temporal profile of the photons to a template of the angular emission profile. The scattering length of Cherenkov-photons in the ice limits angular resolution to $\sigma \sim 10^{\circ}$.

Muons have a rest mass 200 larger than electrons and thus do not experience as much Coulombic scattering and are able to traverse many kilometres of ice. The Cherenkov emission is not usually contained within the detector, which complicates energy reconstruction. The muon follows the trajectory of the original neutrino and as such it is relatively easy to find the vertex of the the muon's travel path. Thus track events have relatively good angular resolution with an average value $\sigma \sim 0.7^0$. Tau-neutrinos decay into tau particles (or tauons) initiating a cascade shower in the process. The tau particle is short-lived with a decay time of $t_{\text{decay}} = 2.9 \times 10^{-13}$ seconds in the particle rest frame and thus will decay after travelling a relatively short distance, producing a secondary cascade of particles and flash of Cherenkov light. This is known as a "double bang" event. A tau particle requires 20 TeV of energy for every metre travelled and since DOMs are at least 17 metres apart, "double bang" events are only distinguishable from ν_e-cascades at PeV scale energies. At the time of writing none have been identified.

3.4 Results

3.4.1 Diffuse Astrophysical Flux

Observations of neutrinos by IceCube began in 2008 while the detector was still under construction. Weak indications of an astrophysical flux of muon neutrinos exceeding the Waxman-Bahcall upper bound was found in the 59-string configuration [82]. By 2012 two PeV energy events had been measured in addition to twenty-six events that started in the detector with energies in excess of 30 TeV. This was in excess of the predictions of the atmospheric background at a 4σ confidence level, marking the discovery of astrophysical neutrinos [41]. After an additional year of observations, the astrophysical flux was fitted to $E^2\Phi_\nu(E) = 10^{-8}\text{GeVcm}^{-2}\text{s}^{-1}\text{sr}^{-1}$ per flavour at energies between 100 TeV to 100 PeV [8], ruling out an atmospheric-only hypothesis at 5.7σ confidence (see figure 3.5). The latter two discoveries were made by selecting for high energy "starting events": events where the neutrino interaction took place within the detector leading to a particle cascade and Cherenkov flash that started inside the detector. Starting events are distinguished using the boundary of the detector as a veto against events initiated outside the detector.

High Energy Starting Events (HESE)

In order to isolate in-detector starting events we use a volume veto. Starting events can be distinguished from incoming muons via the veto where we exclude photons coming before the event vertex . The event is rejected if photons arrive before the vertex time on the outermost layer of the detector. This reduces the number of air-shower muons in the sample to a level far below that of atmospheric neutrinos before additional cuts are placed on the latter. Atmospheric neutrinos can be removed from the sample using an energy cut (around 50 TeV). For very bright events with thousands of photons, the outer layer veto is sufficient to reduce the muon background. But at lower energies the muon rate increases rapidly making the outer layer veto method an untenable filter.

Medium Energy Starting Events (MESE)

To lower the energy thresholds the first modification is to remove the requirement that the veto photons are detected on the outermost layer of DOMs and in local coincidence (two photons detected at once). The second modification is that the photons are used as a veto if they

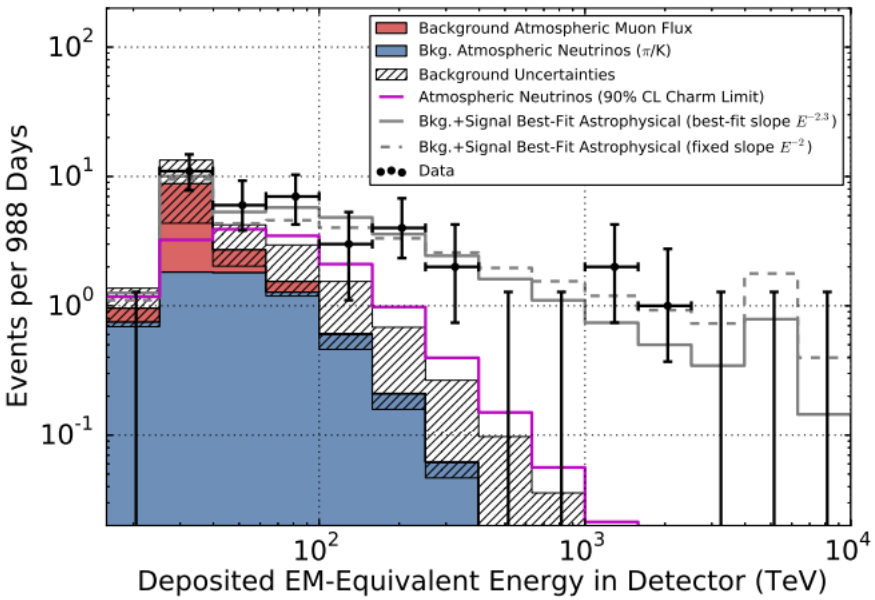

Figure 3.5: The distribution of deposited energy from atmospheric muons and neutrinos and the best fit of the signal component for $\Gamma = 2$ and $\Gamma = 2.3$ (the best fit spectral index to the data)[8]. The distributions account for the HESE veto. The data shows a clear excess above what is expected from atmospheric neutrinos and muons at $E \gtrsim 100$ TeV.

are associated with part of an incoming track not containing the vertex. Some proportion of the volume is used as a veto volume to reconstruct the potential incoming tracks and the remainder for reconstruction of starting events. As the ratio of veto volume to detector volume increases the minimum threshold energy is reduced as the correspondingly higher flux of muons can be more efficiently excluded. The detector volume reduces from everything inside the HESE veto layer progressively down in steps until containing the in-fill DeepCore, with the remainder of the detector used for vetoes (see figure 3.6). This method allows the threshold energy to reduce to 1 TeV for astrophysical neutrino searches [10]. Using MESE the flux was constrained to $\Phi_\nu(E) = 2.06^{+0.4}_{-0.3} \times 10^{-18}(E/10^5\text{GeV})^{-2.46\pm0.12})\,\text{GeV}^{-1}\text{cm}^{-2}\text{s}^{-1}\text{sr}^{-1}$ for an energy range of $25\,\text{TeV} < E < 1.4\,\text{PeV}$. Prompt emission was limited to 1.52 times the level predicted by theory [43].

Up-going diffuse sample

An alternative method of removing atmospheric muons is to restrict the event sample to events arriving below the horizon ($\delta > -5^0$) using the Earth to remove atmospheric muons through absorption. An analysis looked for evidence for an astrophysical flux in track events from the northern sky from the first 659.5 days of data [6] with $\sim$ 300,000 events present. The majority of the muons in this sample ($\sim$ 99.9%) were generated by atmospheric muon-neutrinos but an exclusive terrestrial origin from air-showers was rejected at 3.7σ confidence (see figure 3.7). The astrophysical component to the flux was fitted to $\Phi_{\nu_\mu}(E) = 9.9^{+3.4}_{-3.2} \times 10^{-19}(E/10^5\,\text{GeV})^{-2}\text{GeV}^{-1}\text{cm}^{-2}\text{s}^{-1}\text{sr}^{-1}$ [6]. This corresponds to $\sim$ 318 tracks of extra-terrestrial origin in the sample. The majority of these tracks were from CC-interactions of astrophysical muon-neutrinos but a minority may originate from tau-neutrinos producing taus which subsequently decay into muons.

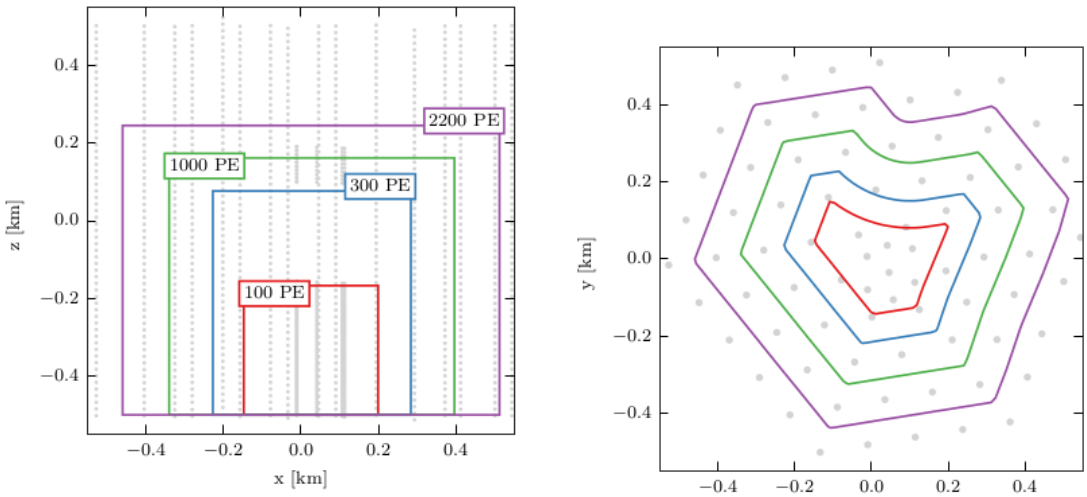

(a) (b)

Figure 3.6: Progressive volume cuts [10] used to obtain the MESE sample. The coloured lines enclose the event reconstruction volume, with the ficudial volume used to veto atmospheric muons. The reconstruction volume shrinks as the photo-electron threshold is reduced. Figure 3.6(a) displays volume cuts side-on, while figure 3.6(b) shows them from the surface down.

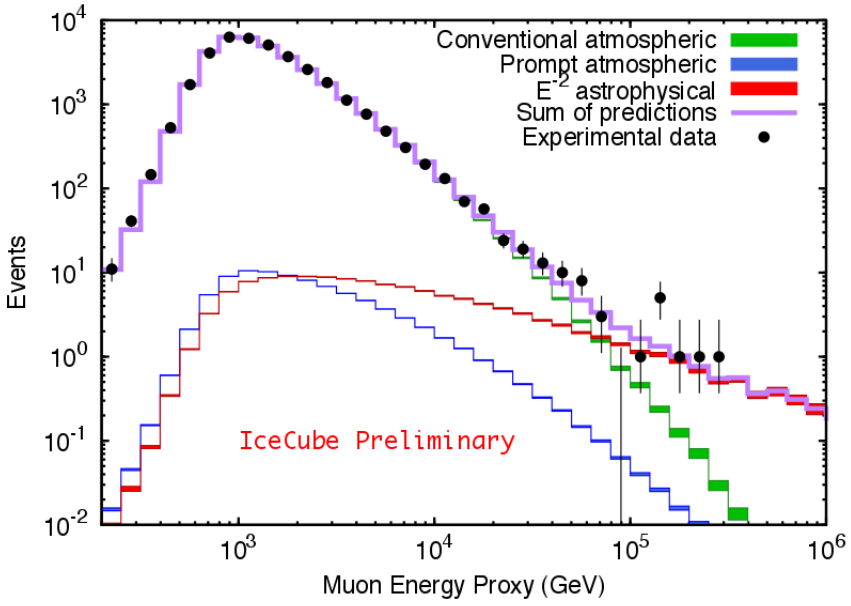

Figure 3.7: The energy spectrum of secondary muons generated by muon-neutrinos from conventional and prompt atmospheric generation and an E^{-2} astrophysical flux. The data displayed shows an excess from atmospheric-only hypothesis [46] [6].

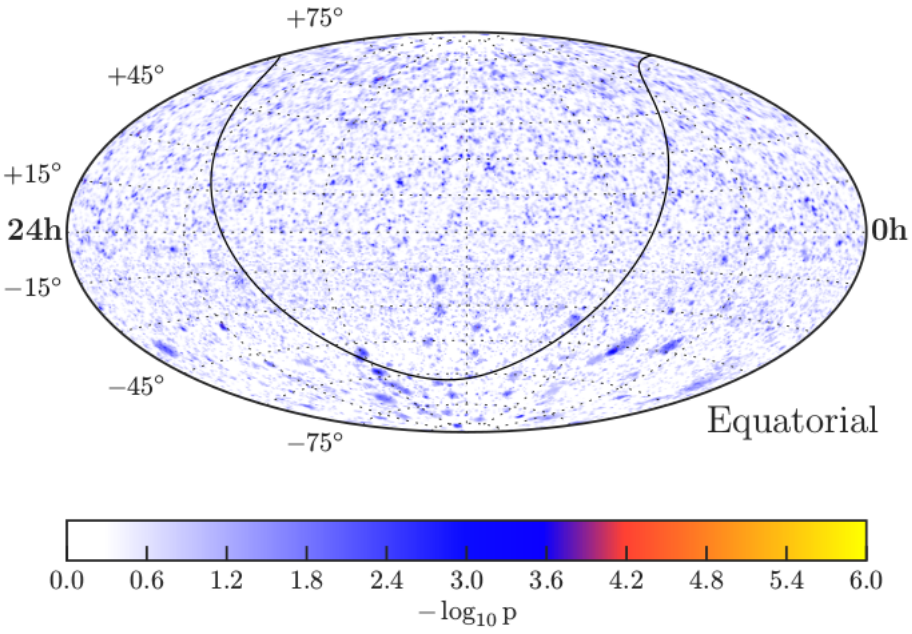

Figure 3.8: A likelihood map showing the likelihood that an excess of events at a particular location in the sky corresponds to a fluctuation from the diffuse background [43] [3]. No significant excess is observed in any direction.

3.4.2 Point Source Searches

Since the discovery of extra-terrestrial neutrinos, efforts have been under way to determine their origins by attempting to trace their arrival directions to distant point sources and checking for cross-correlations with the locations of likely electromagnetic counterparts. The initial discovery was made using a sample dominated by cascades, whose relatively poor angular resolution made point source analyses difficult.

The most conventional point source analysis involves searching for an excess of events at a given location x above that expected for a diffuse background. The most significant excess is considered the most likely location of a single point source that produces a certain number of events, or a certain fraction of the overall neutrino flux. This is achieved by finding the maximum value of a likelihood function $\mathcal{L}(\vec{x}, \theta)$ of the set of event positions $\vec{x}$ over a parameter (θ) space of possible positions of the point source x_{src} and signal strengths (measured with the number of signal events n_s):

$$\mathcal{L}(\vec{x}, \theta) = \mathcal{L}(\vec{x}, x_{src}, n_s) = \prod_{i=1}^{N} [\frac{n_s}{N} S(x_{src} - x_i) + 1 - \frac{n_s}{N} B(x_i)] \tag{3.1}$$

n_s is the number of events originating from the point source, N is the total number of events in the analysed sample, $S(x)$ is the signal probability density (PDF) as a function of the event coordinates x and $B(x)$ is the background probability density function. The form of the signal PDF depends on the form of the analysis, but is usually described by a two-dimensional Gaussian peaking at x_{src} (for the case of a single point source). The background PDF can be estimated from simulations of the diffuse component of the flux, or simply by scrambling the azimuthal coordinates of the real data. In the case of a flat background across the sky we simply set the background to $B = 1/4\pi$. The narrow angular resolution of tracks means that clustering of tracks is considered far more significant than for cascades and more evident of a point source. Neutrino energy is often used as a parameter in these searches, since astrophysical events have

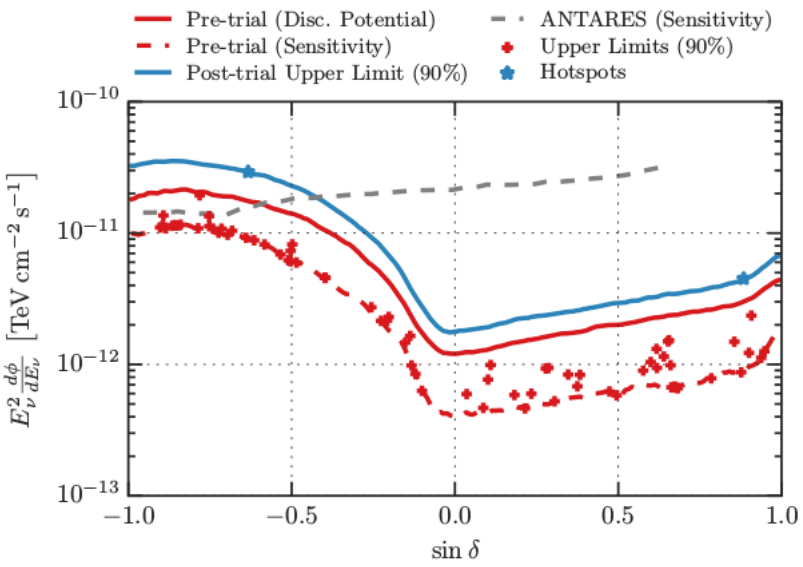

Figure 3.9: The flux upper limits for various point source scenarios shown as a function of declination across the sky. [43][3]. See chapter 9 for the definitions of sensitivity and discovery potential

a different energy distribution to atmospheric events. Thus the up-going diffuse sample is the most useful from the point of view of point sources, and thus a higher sensitivity to point sources exists for events from the northern hemisphere.

An alternative method involves searching for a correlation between neutrino arrival directions and the positions of objects likely to produce neutrinos under some astrophysical model. Instead of scanning for the most likely position based on the neutrino data, source positions are fixed and the overall signal PDF is the combination of point spread functions (PSFs) defined by the position of the sources. This is known as a stacked point source analysis. For a summary of point source methods and a derivation of the point source likelihood function see chapter 7.

As of the time of writing no significant hotspots suggestive of a source have been observed in any of the neutrino samples despite extensive analyses (see figure 3.8). Instead upper-limits have been placed on the point source fluxes (see figure 3.9) across the sky, from $E^2 d\Phi_\nu(E)/dE \sim 3 \times 10^{-11}\,\mathrm{TeVcm^{-2}s^{-1}}$ near the south celestial pole to $E^2 d\Phi_\nu(E)/dE \sim 2 \times 10^{-12}\,\mathrm{TeVcm^{-2}s^{-1}}$ near the equator [3]. The most extensive stacked analysis, looking at blazars, have limited their contribution to the neutrino flux to less than 27 % [5]. The lack of an observed point source has been used to limit the the strengths and densities of different classes of possible sources [64], with some types of radio galaxies, Seyfert galaxies and star-forming galaxies compatible for point source limits and the observed diffuse flux. See Section 4.2 for a more detailed discussion.

3.4.3 Flavour Spectrum

The flavour composition of astrophysical neutrinos contains information about their production mechanism at their sources. Different production scenarios lead to different original flavour ratios which will lead to a specific flavour ratio at Earth due to neutrino oscillations. In particular charged pion decay from cosmic ray interactions leads to a $(\nu_e{:}\nu_\mu{,}\nu_\tau) = (1{:}2{:}0)$ ratio at the source, which evolves into an even ratio (1:1:1) over the great distances traversed towards the Earth [87]. Because analyses can only distinguish between two event morphologies; cascade and track, the flavour composition cannot be measured directly and there is a strong degeneracy in the inference

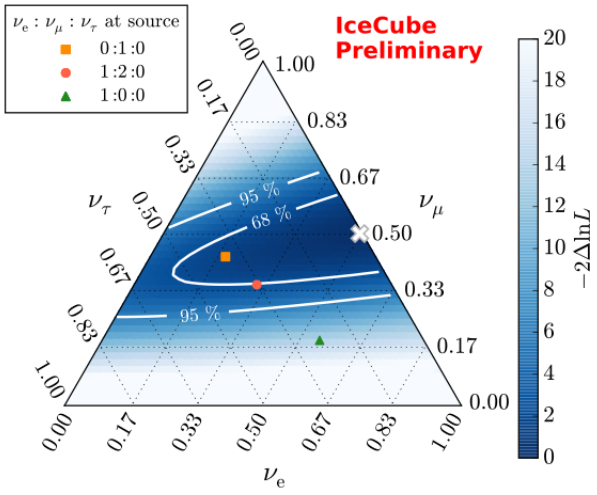

Figure 3.10: The best fit of the high energy neutrino ($E > 35\,\mathrm{TeV}$) flavour ratio ν_e:ν_μ:ν_τ at Earth as depicted using a flavour triangle. The 68 % confidence region includes the 1:2:0 (at source) $\rightarrow$ 1:1:1 (at Earth) scenario which is consistent with pp and $p\gamma$ collision scenarios. Pure electron-neutrino composition at source is excluded at more than 2σ confidence [43].

of the ratio. It is not possible to discriminate between NC and CC neutrino interactions in the ice and the event morphologies are identical between neutrinos and their anti-neutrino counterparts of the same flavour. Cascades are consistent with ν_e and ν_τ scenarios, with the degeneracy only broken by the energy lost to τ-decay in the latter and the lack of observation of the Glashow resonance of $\bar{\nu}_e$ [68]. The future observation of a double-bang signature of tau-neutrino at multi-PeV energies may help resolve this situation. Current constraints on the flavour composition are consistent with a cosmic-ray origin, but it is not the only possibility. The distribution of possible at-source flavour compositions is displayed with a "flavour triangle" shown in figure 3.10.

3.5 Summary

The IceCube Neutrino Observatory has observed a diffuse astrophysical neutrino flux at $E^2\Phi \sim 10^{-8}\mathrm{GeVcm}^{-2}\mathrm{s}^{-1}\mathrm{sr}^{-1}$ [41] [6] [43] with a spectral index of $\Gamma = -2.2$, with fairly consistent results between the starting event analyses and the up-going muon analysis (see figures 3.11(a) and 3.11(b)). This marks the first detection of steady neutrino emission from beyond the solar system. No significant point sources have been observed in directional analyses and no significant correlation with catalogues of potential sources have been found. Instead, upper limits have been established on the brightest point source, ranging from $3 \times 10^{-11}\mathrm{TeVcm}^{-2}\mathrm{s}^{-1}$ in the southern sky to $2 \times 10^{-12}, \mathrm{TeVcm}^{-2}\mathrm{s}^{-1}$ at the equator [4]. These results have been used to constrain different classes of galaxies and other objects as neutrino sources. The flavour composition of the astrophysical sample is consistent with the (1:2:0) at-source ratio expected for cosmic ray acceleration. A major expansion to the detector volume would greatly increase event statistics. This combined with more sensitive point source analyses may reveal sources of cosmic neutrinos [46].

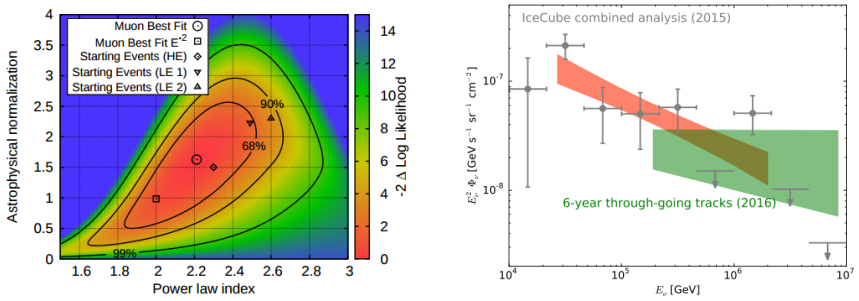

(a) (b)

Figure 3.11: (a) The likelihood profile for the up-going astrophysical flux normalization and spectral index above 100 TeV, with the best fit for starting event analyses (HESE, MESE, LESE) shown with a diamond, upside-down triangle and right-side up triangle respectively, and the best fit for up-going muons shown with a circle and a square for the case of $\gamma = -2$ [43]. (b) The energy flux 95 % CL range of the starting analyses (highlighted in red) and the 6 year up-going muon sample (highlighted in green).

Chapter 4

Astrophysical Neutrino Sources

As described in the previous chapters astrophysical neutrinos are expected to be produced by cosmic ray interactions, either near the cosmic ray accelerator sites or in regions of high gas and radiation density nearby. The various proposed cosmic sources of neutrinos are discussed in this chapter. Note that "galactic" sources refer to objects considered within a given galaxy (not necessarily the Milky Way) while "extra-galactic" sources belong to specific classes of galaxies and necessarily exist outside of the Milky Way. The measurement of the astrophysical diffuse flux and upper-limits placed on point source strengths can be used to limit the permitted space of source luminosities and abundances (or densities). However estimating neutrino luminosity per source is highly model dependent. We expect that neutrino luminosity should scale with γ-ray luminosity, but this depends on the hadronic fraction of the γ-ray emission which is usually unknown. The situation is worse when no γ-ray emission is detected, due to possible source attenuation. Nevertheless, constraints on source strengths and abundances are summarized in figure 4.1.

4.1 Galactic Sources

The measured cosmic ray luminosity inside the Milky Way implies some level of neutrino emission is expected. In particular neutrino production is expected from second order Fermi acceleration in galactic supernova remnants and from the occasional gamma-ray burst (GRB). So far no galactic excess is observed but may become visible with increased data [43].

4.1.1 Supernova Remnants

A supernova is an enormous explosion of a massive star marking the final stage of the star's evolution. Supernovae release an enormous amount of energy on the order of $E \sim 10^{51}$ erg or 10^{44} J and are an important driver of many astrophysical processes, including cosmic ray acceleration and star-formation. Type Ia Supernovae occur exclusively in binary systems with a white dwarf accreting matter from its companion star. At the point when the white dwarf's mass exceeds the Chandrasekahr limit ($M_{WD} \geq 1.3 M_{\odot}$) the gravitational pressure exceeds the electron-degeneracy pressure holding up the star and the white dwarf rapidly contracts to nuclear density forming a neutron star. The released energy radiates outwards in a supernova explosion. The luminosity of Type Ia supernova are uniform such that they are used as a "standard candle" by astronomers.

Most other supernovae are triggered by collapse of the core at the final stage of a massive star's ($M \geq 8 M_{\odot}$) evolution (see section 1.4.2). After cycling through fusion of successively more massive elements, the core of a massive star is converted to iron, the element with the highest binding energy per nucleon. At this point, nuclear fusion no longer releases additional

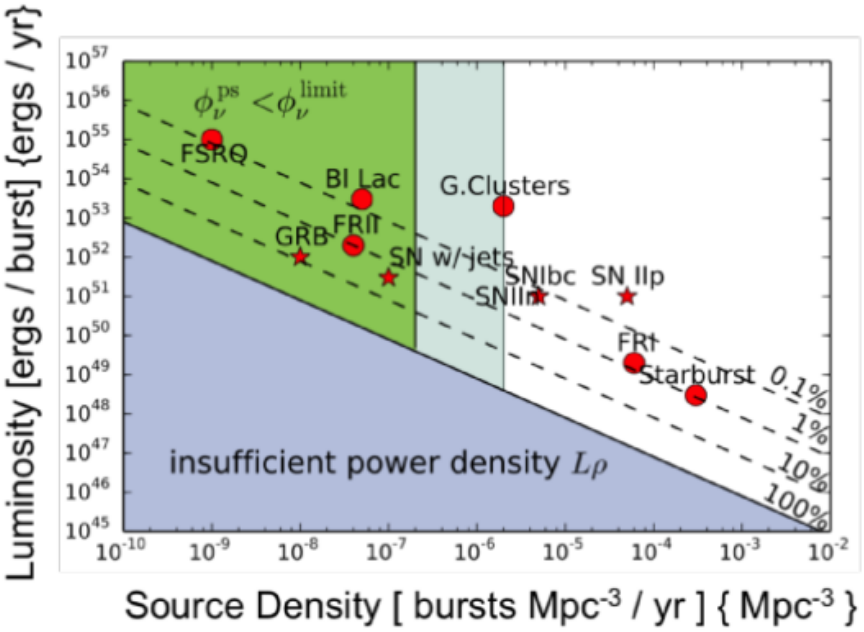

Figure 4.1: Constraints on potential transient and steady sources responsible for the diffuse astrophysical flux detected by IceCube [53]. Under a given red-shift evolution model, we can use the measured energy flux to estimated the range of source densities and luminosities permitted by the observation of the diffuse flux. Individually luminous but rare sources like Flat Spectrum Radio Quasars are shown on the upper left, while common but dimmer sources (starburst galaxies) are shown on the lower right.

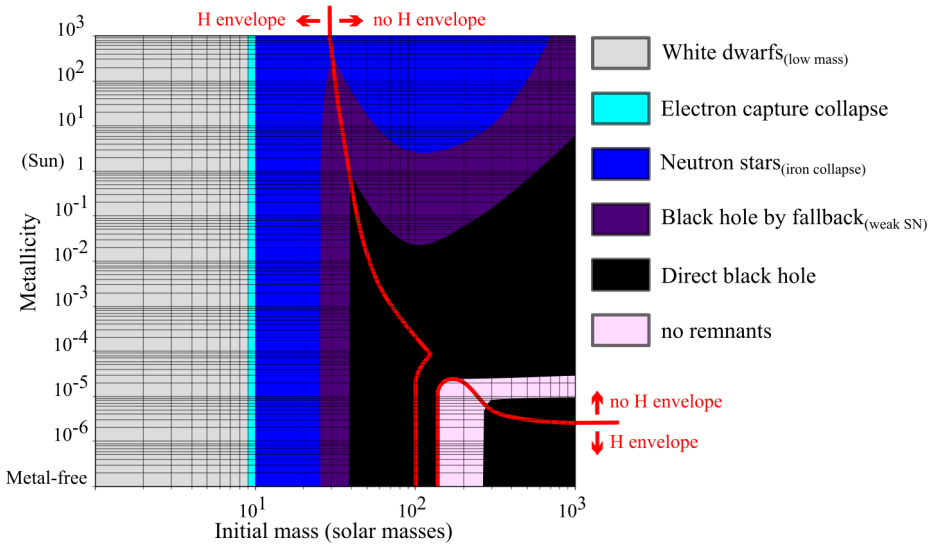

Figure 4.2: Remnants of post main-sequence stars by metallicity and stellar mass. Low mass stars ($M < 8M\odot$) become white dwarfs after the red giant or, in the case of red dwarves, blue dwarf phase while high mass stars undergo supernova explosions leaving behind a neutron star, black hole or leave no remnant [38].

energy and the core can no longer release sufficient radiation pressure to balance the gravitational pressure of the star. The collapse of the core initiates a violent shock wave through the outer layers culminating in a catastrophic explosion and destruction of the star. The majority of the energy released (99 % or 10^{53} erg) is carried by neutrinos escaping the core in the first few minutes of the collapse(see section 1.4.2), $\sim$ 1 % (10^{51}erg) in kinetic energy of the ejecta and $\sim$ 0.1 % in the subsequent electromagnetic radiation[48]. The fate of the core depends on the mass and metallicity of the star (see figure 4.2).

The rest of the star's material, several solar masses, is flung outwards as *ejecta* at a speed of $v_P \sim 10^4 \text{kms}^{-1}$ ($0.2c$, faster than the speed of sound of the interstellar medium $c_{ISM} \sim 10\text{kms}^{-1}$. The resulting shock wave radiates outwards piling up the ISM and its associated magnetic field (see figure 4.3). The shock wave velocity v_S is dependent on the ejecta velocity and on the specific heat of the ISM gas $\gamma = 5/3$ (monatomic as the heat of the supernova will have ionized the gas). In the idea case for a shock (Mach number $M \gg c_{ISM}$) the compression ratio R is $R > \rho_{shocked}/\rho_{unshocked} > 4$. Irregularities present in the ISM result in magnetized clouds that accelerate particles in the Fermi model (see section 2.1.3), scattering them in a randomized direction with an average gain of energy. At the interface of the supernova shock, particles travelling "downstream"(i.e. into the shock) and entering a magnetized cloud will have an enhanced energy gain in the observer frame compared to normal Fermi acceleration. In other words, diffusing charged particles gain energy from the shock itself in addition to acceleration in the associated magnetic fields, a process known as second-order Fermi acceleration. Crucially the particles are trapped in continuous acceleration across the shock front by the magnetic field, escaping when they reach an energy such that the gyroradius is larger than the size of the supernova remnant [30]. One can predict the cosmic ray energy spectrum $\phi_{CR}(E) \propto E^{-2}$ under the simplistic model of a parallel planar shock front of infinite extent where the cosmic rays act as test particles. In reality supernova shock fronts are spherical, not linear and the cosmic rays exert pressure upon the shock; slowing down the up-streaming plasma and resulting in:

- Increased compression.
- Changes to the velocity of the clouds.
- Non-linear magnetic amplification.
- A cosmic-ray spectrum softer than E^{-2} at low energies and harder at higher energies.

The cosmic ray pressure eventually slows down and dissipates the shock on a time-scale of $t_{SNR} \sim 10^5$ years. Supernova Remnants are among the most likely locations for cosmic rays, indeed several of them have been observed by VHE γ-ray telescopes such as H.E.S.S, VERITAS and MAGIC. Indeed a simple calculation shows that supernova remnants can power the total galactic cosmic ray luminosity (taken from the cosmic ray flux above the knee), given an observed supernova rate of $R_{SN} = 0.01\text{yr}^{-1}$, a kinetic energy per supernova of $E_{SN} = 10^{51}$erg and an assumed efficiency of $\eta = 0.1$ for converting the shock's kinetic energy to cosmic ray energy [18].

$$L_{CR} = \eta E_{SN} R_{SN} \sim 2 \times 10^{41} \text{ergs}^{-1} \tag{4.1}$$

The compressed gas at the shock, in addition to accelerating cosmic rays, contain an enhanced density of target protons and nuclei for pion production. However deriving the proportion of cosmic rays that interact with target gas and hence lose energy to pions and ultimately photons and neutrinos requires comparing the escape time t_{escape} with the time until interaction $t_{interaction}$ which in turn are dependent on the local gas density and magnetic field strength.

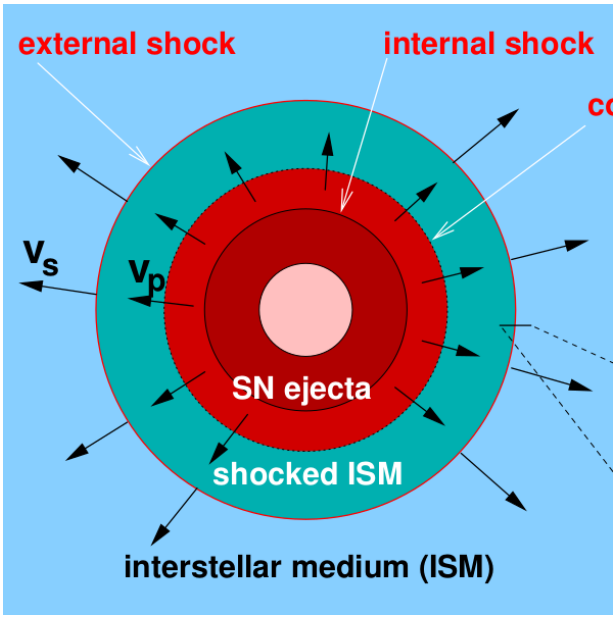

Figure 4.3: Illustration of supernova shock wave. The supernova ejecta emanate from the location of the explosion, colliding with surrounding gas creating a shock wave that travels ahead of the ejecta passing through the surrounding medium.

4.1.2 Gamma-Ray Bursts

Gamma-Ray Bursts (GRBs) are intense flashes of γ-ray emission lasting on an average time-scale of $\Delta t_{burst} = 2$ s for "short' GRBs to $\Delta t_{burst} = 30$ s for "long" GRBs. Long GRBs comprise 70 % of known GRBs and are theorized to be a special case of a supernova or hypernova, in which a rapidly rotating massive star collapses to form a neutron star or black hole and the subsequent burst of radiation is strongly beamed along the axis of rotation. After the initial flash of gamma-rays a longer duration "after-glow" follows in longer wavelengths (X-ray, optical, radio etc.). Short GRBs are associated with "kilonovae" triggered by the merger of a binary neutron star system.

GRBs are expected to accelerate protons and other charged particles to extremely high energies of $E \sim 10^{20}$ eV via Fermi acceleration in their jets. These jets may also generate γ-rays and neutrinos via photohadronic and lepto-hadronic collisions according to various models of GRB jets. One widely discussed model is that of the "choked jet" where the bulk of the photon emission is unable to escape the stellar envelope. The existence of choked jet GRBs would mean there would be many more GRBs than found by current observations [23]. Calculating neutrino emission requires taking into account the expected proton flux and using the known magnetic field, photon, electron and proton densities to find the energy lost to pion production as well as other cooling processes: [51]. An easier conceptualization is to take the time taken for available protons to accelerate versus to cooling down time due to meson production, synchrotron emission and adiabatic cooling:

$$t_{acc}^{-1} > t_{cool}^{-1} = t_{dyn}^{-1} + t_{syn}^{-1} + t_{p\gamma}^{-1} \tag{4.2}$$

The acceleration time can be estimated as $t_{acc} = \epsilon_p / ceB$ where ϵ_p is the proton energy in the jet frame. The adiabatic cooling time is similar to the dynamical time: $t_{dyn} = r_{jet}/c\Gamma$ with r_{jet} representing the radius of the jet and Γ representing the bulk Lorentz boost relative to the star. The synchrotron time for particle species i (which can denote a proton, photon, electron etc.) is: $t_{i,syn} = 6\pi m_i^4 c^3/(m_e^2 \sigma_T B^2 \epsilon_i)$, where σ_T is the Thomson cross-section. Finally the meson

production rate is:

$$t_{p\gamma}^{-1} = \frac{c}{2\gamma_p^2} \int_{m_\pi c^2}^{\infty} d\tilde{\epsilon}_\gamma \sigma_{p\gamma} \kappa_{p\gamma} \tilde{\epsilon}_\gamma \int_{m_\pi c^2/(2\gamma_p)}^{\infty} d\epsilon_\gamma \epsilon_\gamma^2 \frac{dn}{d\epsilon_\gamma} \tag{4.3}$$

where $\gamma_p = \epsilon_p/(m_p c^2)$, $\tilde{\epsilon_\gamma}$ is the target photon energy in the proton's reference frame, $\sigma_{p\gamma}$ and $\kappa_{p\gamma}$ are the cross section and in-elasticity of photo-meson production respectively. The energy threshold $m_\pi c^2 = 145$ MeV for pion production is used as the pion is the meson of lowest mass and highest stability. The vast majority of these interactions produce pions which decay into muons and muon neutrinos (see chapter 2) via the interaction channel: $p + \gamma \rightarrow n + \pi^+$. We define the meson production efficiency as $f_{p\gamma} = t_{p,cool}/t_{p\gamma}$ and hence we can estimate the muon neutrino energy spectrum as [51]:

$$E_{\nu_\mu}^2 \frac{dN_{\nu_\mu}}{dE_{\nu_\mu}} \sim \frac{1}{8} f_{p\gamma} f_{\pi,sup} E_p^2 \frac{dN_p}{dE_p} \tag{4.4}$$

where $E_\nu = 0.05 E_p$ on average across flavours. Note that one must account for suppression of the pion via cooling: (we cannot assume that pions are interaction-less in a jet) $f_{\pi,sup} = 1 - \exp(-t_{\pi,cool}/t_{\pi,dec})$. We find the decay time $t_{\pi,dec} = \gamma_\pi \tau_{pi}$ ($\tau_{pi^\pm} = 2.6 \times 10^{-8}$ s) and the cooling rate $t_{\pi,cool}^{-1} = t_{\pi,syn}^{-1} + t_{\pi,dyn}^{-1}$. The pion cooling results in a spectral break in the neutrino spectrum at $E_\nu = \sqrt{3\pi m_\pi^5 c^5 \Gamma^2/(8 m_e^2 \sigma_T B^2 \tau_\pi)}$. The muons of course subsequently decay into neutrinos and positrons and one must take into account muon suppression from interactions in the jet $f_{\mu,sup}$ and we find the spectra for ν_e and $\bar{\nu}_\mu$:

$$E_{\nu_e}^2 \frac{dN_{\nu_e}}{dE_{\nu_e}} = E_{\bar{\nu}_\mu}^2 \frac{dN_{\bar{\nu}_\mu}}{dE_{\bar{\nu}_\mu}} \sim \frac{1}{8} f_{p\gamma} f_{\mu,sup} f_{\pi,sup} E_p^2 \frac{dN_p}{dE_p} \tag{4.5}$$

Another break due to muon cooling is observed at $E_\nu = \sqrt{3\pi m_\mu^5 c^5 \Gamma^2/(8 m_e^2 \sigma_T B^2 \tau_\mu)}$. Hence the flavour mixing at a GRB does not necessarily follow 1:2:0 but instead one must have knowledge of the local radiation densities and magnetic field strengths among other things [51].

4.2 Extragalactic Sources

The isotropic distribution of neutrino arrival directions measured by IceCube has suggested that astrophysical neutrinos are extra-galactic in origin with different classes of galaxies considered as individual sources. The majority of extra-galactic sources can be classified as active galaxies or star-forming/starburst galaxies, with the production region contained within the active galactic nucleus and starburst region respectively. Note that these two sources may not be mutually exclusive, active galaxies are often host to high levels of star-formation. Active galaxies and starburst galaxies have been extensively catalogued and their populations have been modelled across cosmic epochs, with the latter distribution following the cosmic star-formation rate. By combining the density of different source classes over cosmological epochs with a best-guess of neutrino luminosity per source, once can calculate the nearest observable neutrino source and compare this with established upper limits [64]. The densities and luminosities of neutrino sources permitted by the point source and diffuse upper limits are displayed in figure 4.4.

4.2.1 Active Galaxies

Active galaxies host active galactic nuclei (AGN) in their centre which are the sources of extraordinarily luminous electromagnetic radiation, at least equal to the collective emission of the rest of the galaxy or several orders of magnitude higher. AGN are so luminous that the earliest detected examples were mistaken by astronomers for stars inside the Milky Way. The emission is primarily powered by accretion of material spiralling in towards a super massive black hole,

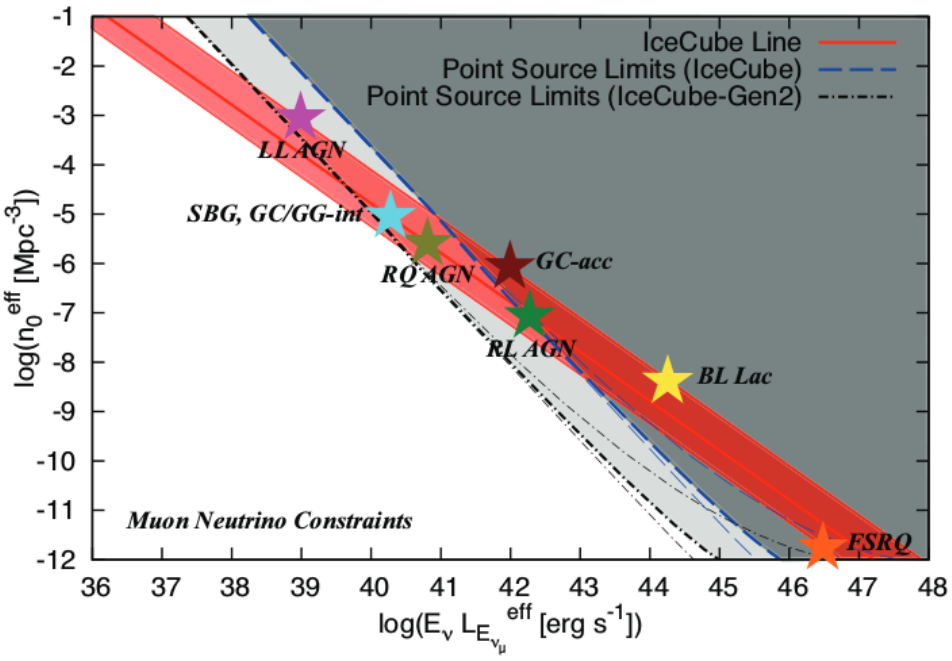

Figure 4.4: Constraints on the logarithmic density (y-axis) and energy luminosity (x-axis) of steady cosmic neutrino sources measured by IceCube [64] under a variety of evolutions of source density. The IceCube line (red) represents the limits imposed by the measurement of the diffuse flux. The blue line represents the point source limits and the black line represents the limits expected from IceCube-Gen2. The spread in the IceCube line accounts for the evolution of source density $n(z)$ under different models including $n(z) \propto (1+z)^0$ (flat), $n(z) \propto (1+z)^2$ (approximate star-formation rate) and $n(z) \propto (1+z)^3$ (the distribution of AGN). The effects of the evolution model on the point source limits are shown with fainter coloured lines.

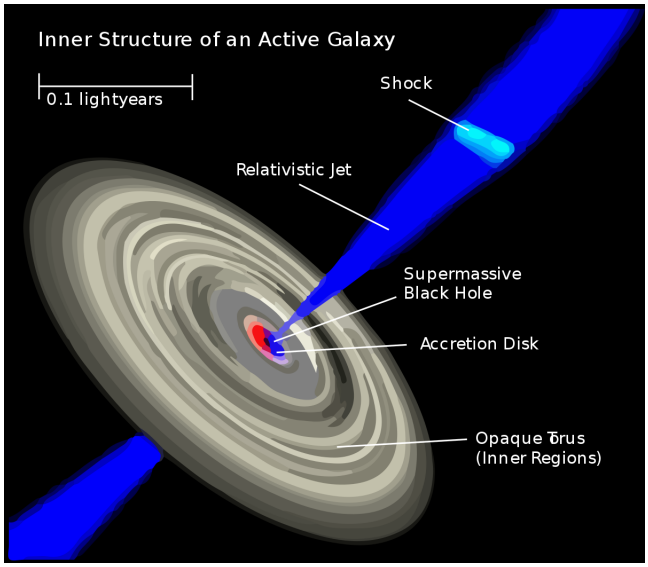

Figure 4.5: An illustration of an active galactic nucleus according to accepted models. Relativistic jets emanate from both poles of supermassive black hole and are enveloped by a torus of thick dust and gas which often obscures the active region from side on observers.

the material in the accretion disk is heated to high temperatures and radiates X-ray photons before falling below the event horizon. AGN also feature relativistic jets, highly collimated beams ($\Delta\theta \sim 1^0$) of high energy plasma erupting from the pole. The jets extend outside of the galactic plane perpendicular to the disk, varying widely in size from a few parsecs (in the case of Seyferts) to millions of parsecs in length (M87). The active core contains thermally excited gas that rises out from the plane which gradually cools down by emitting thermal radiation. The core is usually enveloped by a torus of optically thick gas and dust which is heated by the gas emission from the active core and cools by emitting in the far infra-red. See figure 4.5 for a visual description of an AGN.

The causes of AGN jets are still undetermined, but they are likely formed by particle acceleration by the magnetic field of the black holes and powered by the black hole's rotation. Various classes of AGN are defined using the orientation of the jet to the observer, the level of radio emission (AGNs can be divided into "radio-loud" and "radio-quiet" categories), the presence of emission lines and other features. The observation of different classes of AGN is summarised in figure 4.6. Active galaxies are among the most discussed extra-galactic neutrino sources, with neutrino and γ-ray emission expected from cosmic ray acceleration in the jets and subsequent collisions with high density photon fields within.

Seyferts

Radio-quiet AGN include Seyfert galaxies and Quasars or Quasi-Stellar Objects (QSOs). Seyfert galaxies are the most abundant type of active galaxy (accounting for $\sim 10\%$ of all galaxies) and feature a nucleus with a luminosity approximately equal to the remainder of the galaxy, while QSOs have optical luminosity several orders of magnitude higher. The core of a Seyfert galaxy is usually hosted by a spiral galaxy, and look like normal spiral galaxies when viewed in visible light, with the excess emission apparent at other wavelengths. Seyferts can be further divided into Type 1 and Type 2. Type 1 Seyferts contain broad emission lines, with both allowed lines (HI, HeI and HeII) and broad forbidden lines (OIII) as well as occasional narrow allowed lines. Type 2 Seyferts contain only narrow allowed and forbidden lines (note that the term "forbidden lines" is a slight misnomer, as the electron transitions that cause them are highly improbable

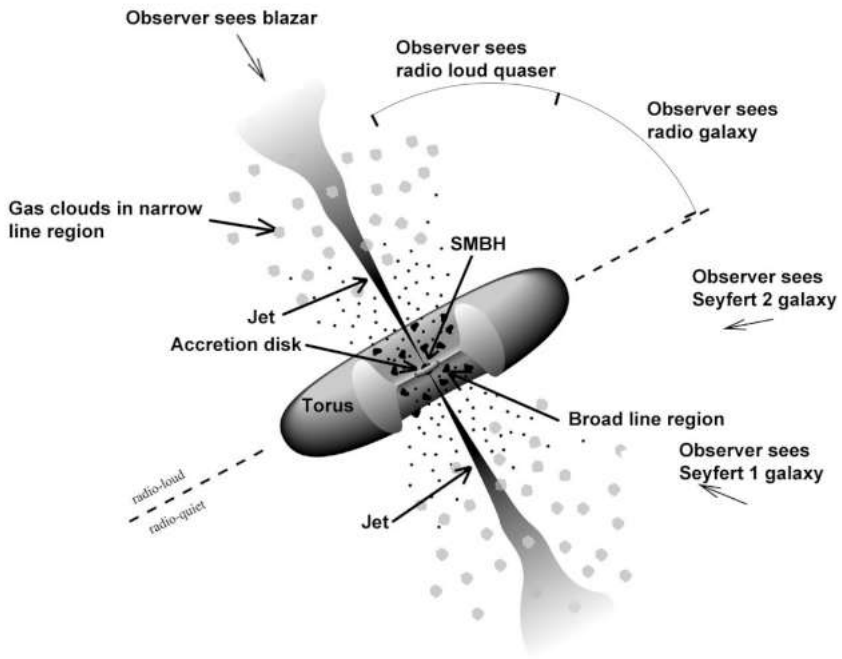

Figure 4.6: Diagram depicting the Unified Model of Active Galactic Nuclei. Different classes of AGN are defined by the observer's orientation with respect to the jet and the galactic plane [21].

but not forbidden). It is believed that all Type II Seyfert are in fact Type 1 Seyferts where the active nucleus is obscured by toroidal dust clouds. These dust clouds obscure broad emission from the hot gas in the centre, allowing only the cooler outer gas to be observed. The observation of Type I or II Seyfert is contingent on the orientation of the observer to the nucleus. The dust envelope is heated by intense UV radiation from the accretion disk, cooling down by emitting in the far infra-red. Starburst galaxies (see section 3.2.2) are also highly luminous in the far infra-red, owing to heating of dust by bright O and B type stars, and so care must be taken to differentiate between Seyfert and starburst galaxies using the shape of the infra-red spectrum and the presence of contiuum radio emission in starburst galaxies.

Like other AGN, Seyferts contain relativistic jets, although they are relatively weak with the most powerful only extending to a few parsecs. Colliding blobs within the jet and the formation of shocks can accelerate protons up to 10^{18} eV which can in turn produce neutrinos via photomeson interactions.

Blazars

Blazars are active galactic nuclei where the jet is pointed directly towards Earth, and are only observed inside elliptical galaxies. The line of sight orientation leads to enhancement of the emission from relativistic beaming and can explain the higher polarization and variability than that of non-blazar AGN as well as apparent superluminal motion in the jet itself. Under a Unified Model of AGN, highly variable blazars are related to radio-loud galaxies while BL Lacertae Objects (BL Lacs) are intrinsically radio-quiet.

Shocks in the jet would be the site of cosmic ray acceleration, with subsequent collisions of cosmic rays with photons in the jet producing γ-rays and neutrinos. Although the mechanism is largely the same between blazar and Seyfert type sources, the luminosity of blazars is higher by around 3 orders of magnitude for BL Lacs to 5 orders of magnitude for Flat Spectrum Radio Quasars (FSRQs). Blazars are far rarer than Seyfert galaxies, with a local cosmic density around

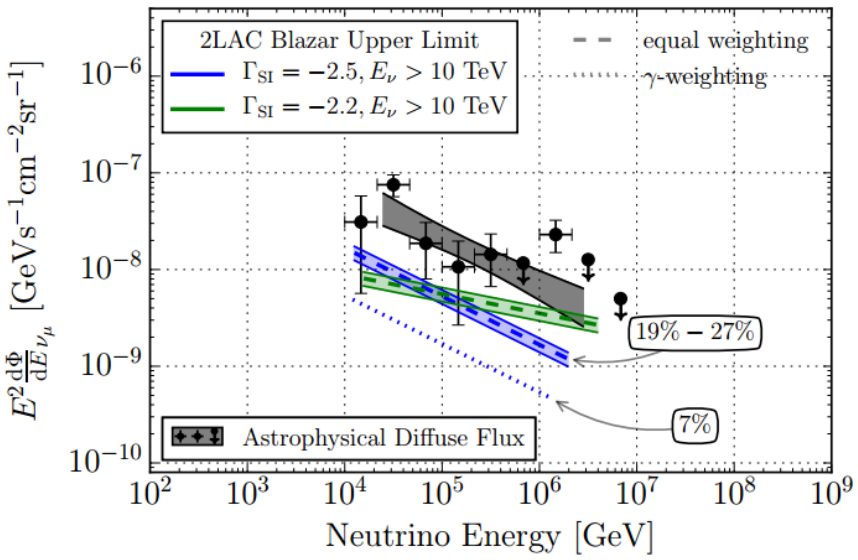

Figure 4.7: Upper limits to the cumulative blazar energy flux established by the 2LAC-Fermi blazar stacked point source analysis [5]. The limits assuming spectral indices above $E > 10\,\text{TeV}$ are considered, shown in green for $\Gamma = 2.2$ and blue for $\Gamma = 2.5$. The results are shown for equally weighted blazar (blazars with equal neutrino intensities) and for γ-weighted blazars where the neutrino intensity is proportional to the γ-ray intensity measured by Fermi-LAT between 100 MeV and 100 GeV). The data points show the measurements of the astrophysical muon-neutrino flux, with the shaded black area indicating the uncertainty in the flux magnitude and spectral index.

2 to 3 orders of magnitude lower for BL Lacs and FSRQs respectively (as shown in figure 4.4 in the constraints on BL Lacs and FSQRs) [64]. More than 862 γ-ray emitting blazars have been identified and catalogued by Fermi-LAT [65] [13]. γ-ray emission can be used to predict the neutrino flux assuming a completely hadronic origin for γ-ray emission. Although the exact ν/γ proportionality may vary considerably between individual sources, an average ratio can be established by measuring the correlation between the positions of γ-ray blazars and the arrival directions of astrophysical muon-neutrinos. The results of stacking analyses comparing the Fermi 2LAC catalogue of γ-ray blazars with up-going muons measured by IceCube found no significant correlation overall and none for any of the subcategories of blazars including BL Lacs, FSRQs, ISPs or LSPs. This result indicated that γ-ray blazars could account for no more than 27 % of the astrophysical neutrino flux measured by IceCube (see figure 4.7). Collectively blazars do not dominate the neutrino sky and so other sources, such as star-forming galaxies need to be investigated as possible neutrino sources.

4.2.2 Star-forming and starburst galaxies

Starburst galaxies are thought to be engines of cosmic ray production, and due to the high densities of interstellar gas and radiation, may act as cosmic ray "calorimeters" i.e. the neutrino emission via pion decay may be a metric of the cosmic ray flux at certain energies [88] . The limited observations of starburst galaxies by γ-ray telescopes leave an unclear picture of the situation. Fermi-LAT's observations of the γ-ray flux of starburst galaxies are at energies around three orders of magnitude lower than the astrophysical neutrino flux measured by IceCube hence there is a strong systematic induced by the assumptions of the power-law at high energies.

A large proportion of galaxies are hosts to star-formation, as clouds of atomic and molecular

gas undergo gravitational collapse. As the clouds are compressed, the density and temperature rises, as gravitational energy is converted into thermal energy. At the centres of collapse eventually a critical temperature is reached allowing fusion of hydrogen. Star-formation is a well studied phenomenon as astronomers can view virtually every stage of stellar synthesis within the Milky Way. In the galaxy, star-formation can be initiated by supernova shocks, gravitational perturbations in the spiral arms and compression of clouds from radiation pressure from hot O and B type blue super giants. On larger scales, galactic mergers lead to rapid run-away star-formation, in some cases creating "starburst" regions in which all available gas is converted into stars on a relatively short time scale ($t \leq 10^6$yr). High star-formation rates correlate with higher populations of short-lived high mass stars such as the O and B blue super-giants. O and B stars are often born in close proximity to each other and given their short lives do not have time to diffuse into the galactic plane and therefore are usually found in clusters called OB associations. Being the hottest main-sequence stars, with surface temperatures ranging from 10,000 K to more than 50,000 K, a large proprotion of surface radiation is in the blue and ultraviolet. Enormous surface areas ensure that the stars are highly luminous, accounting for the majority of stellar emission in the blue and ultraviolet despite forming less than 0.1 % of the stars. UV photons are absorbed by optically thick dust in the starburst region which warms to 100-200 K and gives off thermal radiation in the far-infrared. Thus infrared emission is a reliable tracer of star-formation in general [61] and the most luminous infrared galaxies are star-forming galaxies. The stellar winds from OB associations lead to cosmic ray acceleration and associated γ-ray and neutrino production. Since the starburst phase occurs on a time-scale an order of magnitude greater than the lifetime of O and B type stars, the supernova rate is in equillibrium with the star-formation rate and the supernova shocks power cosmic ray acceleration in the medium. The thick gas and intense stellar radiation in starburst regions lead to abundant pp and $p\gamma$ collisions producing γ-rays and neutrinos [67].

Star-formation can be measured across cosmological time-scales across multiple bands including UV, infrared, radio contiuum and far-infrared emission and molecular recombination lines. Combining these methods, one can trace the history of the cosmic star-formation rate (see figure 4.8) across redshifts as described by the equation 4.6:

$$\Psi(z) = 0.015 \frac{(1+z)^{2.7}}{1+[(1+z)/2.9]^{5.6}} \, [\mathrm{M_\odot yr^{-1} Mpc^{-3}}] \tag{4.6}$$

Following the reionization epoch and the cosmic dark ages the star-formation rate density increased reaching a peak at $z \sim 1.9$ or 3.5 Gyr and decreased after $z \sim 1$ with an e-folding timescale of 3.9 Gyr. The Universe was a more active place in the past, stars formed at a rate nine times higher during the peak of cosmic star-formation than today [61]. Around 25 % of the current stellar mass density formed at $z > 2$, prior to the peak of star-formation and another 25% formed after $z = 0.7$ (roughly half way through the lifetime of the Universe). The smooth evolution of the star-formation rate density implies that the star-formation is dominated by "main-sequence" galaxies, ones that form stars at a low but stable rate across large timescales. Starburst galaxies play a sub-dominanat role in overall star-formation across the Universe, accounting for $\sim 10\%$ of the star-formation rate before $z > 2$, $\sim 20\%$ at $1 < z < 2$, and $\lesssim 5\%$ after $z > 1$ [57].

The connection between star-formation and cosmic ray acceleration is evidenced by observation of γ-ray emitting starburst galaxies by Fermi-LAT [90]. Collectively star-forming galaxies account for between 43 % and 91 % of the isotropic γ-ray background (IGRB) intensity measured above 1 GeV [59]. Very high energy γ-rays have been observed in the two closest starburst galaxies: M82 and NGC 253 by VERITAS and HESS respectively [47], and both observatories

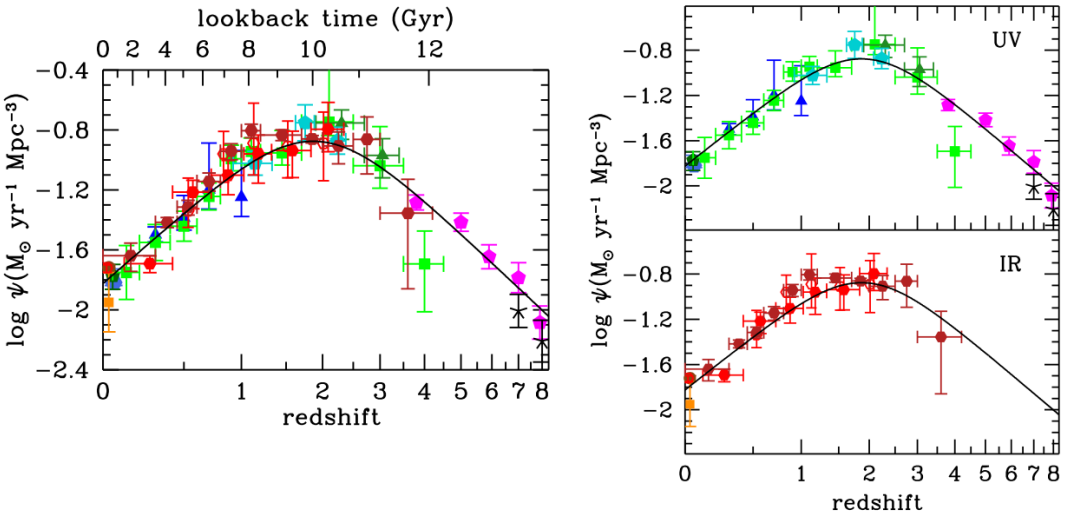

Figure 4.8: The evolution of the star-formation rate density from the cosmic dark ages to the present epoch based on UV and infra-red observations [61]. The star-formation rate density reached its peak around $z = 1.9$ (or 3.5 Gyr after the Big Bang) and declined exponentially thereafter.

have placed upper limits close to the expected flux from Arp 220, the most infra-red luminous starburst galaxy in the local Universe [27]. Starbursts are expected to be weaker overall γ-ray and neutrino producers than blazars and other AGN but are known to be far-more numerous with more starbursts in the local Universe [64]. The connection between star-formation and γ-ray emission in starbursts is supported by a strong correlation between bolometric γ-ray luminosities $L_{\gamma,1-100\mathrm{GeV}}$ and infra-red luminosities $L_{\mathrm{IR},8-1000\mu m}$ [75] as shown in figure 4.9. The relation can be described by the following log-linear relation at 5.7σ confidence [59]:

$$\log_{10}(L_\gamma/\mathrm{ergs}^{-1}) = \alpha \log_{10}(L_{\mathrm{IR}}/10^{10}\mathrm{L}_\odot) + \beta \tag{4.7}$$

where $\alpha = 1.18 \pm 0.15$ determines the power relation (nearly linear) between the respective luminosities and $\beta = 38.49 \pm 0.24$ governs the difference in orders of magnitude [59]. This would imply that local neutrino luminosity should scale with infra-red luminosity in a similar fashion in regions of intense star-formation. However this assumes a purely hadronic origin for the observed γ-rays. High star-formation rates will also lead to an abundance of remnant pulsars which produce powerful winds of electrons and positrons which produce γ-rays via the leptonic acceleration mechanisms described in section 2.3.1. In fact the starburst γ-ray flux can be equally explained by hadronic and leptonic mechanisms [67], an ambiguity that needs to be resolved by the next generation of higher resolution γ-ray observatories like the Cherenkov Telescope Array (CTA) [67].

Even if γ-rays from starburst galaxies are predominantly or entirely hadronic in origin, the observed correlation paints an ambiguous picture with respect to neutrinos. The most extensive observations of γ-ray starbursts by Fermi-LAT measure photon energies up to 100 GeV at least 3 orders of magnitude below the energy threshold at which IceCube can distinguish an astrophysical neutrino flux. Even HESS and VERITAS can only measure γ-ray emission up to this threshold. So any extrapolation of γ-ray fluxes to neutrino fluxes is subject to high uncertainty from the unknown spectral index. For example, *Bechtol, Ahlers et al.* [17] claimed to limit the starburst contribution to the IceCube neutrino flux to less than 28 % by extrapolating the starburst component of the IGRB to neutrinos at higher energies [17]. Their value was highly sensitive to the assumed spectral index above 100 TeV, with harder spectra leading to a larger

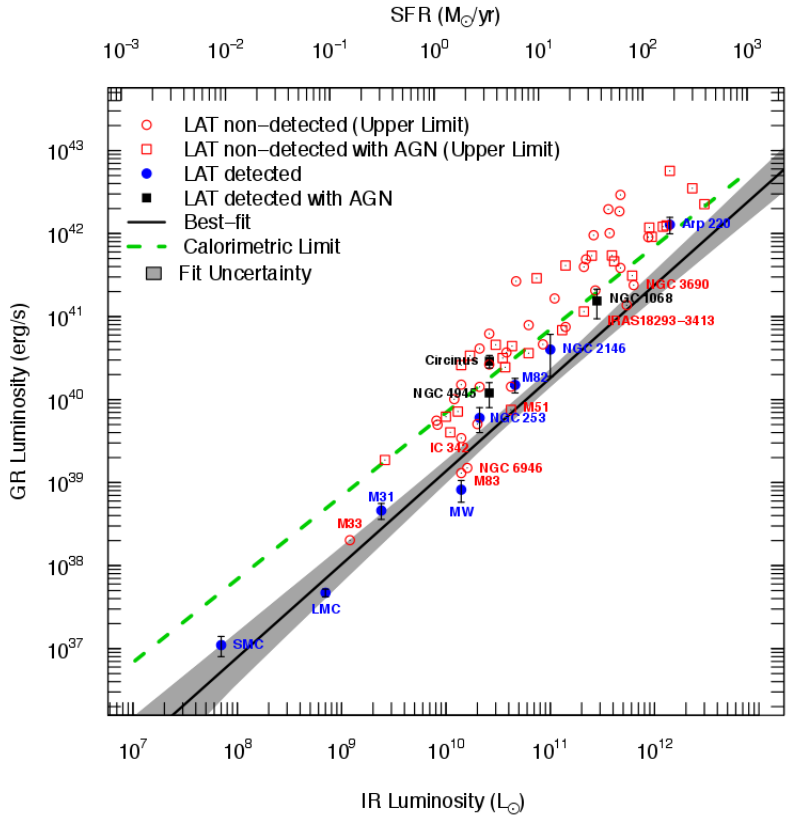

Figure 4.9: Correlation between theγ-ray (Fermi-LAT) and far infra-red (observations taken from IRAS, Spitzer and Herschel) luminosity in star-forming and starburst galaxies [75]. The effective star-formation rate is display on the upper x-axis, showing the relation of star-formation and high energy γ-ray production.

share of the IceCube flux and the share increasing with energy.

- Spectral index $\gamma = -2.3 \rightarrow \Phi_{\nu,\mathrm{SFG}}/\Phi_{\nu,\mathrm{IceCube}} = 0.1$
- Spectral index $\gamma = -2.3 \rightarrow \Phi_{\nu,\mathrm{SFG}}/\Phi_{\nu,\mathrm{IceCube}} = 0.3$ (for $E \geq 100$TeV) and 0.6 (for $E \geq$ PeV)

Predicting the spectral index becomes more problematic as poorer photon statistics at higher energies leads to greater uncertainty in the fit of the γ-ray spectrum. Measurements of M82 and NGC 253 by HESS and VERITAS disfavour hard spectral indices at 100 TeV [56]. IN chapter 6 we analyse the effects of the spectral index on the predicted starburst flux.

Moreover the high densities of gas and background photons in starbursts may render them opaque to γ-rays above 100 TeV [47], leading to an underestimation of the neutrino flux if directly scaled to observed γ-rays. In the presence of gas γ-ray photons pair-produce electrons and positrons which can up-scatter ambient photons to γ-ray energies via inverse Compton scattering. This sometimes leads to particle cascades inside the starburst region. The resultant cascades may be evident in increased γ-ray emission at lower energies, increasing the flux by 10 %- 45 % in M82 and NGC 253[47] in the 1 to 100 GeV range. The optical thickness to pair-production in starbursts increases with photon energy, reaching $\tau_{\gamma\gamma} = 1$ at around 10 TeV [47]. The multi-source nature of the IGRB, the uncertainties in the spectral index of γ-rays at high energies, the uncertain hadronic to leptonic ratio and the presence of γ-ray attenuation, significantly complicate the picture for starburst neutrinos. This situation may be resolved by searching for directional associations between astrophysical neutrinos and nearby starburst galaxies.

4.3 Summary

The isotropic distribution of neutrinos measured by IceCube favours an extra-galactic origin scenario. Blazars and related Active Galactic Nuclei have been widely discussed as sources but the lack of directional correlation limits them to accounting for less than 27 % of the neutrino flux. Seyfert galaxies are also of interest in accessing neutrino origins. Starburst galaxies are widely considered highly likely producers of neutrinos but the picture from γ-ray emission makes the actual level of neutrino emission highly uncertain. An extensive directional analysis of starburst galaxies may help resolve these ambiguities.

Chapter 5

Cross Correlation between starburst galaxies in the IRAS catalogue and High Energy Starting Events

If there is a correlation between neutrino emission and star-formation in galaxies, then we expect neutrino arrival directions to point towards the brightest starburst galaxies. This chapter examines a published study "Do high energy astrophysical neutrinos trace star formation?" by Lunadrini, Emig and Windhorst (2015) [24] which examines the degree of directional correlation between the three year high energy starting events (HESE) sample and nearby bright galaxies belonging to different galactic classes, including starburst galaxies, that are suspected to be the source of cosmic ray powered neutrino production. A weak correlation is claimed between the three year HESE sample and seven starburst galaxies selected from the IRAS Revised Bright Galaxy sample with a significance level of $p \sim 0.05$ ($\sim 2\sigma$). The starbursts were selected for their high infra-red flux at 100 microns: $S_{100\mu m} > 250\,\mathrm{Jy}$ and two of them: M82 and NGC 253 have been observed by high energy γ-ray telescopes. In the following chapter we examine the methodology and results of the study and make an extension of it using more realistic statistical methods and updated neutrino data sets. We also examine the sensitivity of the results to the cut placed on the infra-red flux of starburst galaxies.

5.1 Summary of the study

Here we provide a brief summary of the methodology, data selection and results of the study performed by Lunardini et al. in order to provide context for our later examination of it.

5.1.1 Data Selection

For their study Lunadrini et al. used the three year HESE sample containing thirty seven events measured in the first 988 days of the detector's operation. However two events were found to be in coincidence with IceTop, implying they were atmospheric in origin and are therefore excluded. Of the remaining thirty five events, ten of them are track events with small angular uncertainties $\sigma < 1^\circ$ and the remainder are cascade events with large angular uncertainties $\sigma \sim 15^\circ$. It is interesting to note that none of the correlations found involved track events.

Source Catalogues

Lunadrini et al. considered three classes of galaxies as neutrino sources:

1. Blazars

2. Seyfert II Galaxies

3. Star-forming regions and starburst galaxies

with each examined independently of the others. They consider objects that have been observed to emit high energy γ-rays as this may indicate pion production. The γ-ray fluxes of these objects can also provide a crude upper limit on the possible neutrino flux, although they note that γ-ray absorption may reduce the γ-ray flux with respect to the neutrino flux and lead to an under estimation of the upper limit. A cut on the photon-flux of the Blazars and Seyferts is used to leave only the brightest sources which are more likely to be observed by IceCube. The catalogues used in the study include the following,

- TeVCat: A compilation of known high energy γ-ray sources ($100\,\mathrm{GeV} < E_\gamma < 100\,\mathrm{TeV}$) measured by HESS, MAGIC and VERITAS. These observatories measure Cherenkov light from γ-ray initiated air-showers allowing good angular resolution reconstruction $\sigma < 0.1°$.

- 3FGL: A catalogue of extra-galactic objects measured by the Fermi-LAT detector on the Fermi satellite over 4 years. Fermi-LAT measures γ-ray photons over an energy range of: $100\,\mathrm{MeV} < E_\gamma < 100\,\mathrm{GeV}$. Angular resolution ranges from 5° at 100 MeV to 0.8° at 1 GeV. Gamma-ray emission near the galactic plane ($|b| < 10°$) is likely produced by galactic cosmic rays [14] and is therefore excluded.

- IRAS Revised Bright Galaxy Catalogue: Star-formation is measured using emission in the far infra-red at 100μm as a proxy. Starburst galaxies comprise the objects with the highest fluxes and are selected by using a cut on the flux density at 60 μm ($S_{60\mu\mathrm{m}} > 5.24\,\mathrm{Jy}$). Objects within 5° of the galactic plane are also excluded ($|b| < 5°$).

5.1.2 Method

The authors use equatorial coordinates in their analysis, a convention that we also follow in all following chapters. For the set of neutrino events and sources from a given catalogue, we estimate the coincident rate, defined as when the coordinates of the i^{th} event and j^{th} source are aligned within the median angular uncertainties σ_i and σ_j. The angular distance S_{ij} is defined:

$$S_{ij} = \Delta\theta_{ij} = \cos^{-1}(\sin\delta_i \sin\delta_j + \cos\delta_i \cos\delta_j \cos\Delta\alpha_{ij}) \tag{5.1}$$

where δ_i and δ_j are the declinations of event i and source j respectively and $\Delta\alpha_{ij} = \alpha_i - \alpha_j$. From S_{ij} which we define the unit-less "weighted distance" R_{ij} using the median angular uncertainties:

$$R_{ij} = \frac{S_{ij}}{\sqrt{\sigma_i^2 + \sigma_j^2}} \tag{5.2}$$

and since we expect $\sigma_i \gg \sigma_j$ in all instances [57] we simplify this term to $R_{ij} = S_{ij}/\sigma_i$. For each event we calculate the weighted distance to the nearest source r_i where $r_i = R_{ij_{min}}$ is smaller than the distance to all other sources.

$$r_i = min(R_{ij})\,(r_i = R_{ij_{min}} < R_{ij}, \forall j) \tag{5.3}$$

For a set of neutrino events and sources, we find the distribution of r, and calculate the coincidence rate N_C to be the number of events for which $r < 1$. Note that we have dropped the index i on r for the sake of simplicity. We find our null distribution by sampling a set of events of equal size from a background and finding the r distribution for each. For a truly isotropic background we can find the r distribution analytically [24].

$$\frac{dP(r)}{dr} = \sum_{i}^{N_\nu} \sigma_i \frac{N_{\rm src}}{2^{N_{\rm src}}} \sin\sigma_i [1 + \cos r\sigma_i]^{N_{\rm src}-1} \tag{5.4}$$

Alternatively one can estimate the result's significance by scrambling the positions of either the sources or the neutrinos and recalculating the coincidence rate. After repeating this process a large number of times, one can calculate the probability of the finding the observed coincidence rate by chance. The authors chose to scramble the positions of the sources and leave fixed the positions of the neutrinos. N_C is the relevant parameter in the analysis, and we define the significance using the probability p of finding N_C in the null distribution that is equal to or greater than that of the experimental results:

$$p = \frac{\sum_i^{N_{\rm skies}} N_{C,i} \geq N_{C,\rm obs}}{N_{\rm skies}} \tag{5.5}$$

Since many cascade events overlap with other cascade events, we could treat them as originating from the same source. Therefore it may be useful to treat overlapping events as belonging to a common source, and then measure a coincidence rate between the combined events with the catalogue objects. The events are merged through an iterative process with each of the $N!$ possible pairs considered. For the $\rm i^{th}$ event if the distance to the closest event j is $R_{ij} < 1$ then a new combined event is created with the coordinates,

$$\alpha_c = \frac{\sum_i^2 \alpha_i \cdot \sigma_i^{-2}}{\sum_i^2 \sigma_i^{-2}} \quad \delta_c = \frac{\sum_i^2 \delta_i \cdot \sigma_i^{-2}}{\sum_i^2 \sigma_i^{-2}} \quad \sigma_c^2 = \sum_i^2 \sigma_i^2 \tag{5.6}$$

and the process is then repeated until $R_{ij} > 1$ for all remaining events. Note that interpreting these combined events as actual sources can lead to implied sources with implausibly high fluxes and should only be taken as a cross-check on the cross correlations found for the event and source lists.

5.1.3 Results

The coincident rate N_C, the excess from the null distribution ΔN_C ($= N_{C,\rm exp} - N_{C,\rm null}$) and its significance are found by comparing the r-distribution from the real events and the ensemble of randomized events (see figures 5.1, 5.2, 5.3 and 5.4). In general the null distributions feature a narrowly peaked curve reaching its maximum around $r \sim 2$ and then falling sharply up to $r = 10$. The null distributions also contain a long tail with a slight bulge for $r > 10$ that is inconsistent with the the peaked curve for $r < 10$. These two components of the distribution correspond to the cascades in case of the peak and tracks in the case of the tail. This can be explained since the tracks have smaller angular resolutions and are thus likely to be further away from a given source than a cascade. It is notable that both features of the null distribution can also be seen with experimental r-distributions, since only cascades were found to overlap with sources. Additionally sky-maps are displayed alongside the r-distributions in figures 5.1, 5.2, 5.3 and 5.4. In the figures the median angular resolution illustrated with a red error circle and the size of the marker proportional to the energy. The examined sources are shown with colourized markers.

Blazars (AGN)

For the analysis of blazars, the authors draw their sources from the 3FGL catalogue, where objects are already identified by their type [65] and place a cut on the photon flux $\Phi_\gamma \geq 10^{-9}\,\rm cm^{-2}s^{-1}$ in the energy band $10\,\rm GeV < E_\gamma < 100\,\rm GeV$. The cuts leave eleven objects as potential sources including ten blazars and one flat spectrum radio quasar (FSQR). The results are consistent with

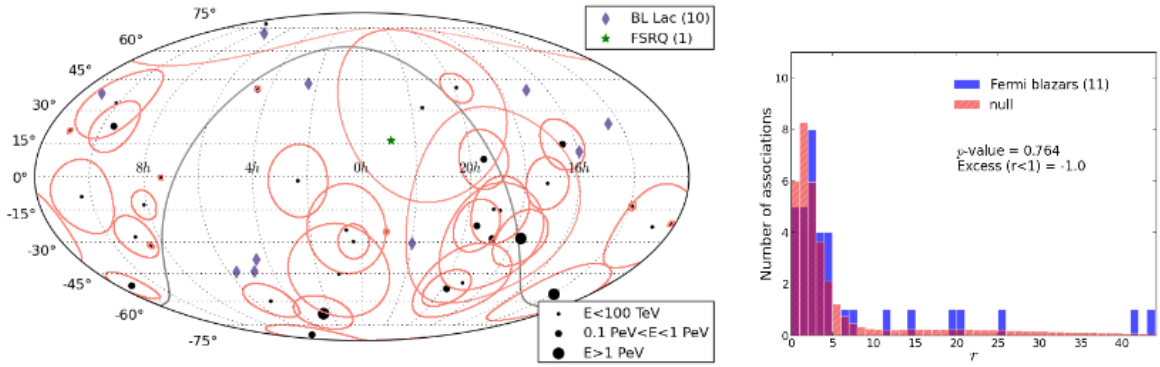

Figure 5.1: The sky-map and (left) r-distribution (right) of bright Fermi blazars examined by Emig et al [24]. Neutrino events are indicated with black markers whose size is proportional to the event energy (see legend). The angular uncertainty is indicated with a red circle centred on one of the dots. Source positions are shown with colourized markers (see legend). The plot on the right shows the null r-distribution (pink) against the measured r-distribution (blue) with overlaps shown in dark pink.

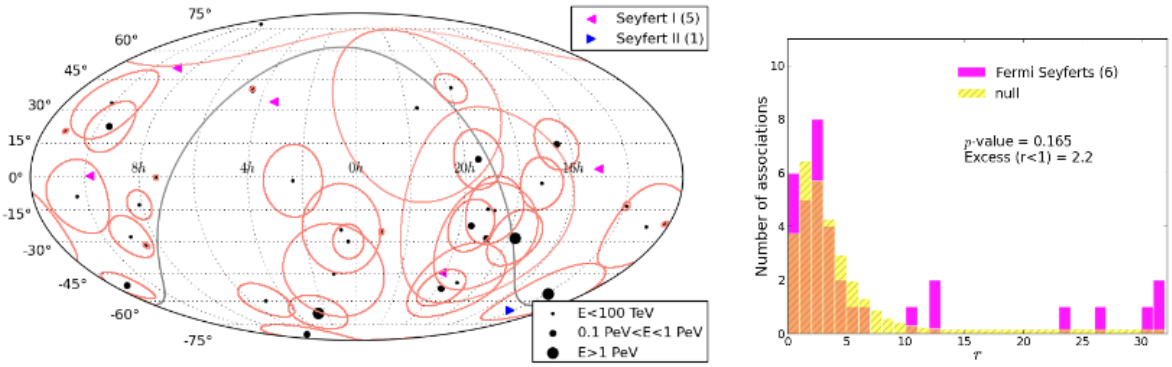

Figure 5.2: The skymap (left) and r-distributions (right) of bright Fermi Seyferts examined by Emig et al [24]. The angular uncertainty of the event is indicated with red circles (as per figure 5.1 and the event and source positions with markers (see legend). The null r-distribution is shown in yellow, the experimental distribution in violet and the overlap in orange (see legend).

the null hypothesis (figure 5.1) [24] with 6 events coincident with a blazar, below that expected from the null hypothesis $\Delta N_C = -1$ with a p-value of $p = 0.764$.

Seyferts

All six Seyfert II galaxies identified in the 3FGL catalogue are used in the analysis. In this case six events are coincident with Seyferts, a small excess from that expected from the null distribution $\Delta N_C = 2.2$ with a p-value of $p = 0.165$ (figure 5.2). No correlation is claimed but that authors note that the result may merit further investigation into Seyfert galaxies.

Starbursts

The authors consider the brightest seven starburst galaxies in the IRAS RBG catalogue with a cut imposed on the 100-micron flux density $S_{100\mu m} > 250\,\text{Jy}$ to select for high star-formation in addition to the cut on the 60-micron flux density $S_{60\mu m} > 5.24\,\text{Jy}$ to remove Seyfert galaxies. Two of these, M82 and NGC 253, are included in the TeVCat catalogue. Another two galaxies are included in the 3FGL catalogue but are not observed in the TeV range. The remaining three

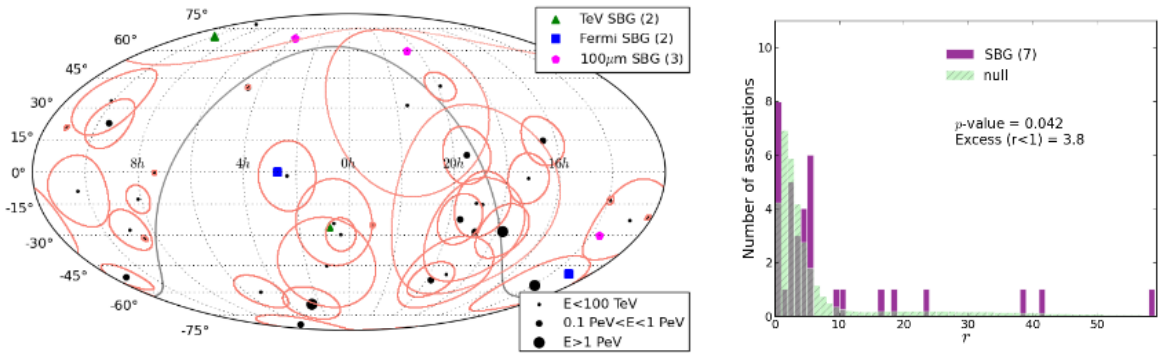

Figure 5.3: Emig et al's sky-map and r-distribution for the brightest 7 starburst galaxies in the IRAS catalogue [24]. The red error circles indicate the event's angular uncertainty (as per figures 5.1 and 5.2) and event and source positions with the black and colour markers respectively (see legend). The experimental r-distribution is shown in purple and the null distribution in green (see legend).

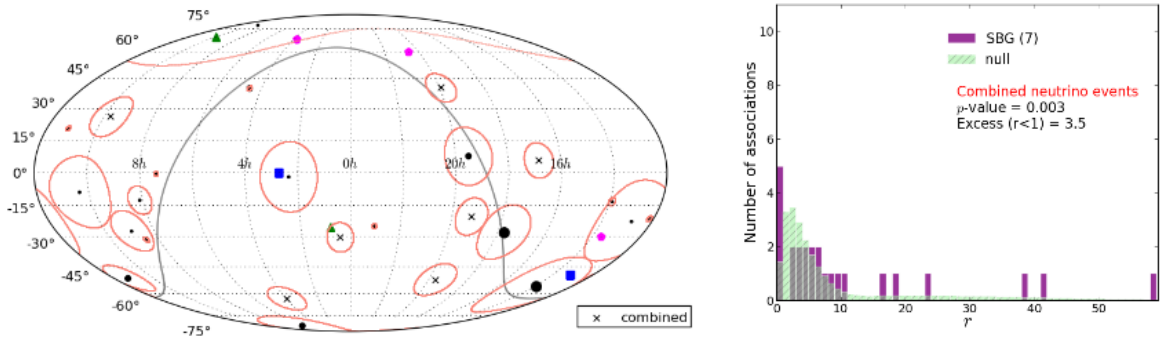

Figure 5.4: The same test as figure 5.4 applied with merged overlapping events, to test the robustness of the correlation [24].

have no observed γ-ray emission but pass the infra-red flux cut. All seven starburst galaxies are coincident with cascade events, with one coincident with two events resulting in a coincident rate of $N_C = 8$, an excess of $N_C = 3.8$ from the null hypothesis (figure 5.3). This corresponds to a p-value of $p = 0.042$, meaning that 4.2 % of the ensemble equals or exceeds the experimental coincidence rate. This correlation was somewhat strengthened when overlapping events were iteratively merged, leaving a list of twenty five events. The coincidence rate was lower $N_C = 5$, but was more significant ($p = 0.003$) as fewer overlaps are expected for the null distribution $\Delta N_C = 3.5$ (see figures 5.3 and 5.4).

Starbursts and star-forming regions

The results for starburst galaxies were taken as evidence for a star-formation driven model of neutrino production. Finally the authors consider nearby star-formation regions that are not starburst galaxies. Since nearby star-forming regions such as the Magellanic clouds are brighter in infra-red and γ-ray radiation than the examined starburst galaxies they could also be brighter neutrino sources under a star-formation driven model. A new catalogue of nearby star-forming regions was created including the four γ-ray starbursts as well as the Magellenic clouds and the Cocoon nebula is Cygnus (IC 5146), designated as star-forming regions in the 3FGL catalogue [13]. The cross correlation results are a coincidence rate of ten events, exceeding the null distribution by $\Delta N_C = 5.8$ at significance level of $p = 0.003$ (figure 5.5), a noticeable increase in significance from the starburst-only catalogue.

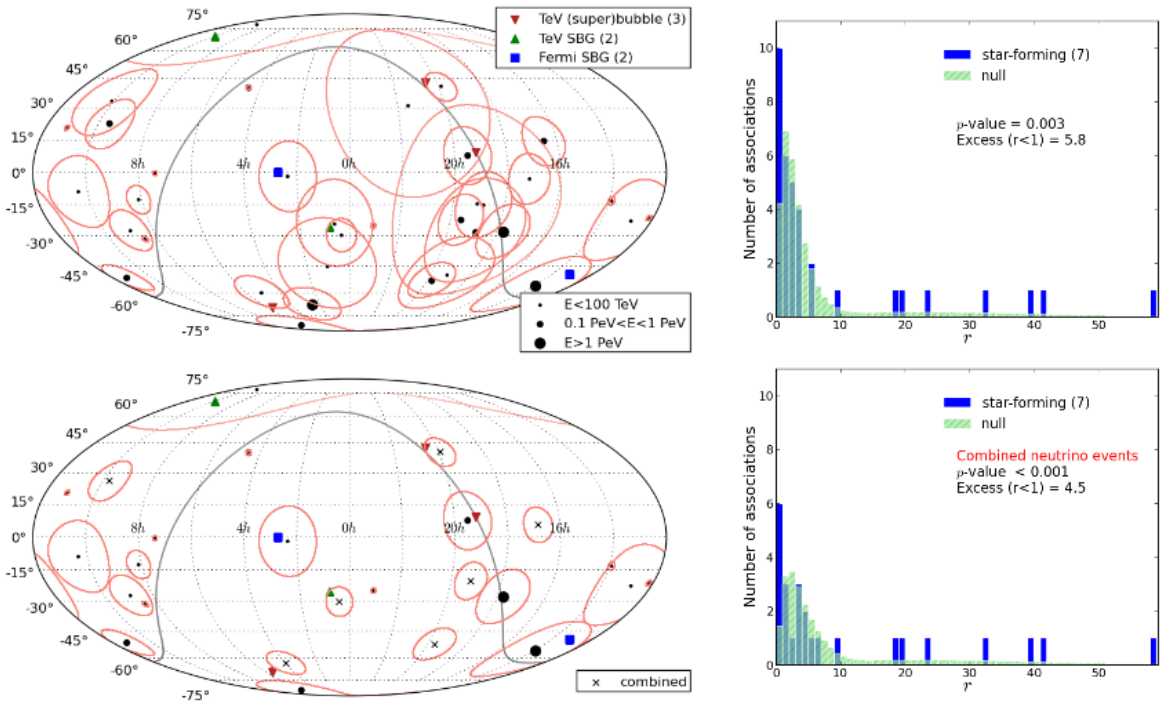

Figure 5.5: Skymap (left) and r-distribution (right) of star-forming regions and observed neutrino events (top) and for combined events (bottom).

5.2 Review

Having summarized the paper, we now examine the author's results when the analysis is repeated with an additional year of data from IceCube. We investigated the sensitivity of the results to the cuts on the source flux, seeing if the choice of the cut affects the significance of the correlation. Finally the significance was estimated using scrambling of the neutrinos while keeping the sources fixed, in addition to the method used in [24].

5.2.1 Increased Data

The four year High Energy Starting Event sample adds an additional seventeen events to the three year sample, including six additional tracks, leaving a total of fifty two events with thirteen tracks. Compared with the list of bright starburst galaxies, an additional coincidence was found for starburst galaxy M83. All of the examined events and sources are displayed in figure 5.6 with the error circles indicating the angular uncertainty of the event. The total coincidence rate was $N_C = 9$, in excess of $\Delta N_C = 3.86$ from the null distribution found from scrambling the source coordinates (see figure 5.7(a)).

5.2.2 Weighted Background Sampling

An alternative method of estimating the r distribution under the null-hypothesis is to scramble the positions of the events while holding the sources fixed. This approach is more complicated as a truly isotropic distribution of astrophysical neutrinos will be subject to differing absorption when arriving at different zenith angles and at different energies [9] (see figures 5.10 and 5.11 to see the E-sin δ distribution for tracks and cascades respectively). The Earth becomes more opaque to neutrinos at higher energies, resulting in a lower acceptance from the northern sky. Hence the event declination is sampled from the simulated declination distribution of neutrino events (the distribution is shown in figure 5.9). The right ascension is sampled from a flat distribution

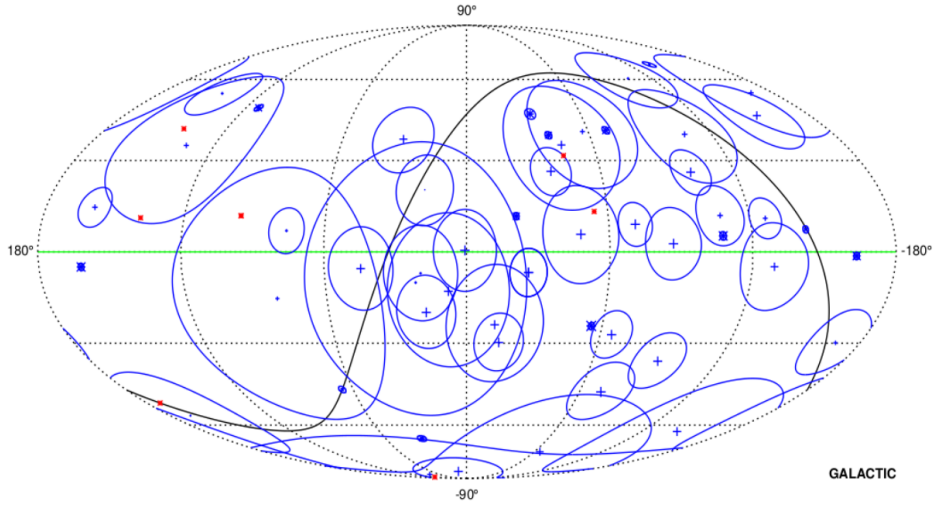

Figure 5.6: 4 year HESE events (blue) and 7 bright starbursts (red). Median angular uncertainty of events shown with error circle (blue). "Plus" markers show the best fit position of cascades and "X" markers denote tracks. Size of marker scales with energy. The sky-map is shown in galactic coordinates, equatorial plane shown in black.

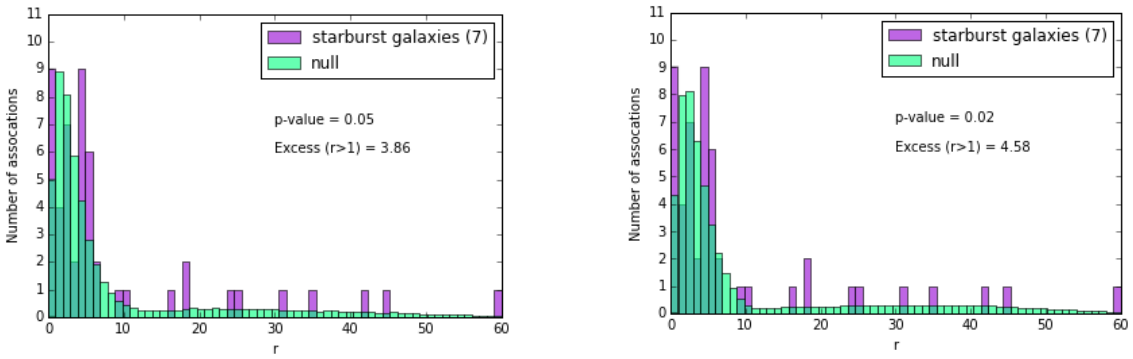

(a) (b)

Figure 5.7: The r-distribution for 4 year starting events and bright starbursts. (a) displays the results for scrambling the sources and fixing the events while (b) shows them for scrambled events and fixed sources. The latter approach results in a lower p-value, but the effect is minor.

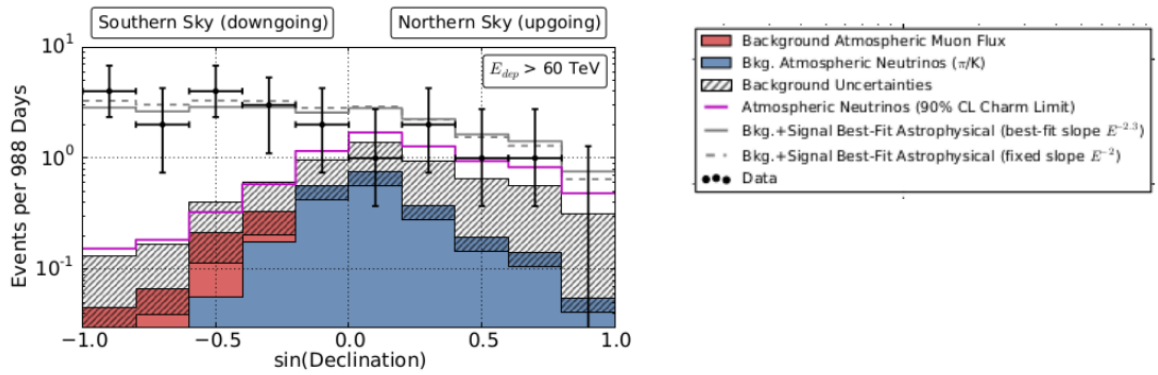

Figure 5.8: sin(δ) distribution across zenith angle for 3 year starting events [9].

$S_{100\mu\mathrm{m},cut}$[Jy]	N_{gal}	N_C	ΔN_C	p
250	7	8	4.44	0.02
200	9	10	4.7	0.04
150	9	10	4.7	0.07
100	26	15	5.02	0.08
50	42	20	7.06	0.02
0	127	24	4.35	0.16

Table 5.1: The change in correlation significances for successively lower infra-red cuts

as we can assume azimuthal symmetry for the detector (as its positioned at the South Pole). We calculated the r-distribution and hence the ΔN_C value, with the results displayed in figure 5.7b. The effect on the analysis is small, we find a slightly greater significance $p = 0.02$ for event scrambling than we find for source scrambling $p = 0.05$ using the four year HESE sample and the seven bright starburst galaxies (see figure 5.7a).

5.2.3 Infrared Cut

The cut at $S_{100\mu\mathrm{m}} > 250\,\mathrm{Jy}$ limits the source catalogue to only seven objects [24], a list smaller than the number of neutrinos being checked for correlation. This largely avoids the problem of having multiple sources explaining the same event (although this does happen in the cases of galaxies M82 and NGC 1068, both overlapping with the same event), causing a break down of the method. At some point, as the size of the source catalogue increases, a coincidence with an event becomes inevitable for a given source and this method is unable to measure significant correlations. This threshold was explored by lowering the cut on the flux $S_{100\mu\mathrm{m}}$ with the results displayed in table 5.1. A similar proportion of galaxies overlap with events as the cut is lowered, with significance not varying much until the cut is removed entirely. It is apparent the choice of the cut does not have much influence on the significance of the results but the presence of any cut does affect the results (see figure 5.12).

5.3 Summary

A weak correlation ($\sim 2\sigma$) between bright starburst galaxies in the IRAS RBG sample and the IceCube HESE four year sample is found. The strength of the correlation appears to be consistent when tested using different methods of estimating the null distribution and using different cuts on the source fluxes. Although the correlation is not highly significant, further investigation may be merited with track events from larger data sets (i.e. the up-going muon sample).

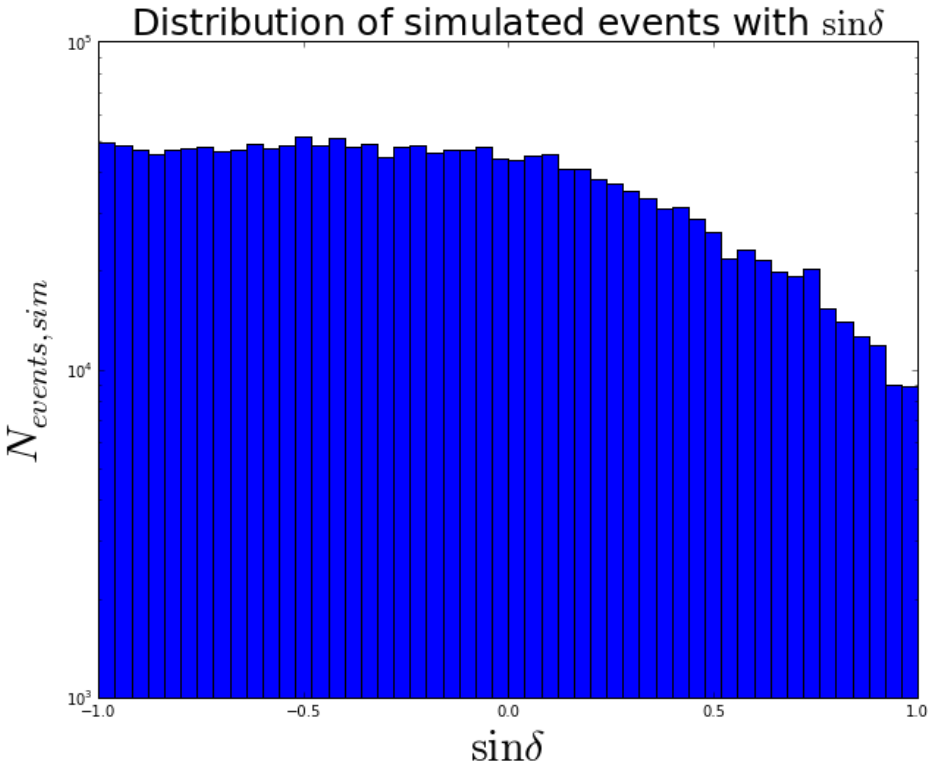

Figure 5.9: Simulation of the HESE event distribution across $\sin\delta$. The distribution decreases north of the celestial equator due to the reduced detector sensitivity. A total of 2×10^6 simulated events are displayed in the histogram.

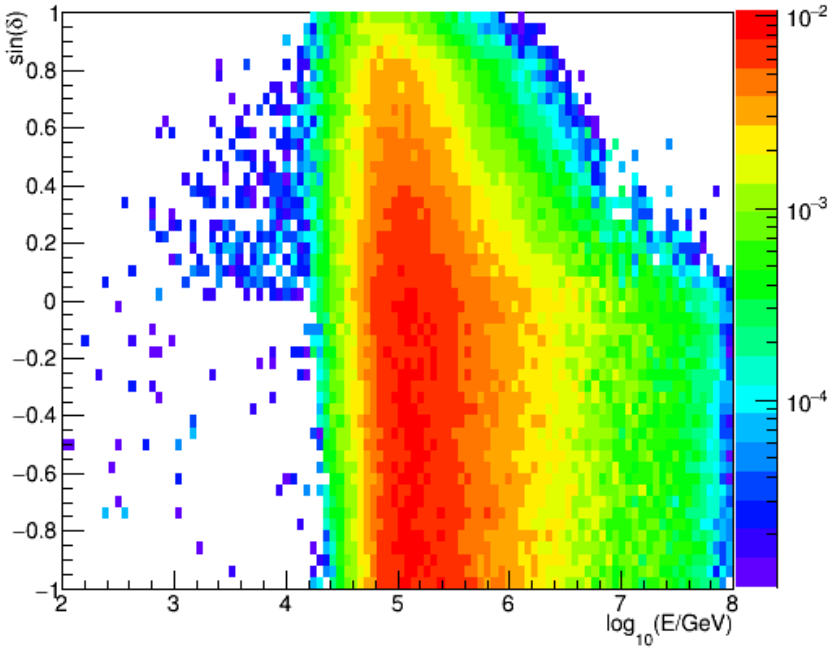

Figure 5.10: The astrophysical background distribution of in-detector track events, plotted over $\log_{10}(E/GeV)$ and $\sin(\delta)$. The color scale indicates the event frequency per bin of $\log_{10}(E/GeV)$ and $\sin(\delta)$. For the latter a standard power law $\Phi_{\text{ast}}(E) \propto E^{-2}$ is assumed.

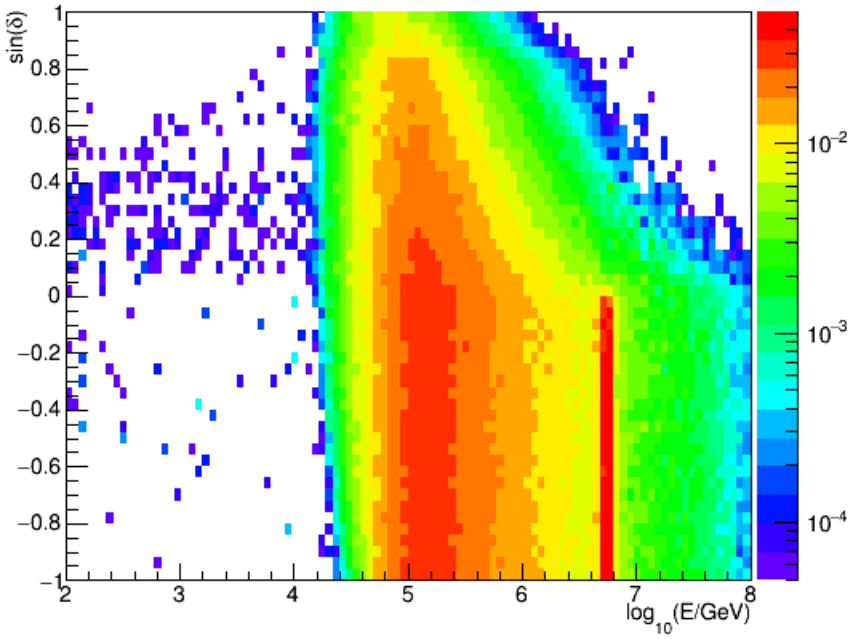

Figure 5.11: The astrophysical backgrounds for cascade events. The colour scale indicates the frequency of events per bin. Note the strong peak at $\log(E/\mathrm{GeV}) \sim 6.8$ corresponding to the Glashow resonance [19] [33]: enhanced production of W bosons from anti-neutrino interactions $\bar{\nu}_e + e^- \to W^-$ at $E = 6.3\,\mathrm{PeV}$.

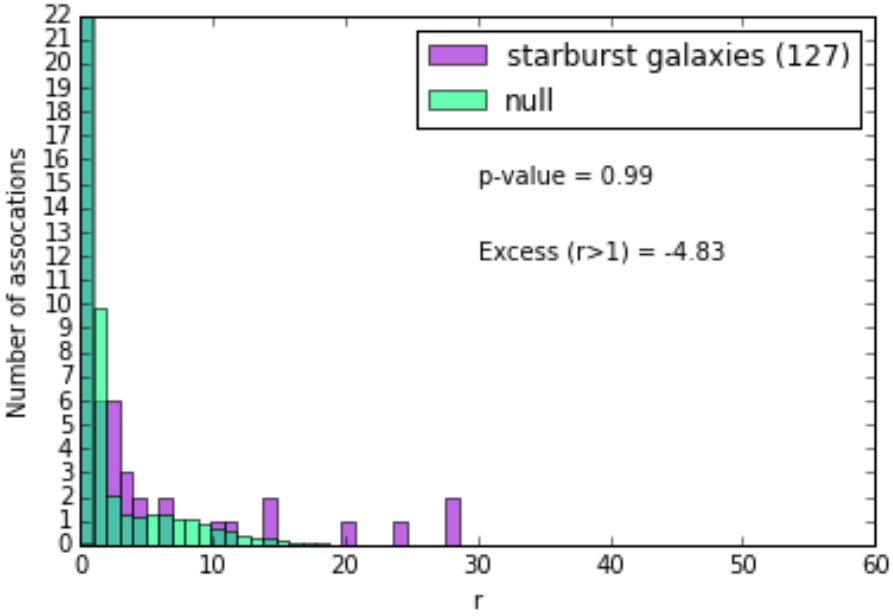

Figure 5.12: The r-distribution for the uncut starburst sample (127 galaxies in total). The null distribution is found from neutrino scrambling. The null distribution far exceeds the experimental distribution in the bin of $r < 1$ ($\Delta N_C = -4.83$), indicating no significant correlation can be claimed when the full list of sources is analysed.

Chapter 6

A Star-formation Driven Model of Cosmic Neutrino Emission

The cumulative emission from cosmic ray interactions in star-forming galaxies (SFGs) has been proposed as the dominant component of the astrophysical neutrino flux measured by IceCube at TeV to PeV scale energies[88] [89]. The same cosmic ray interactions will inevitably lead to γ-ray emission from the same sources. GeV γ-ray emission has been observed in several SFGs by Fermi-LAT[14] and collectively produces around 61^{+30}_{-18} % of the extragalactic γ-ray intensity above 1 GeV [59]. A well supported correlation between bolometric far infra-red emission ($8\,\mu\text{m} < \lambda < 1000\,\mu\text{m}$) and γ-ray emission ($0.1\text{GeV} < E_\gamma < 100\text{GeV}$) in SFGs [14] [59] supports a connection between star-formation and γ-ray emission. This may also indicate neutrino and cosmic ray production in SFGs. However leptonic production mechanisms are considered equally likely to explain γ-ray emission in SFGs [67]. Moreover, the astrophysical neutrino flux is best constrained between 10 TeV to 1 PeV, at least two orders of magnitude above the maximum photon energy ($\sim$ 100 GeV) measured by Fermi-LAT. Thus predicting neutrino intensities at IceCube scale energies requires an extrapolation of the spectral index at these energies. Indeed only two SFGs, the starburst galaxies M82 and NGC 253, have been observed at TeV photon energies [47]. The lack of TeV observations from SFGs may be explained by attenuation by the dense gas clouds and radiation fields present in star-forming regions [47][57].

In lieu of high energy γ-ray observations, we use the IR-γ scaling relation to predict the collective neutrino emission from SFGs and starburst galaxies, using the star-formation rate evolution function [61] to predict the density of SFGs over cosmic time. We assume maximal hadronic contribution to the γ-ray intensities and plot the predicted neutrino intensity over possible starburst spectral indices Γ_{SB}. We find that SFGs and starbursts would need to have hard spectral indices close to $\Gamma \sim 2$ to explain the intensity observed by IceCube. However the combined analysis of IceCube data predicts a spectral index of around $\Gamma_\nu \sim 2.5 \pm 0.1$ at TeV energies, with which star-forming galaxies would under-predict the flux by at least an order of magnitude[17]. Observations of M82 and NGC 253 also disfavour hard spectral indices for starburst galaxies. However, hard spectral indices are within the uncertainty range of the up-going muon analysis, leaving open the possibility of a multiple origin scenario for the neutrino flux [6]. We also examine the collective neutrino emission from local starburst galaxies in the IRAS Bright Galaxy catalogue, in the context of a point source analysis discussed in chapter 9.

6.1 Flux versus Intensity

Here we clarify the meanings of flux and intensity as they often used interchangeably in astrophysics. In the following chapters we use the definitions of flux and intensity used by Rybicki and Lightman in *Radiative Processes in Astrophysics*[76]. Classically a flux is the measurement

of all energy carried by all rays passing through a given area. However in particle astrophysics we consider the number of particles passing through a unit area per unit time. Specific intensity is defined as the number of particles dN from a specific direction $\hat{\Omega}$ passing through a unit area dA per unit time dt in an energy interval dE and within an unit solid angle $d\Omega$ about the arrival direction. Usually the particles are arriving isotropically from the sky (except at the very highest energies) so the directional dependence is usually dropped.

$$I(E, \hat{\Omega}) = \frac{dN}{dAdtdEd\Omega} \tag{6.1}$$

Particle flux is simply the number of particles passing through an area across the entire sky, i.e. the intensity integrated over all solid angles. Unfortunately flux is often used to refer to intensity in the literature of particle astrophysics. We adopt the following definition of differential particle flux:

$$\frac{d\Phi}{dE} = \int I(E) d\cos(\theta) d\Omega \tag{6.2}$$

Since the energy spectrum of particles usually obeys an inverse power law with a spectral index $\Gamma \sim 2$ we obtain the differential energy flux by multiplying the term by the energy squared:

$$E^2 \frac{d\Phi}{dE} [\mathrm{GeV cm^{-2} s^{-1} sr^{-1}}] \tag{6.3}$$

Hence the strength of neutrino emission is quantified using the value of the differential energy flux (defined in equation 6.3). Note that the different energy flux is constant per log-energy interval for an E^{-2} spectrum.

6.2 Estimating Starburst Neutrino Emission

The collective astrophysical neutrino flux can be resolved into the sum of emission from all neutrino sources in the observable Universe. Each neutrino source has an intrinsic luminosity L_ν and distance from Earth. To account for the effects of cosmological red-shift and time dilation we use the luminosity distance $D_L = (1+z)^2 D_C$, which is defined using the co-moving distance D_C. Thus we represent the neutrino flux from star-forming galaxies as a sum:

$$\Phi_{\nu,SB} = \sum_i^N \Phi_{\nu,i} = \sum_i^N \frac{L_{\nu,i}}{4\pi D_{L,i}^2} \tag{6.4}$$

with N total starburst galaxies in the observable Universe. The flux received at Earth originates from sources distributed across cosmic red-shift. The distribution of the flux per interval of red-shift depends on the evolution of source density and luminosity. We assume that the average luminosity per source (starburst or normal star-forming galaxy) remains constant over time and we account for the change in source distributions with a co-moving density $n_{SB}(z)$ of star-forming galaxies. We then define an integral:

$$\Phi_{\nu,SB} = \lim_{N\to\infty} \sum_i^N \frac{L_{\nu,i}}{4\pi D_i^2} = \hat{L}_\nu \int_0^{z_{max}} \frac{n_{SB}(z)}{4\pi D_L^2(z)} \frac{dV_C(z)}{dz} dz = \hat{L}_\nu \int_0^{z_{max}} \frac{n_{SB}(z)}{4\pi (1+z)^2 D_C^2(z)} \frac{dV_C(z)}{dz} dz \tag{6.5}$$

with our number density integrated over the co-moving volume $V_C(z) = 4\pi D_C^3/3$. By taking the differential of co-moving volume over red-shift we find the expression for differential co-moving volume:

$$\frac{dV_C(z)}{dz} = 4\pi D_C^2(z) \frac{dD_C(z)}{dz} \tag{6.6}$$

with co-moving distance defined using the Hubble distance $D_H = c/H_0$ and the Hubble parameter $H(z) = H_0 E(z)$. H_0 is the Hubble constant for the present epoch. Thus the co-moving distance becomes:

$$D_C(z) = \int_0^z \frac{D_H}{E(z')} dz' = \int_0^z \frac{c}{H(z')} dz' = \int_0^z \frac{c}{H_0 E(z')} dz' \tag{6.7}$$

we then differentiate the co-moving distance to find:

$$\frac{dD_C(z)}{dz} = \frac{c}{H_0 E(z)} \tag{6.8}$$

and define $E(z)$:

$$E(z) = \sqrt{\Omega_r (1+z)^4 + \Omega_m (1+z)^3 + \Omega_k (1+z)^2 + \Omega_\Lambda} \tag{6.9}$$

using the total matter density Ω_m (including dark matter and baryonic matter), radiation density Ω_r and the cosmological constant Ω_Λ (or dark energy density). The curvature term $\Omega_k = 1 - \Omega_m - \Omega_\Lambda$ is exactly zero for a flat Universe (the curvature most consistent with current observations) and the radiation density can be considered negligible and ignored. Thus we simplify the parameter to:

$$E(z) = \sqrt{\Omega_m (1+z)^3 + \Omega_\Lambda} \tag{6.10}$$

and by feeding these terms into our original integral (6.5) we estimate the collective neutrino flux to be:

$$\Phi_{\nu,SB} = \hat{L}_\nu \int_0^{z_{max}} \frac{n_{SB}(z)}{4\pi(1+z)^2 D_C^2(z)} \frac{4\pi D_C^2(z) c}{H_0 E(z)} dz = \frac{c\hat{L}_\nu}{H_0} \int_0^{z_{max}} \frac{n_{SB}(z)}{(1+z)^2 E(z)} dz \tag{6.11}$$

for all SFGs out to z_{max}. For our analysis we set $z_{max} = 5$, considering all SFGs from 1.2 Gyr after the Big Bang (all SFGs within a 7.9 Gpc radius from the Earth), the end of the cosmic dark ages [61]. For our cosmological parameters we use the 2015 results from the Planck satellite: $\Omega_\Lambda = 0.68$, $\Omega_m = 0.32$ and $H_0 = 68\,\mathrm{kms}^{-1}\mathrm{Mpc}^{-1}$ [72].

6.2.1 Starburst densities

The most extensive all-sky catalogue of starburst galaxies, the IRAS Revised Bright Galaxy Catalogue (IRAS RBGS), extends to a maximum red-shift of $z = 0.03$ corresponding to a maximum distance of $D \sim 200\,\mathrm{Mpc}$ (see figure 6.1). The number density of star-forming galaxies across cosmological time up to $z_{max} \sim 5$ can be estimated from the evolution of the cosmic star-formation rate. The density of the star-formation rate across red-shift, $\Psi(z)$, is described well by the function 6.12 which is found by applying a fit to infra-red and ultra-violet emission associated with star-formation[61].

$$\Psi(z) = 0.015 \frac{(1+z)^{2.7}}{1 + [(1+z)/2.9]^{5.6}} \,[\mathrm{M}_\odot \mathrm{yr}^{-1} \mathrm{Mpc}^{-3}] \tag{6.12}$$

The fraction of stellar material formed in starbursts f_{SB} has varied over time from 5 % for low red-shift ($z < 1$), to 20 % during the peak of star-formation ($1 < z < 2$) to 10 % preceding that ($z > 2$). We define a starburst galaxy as a star-forming galaxy with a local star-formation rate $\Psi_0 \geq 10\,\mathrm{M}_\odot/\mathrm{yr}$. Combining these factors we obtain the co-moving starburst number density $n_{SB}(z)$:

$$n_{SB}(z) = \frac{\Psi(z) f_{SB}}{\Psi_0} \,[\mathrm{Mpc}^{-3}] \tag{6.13}$$

The cosmic star-formation rate evolution is shown in figure 6.2. Incorporating equation 6.13

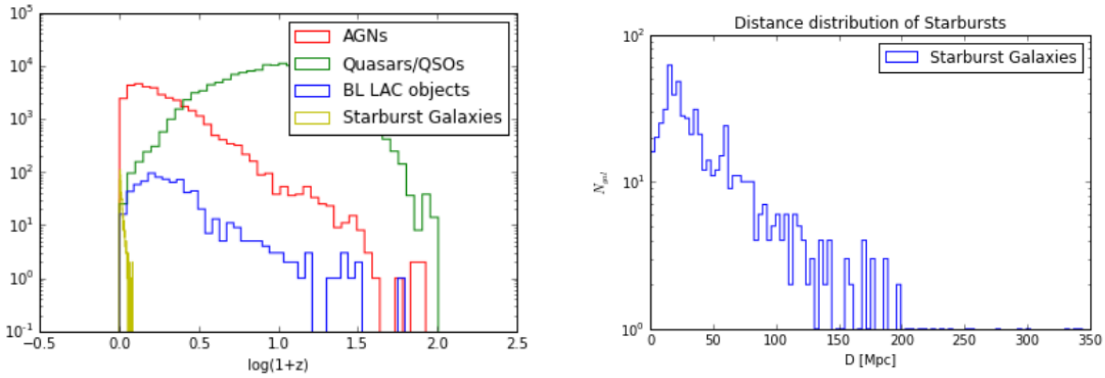

Figure 6.1: Figure 6.1(a)) shows the distribution of different classes of galaxies across redshift $\log(1+z)$. The active galaxy types: AGN, Quasars and BL Lac objects are drawn from the Veron-Cetty and Veron catalgoue [85] while the starburst galaxies are drawn from the IRAS catalgoue [78]. Figure 6.1(b) shows distances to the IRAS starburst galaxies.

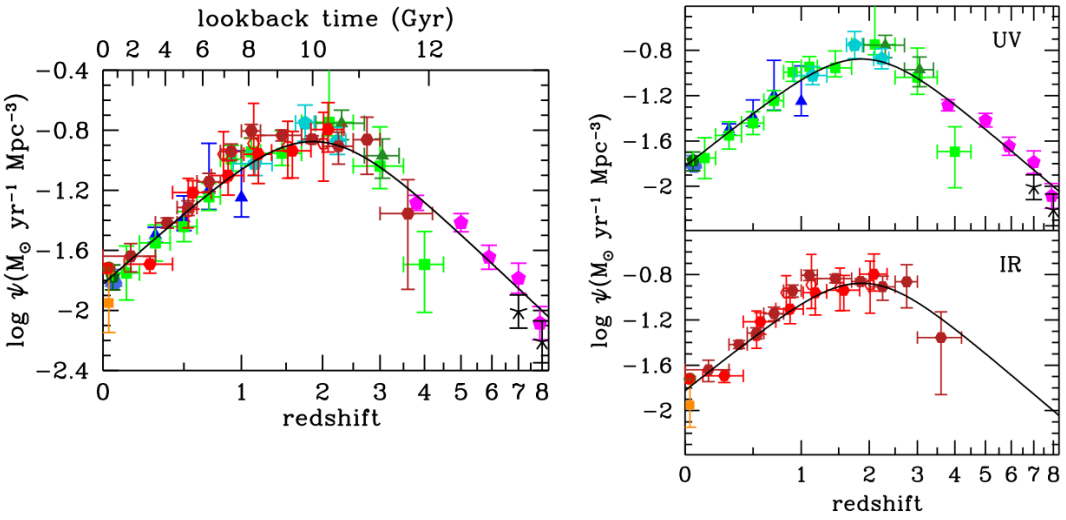

Figure 6.2: Star-formation rate density across redshift [$M_\odot yr^{-1}Mpc^{-3}$], fitted to UV and IR data [61].

into 6.11 we obtain the integral formula for the starburst neutrino flux.

$$\Phi_{\nu,SB} = \frac{c\hat{L}_\nu}{H_0\Psi_0}\int_0^{z_{max}} \frac{\Psi(z)f_{SB}(z)}{(1+z)^2E(z)}dz \tag{6.14}$$

6.2.2 Starburst Neutrino Luminosity

To estimate L_ν we utilize the IR-γ-ray relation (see figure 6.3) to calculate the bolometric γ-ray luminosity between 100 MeV and 100 GeV. We assume an entirely hadronic origin and assume that the neutrino luminosity is equal within the same energy range.

$$\log_{10}(L_\nu/\text{ergs}^{-1}) \sim \log_{10}(L_\gamma/\text{ergs}^{-1}) = \alpha\log_{10}(L_{\text{IR}}/10^{10}\text{L}_\odot) + \beta \tag{6.15}$$

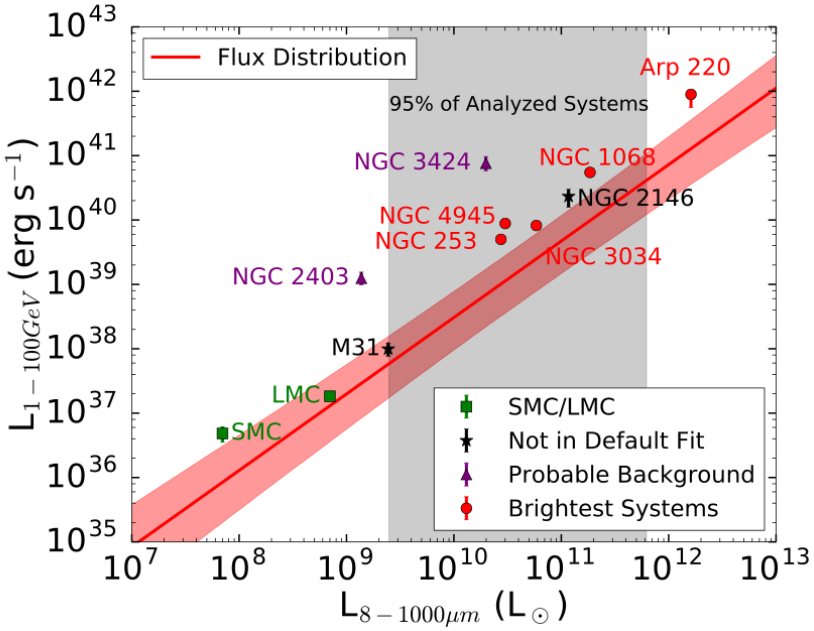

Figure 6.3: The correlation between the bolometric infra-red luminosity $L_{8-1000\mu\mathrm{m}}$ and γ-ray luminosity $L_{0.1-100\mathrm{GeV}}$ in star-forming galaxies[17].

From the bolometric neutrino luminosity we find the integral energy flux between 100 MeV to 100 GeV:

$$\Phi_{\nu,0.1-100\mathrm{GeV}} = \int_{100\mathrm{MeV}}^{100\mathrm{GeV}} E\frac{d\Phi_\nu(E)}{dE}dE = \frac{c}{H_0\Psi_0}\int_0^{z_{max}} \frac{\Psi(z)f_{SB}(z)L_{\nu,0.1-100\mathrm{GeV}}(z)}{(1+z)^2E(z)}dz \quad (6.16)$$

and since we expect the intrinsic neutrino luminosity per starburst to remain constant over time we remove luminosity from the integral:

$$\int_{100\mathrm{MeV}}^{100\mathrm{GeV}} E\frac{d\Phi_\nu(E)}{dE}dE = \frac{c\hat{L}_{\nu,0.1-100\mathrm{GeV}}}{H_0\Psi_0}\int_0^{z_{max}} \frac{\Psi(z)f_{SB}(z)}{(1+z)^2E(z)}dz \quad (6.17)$$

where $\hat{L}_{\nu,0.1-100\mathrm{GeV}}$ is the average neutrino luminosity between 100 MeV and 100 GeV for a starburst galaxy. We find this average value for luminosity from the distribution of luminosities $f(L)$ for a sample of starburst galaxies, the IRAS revised bright catalogue (see figure 6.4).

$$\hat{L} = \frac{\int_{L_{min}}^{L_{max}} Lf(L)dL}{\int_{L_{min}}^{L_{max}} f(L)dL} \quad (6.18)$$

We solve the formula 6.17 to find the differential flux assuming the value of the spectral index Γ.

$$\frac{d\Phi_\nu(E)}{dE} = \Phi_0 E^{-\Gamma} \quad (6.19)$$

Hence by combining the IR-γ relation (equation 6.15) and the starburst number density we estimate total neutrino flux associated with starburst galaxies. The results are summarized in the following section (section 6.2.3).

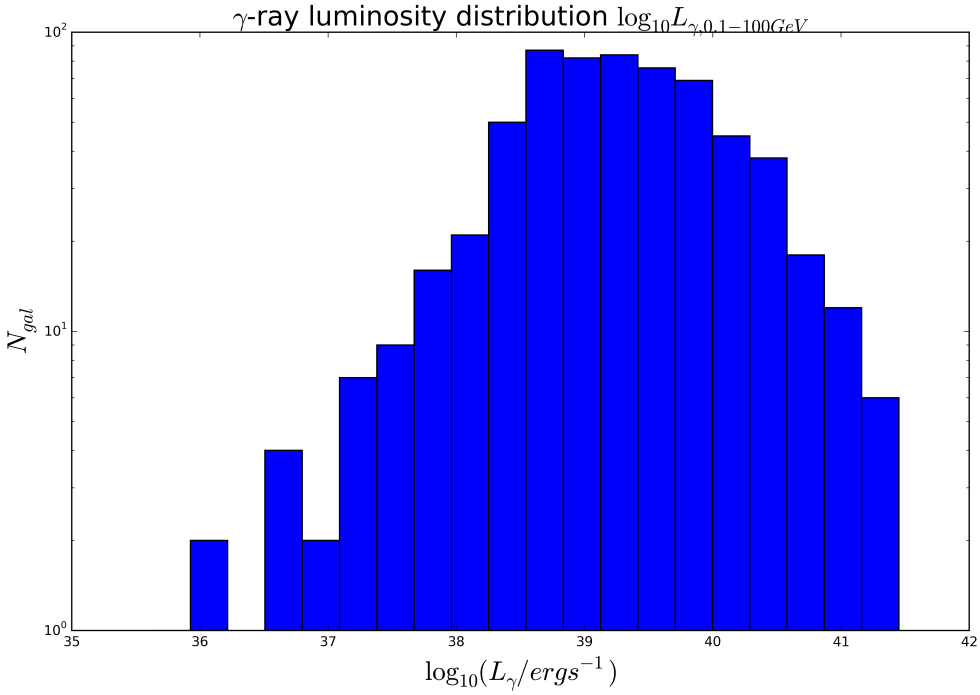

Figure 6.4: Distribution of bolometric γ-ray luminosities L_γ for starburst galaxies in the IRAS bright galaxy catalogue. The luminosities of the starbursts are inferred from the scaling relation (figure 6.15). Assuming $\nu/\gamma \sim 1$ we find an average neutrino luminosity of $L_\nu = 1.74 \times 10^{39}\,\mathrm{ergs}^{-1}$ a similar value to that assumed for starburst galaxies in figure 4.4 in chapter 4 [64].

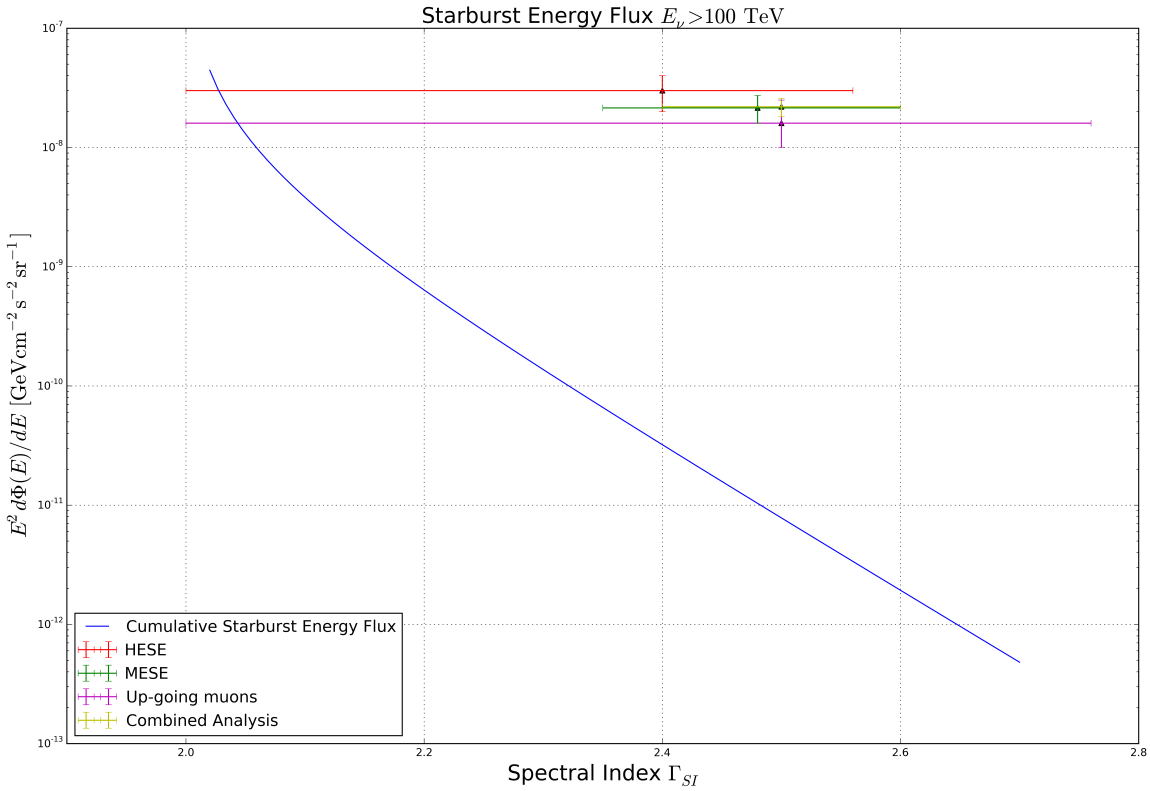

Figure 6.5: The cumulative starburst energy flux at 100 TeV for a range of spectral indices Γ between 2 and 2.8. Also displayed for comparison are the measured astrophysical flux normalizations and spectral indices, with their 95% intervals from the HESE [9], MESE [10] and up-going muon sample [6] (see chapter 3 for an explanation of these samples). Additionally the results of the combined analysis is shown. The predicted starburst energy flux underpredicts the flux measured by IceCube for most spectral indices, except perhaps for the up-going muon sample.

6.2.3 Results

Under a spectral index assumption of $\Gamma = 2$ the energy flux remains constant as a function of energy (implying that an exponential cut-off must exist at some energy). We plot the expected values of the total starburst energy flux with different spectral indices ranging from $\Gamma = 2$ to $\Gamma = 2.8$ in figure 6.5. The distribution with spectral index is compared with the measured values of the neutrino flux found in the HESE, MESE and up-going muon analysis. For $\Phi_{\nu,C}(100\text{TeV})$ of the combined analysis [43] we find the fraction of neutrino emission produced by starburst galaxies falls rapidly for larger spectral indices with $\Phi_{SB}/\Phi_{\nu,C} \sim 1$ at $\Gamma = 2$ falling to $\Phi_{SB}/\Phi_{\nu,C} \sim 0.1$ at $\Gamma = 2.2$ and $\Phi_{SB}/\Phi_{\nu,C} \sim 0.01$ at $\Gamma = 2.4$.

We obtained our estimates for the starburst energy flux by solving the integral formula 6.17. However the integrand of 6.17 gives the differential starburst energy flux as a function of red-shift. Figure 6.6 indicates the distribution of the flux origin with red-shift, with the shape indicating that only a small fraction (< 0.1) of neutrino production occurs in the local Universe ($D < 200\,\text{Mpc}$) under our model. To illustrate this we take the luminosities of the starburst

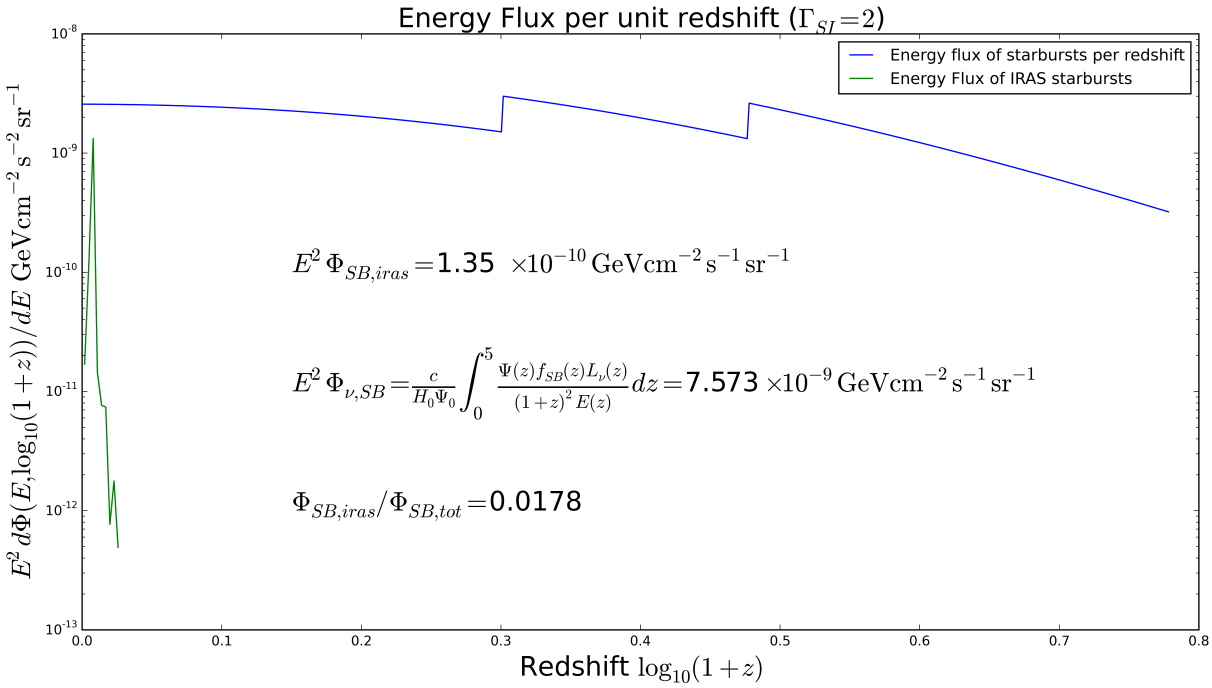

Figure 6.6: The predicted neutrino intensity of star-forming galaxies, distributed over the log of the red-shift ($\log(1+z)$) of the star-forming galaxies. The blue curve shows the flux distribution obtained from the evolution of the star-formation rate, while the green curve shows the neutrino intensity of the galaxies in the IRAS bright galaxy catalogue.

galaxies in the IRAS catalogue (see figure 6.4) and find the collective flux using the equation 6.4.

$$\Phi_{\nu,iras} = \sum_{i}^{N_{\rm IRAS}} \Phi_{\nu,i} = \sum_{i}^{N_{iras}} \frac{L_{\nu,i}}{4\pi D_i^2} \tag{6.20}$$

Under an assumption of $\Gamma = 2$ we find a collective neutrino emission $E^2 d\Phi_{\nu,iras}/dE = 1.35 \times 10^{-10}\,\mathrm{GeVcm^{-2}s^{-1}sr^{-1}}$, around 1.78 % of the value expected found from the integral expression 6.17. Figure 6.6 shows the distribution of the IRAS flux over red-shift, which follows from the predictions of our model at higher red-shifts. We would expect the completeness of the catalogue to fall with greater red-shift.

6.3 Summary

By combining the IR-γ scaling relation and a model of starburst number densities over red-shift we find that starbursts may account for the majority of the neutrino flux assuming very hard spectral indices $\Gamma \sim 2$. We also find that the majority of this emission would originate at distant red-shifts $z > 1$, produced in sources that are unlikely to be distinguished as point sources. However hard spectral indices are currently disfavoured by most IceCube diffuse analyses (HESE, MESE and the combined analysis shown in figure 6.5) which imply $\Gamma \sim 2.4$ although a spectral index of $\Gamma = 2$ is not excluded in the analysis of the up-going muon sample. Furthermore, although most starburst galaxies do not have measurable TeV γ-ray emission, observations by HESS and VERITAS of M82 and NGC 253 (the two nearest starburst galaxies) imply softer spectral indices closer to $\Gamma \sim 2.2$ [47]. For these reasons it is possible but unlikely that starburst

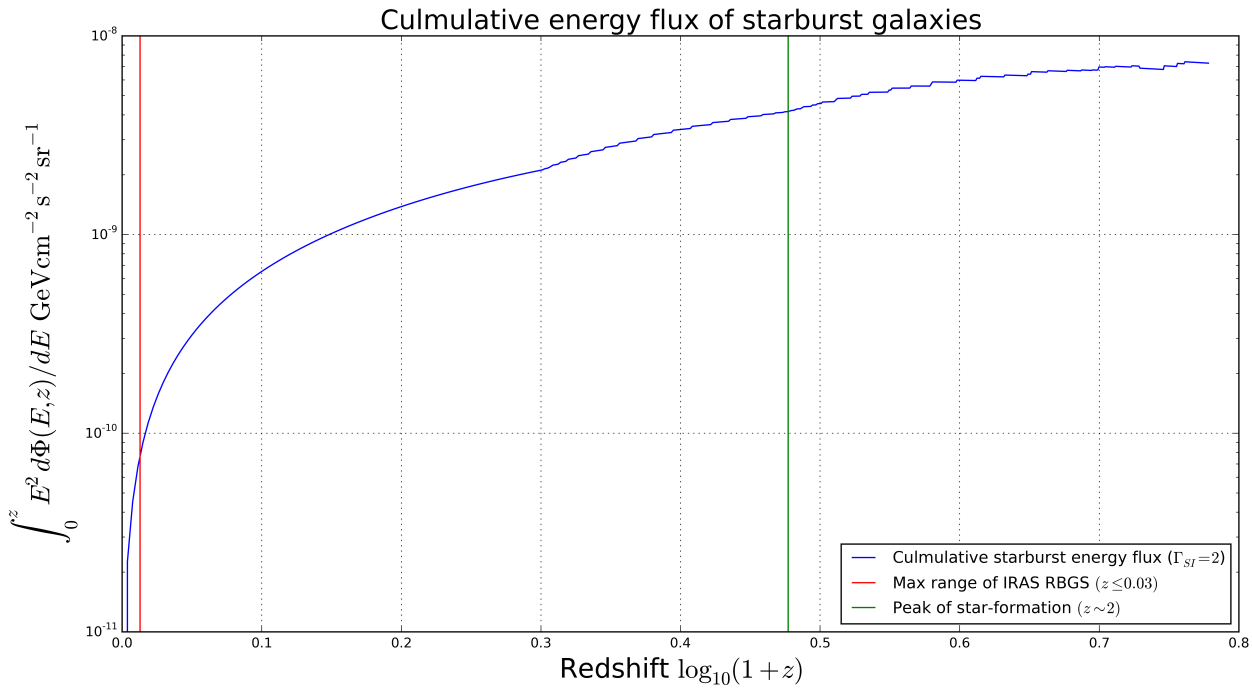

Figure 6.7: The cumulative neutrino flux of starburst galaxies up to redshift z ($E^2 d\Phi_{C,\nu}(E,z)/dE = \int_0^z E^2 d\Phi_\nu(z^{'})/dE/dz^{'}\, dz^{'}$). Over the range of the IRAS Revised Bright Galaxy Sample ($z \leq 0.03$), containing the starbursts used in this analysis, the cumulative flux adds up to $\sim 2\%$ of the total expected from starbursts under our model. The majority of the energy flux is emitted during the peak of the star-formation $z \sim 2$. This result implies that the bulk of starburst neutrino emission originates in distant sources that likely cannot be resolved with point source searches.

galaxies form the majority of the astrophysical neutrino flux, a conclusion in agreement with a similar analysis of starburst neutrino emission[17]. Under very optimistic assumptions of the spectral index and the hadronic origins of the starburst γ-ray flux, a stacked point source analysis would need to be sensitive to a collective point source emission of 1 to 2 % of the total astrophysical flux. The sensitivity of a stacked point source analysis of starburst galaxies is the subject of chapter 9 and of this thesis in general.

Chapter 7

Point Source Methods

In chapter 9 we search for a neutrino signal from starburst galaxies in the IRAS revised bright galaxy catalogue. We search for the signal using a stacked point source likelihood function. The point source likelihood considers the background components of the neutrino flux as well as a possible signal component, the latter of which is quantified with the best fit value to the number of signal events n_s, the value of which is found by optimizing the likelihood function:

$$\ln \mathcal{L}(n_s) = \sum_{i}^{N} \ln[\frac{n_s}{N} S_i + \frac{N_A - n_s}{N} A_i + \frac{n_c}{N} C_i] \tag{7.1}$$

in which N is the total number of neutrino events, N_A is the number of astrophysical events, S_i is the signal probability for event i, while A_i and C_i are the astrophysical and atmospheric background probabilities respectively. A full derivation of equation 7.1 is outlined in the following chapter.

7.1 Maximum Likelihood Analysis

Point source searches utilize optimization of a statistical likelihood function to determine the most optimal set of parameters that explain the observed data. This usually includes the number of "signal events" (events that originate from point sources) n_s and the spectral index Γ of the point source flux. The terms likelihood and probability are used interchangeably in everyday parlance, but in statistics the terms have related but distinct definitions. Both terms describe the relationship between a set of data $\vec{x}$ and a model that can be described with a set of parameters θ. We can describe the probability distribution of a set of data for fixed parameters θ_0 with a density function $P(\vec{x}, \theta_0)$. This is useful for predicting the outcome of a physical model before performing the experiment and obtaining the data. However for a fixed set of data we use a *likelihood* function $\mathcal{L}(\theta, \vec{x}_0)$ to find the parameters most likely to predict the data. In our case we wish to distinguish a subset of neutrinos originating from point sources, our signal, from a diffuse background which may account for the majority of events in a given event sample. The likelihood is found from the product of the linear combinations of the signal and background densities per event:

$$\mathcal{L}(\theta, \vec{x}) = \mathcal{L}(n_s, \vec{x}) = \prod_{i=1}^{N} [\frac{n_s}{N} S(x_i) + (1 - \frac{n_s}{N}) B(x_i)] \tag{7.2}$$

where there are N events and $S(x_i)$ and $B(x_i)$ are the values of the signal and background probability densities for the event features: energy, declination, right ascension and flavour $x_i = (E_i, \delta_i, \alpha_i, f_i)$.

7.2 Derivation of the Likelihood Function

The measurement of a neutrino with a particular energy and flavour from some region of the sky is a discrete event which obeys a Poisson probability distribution. The unbinned likelihood function is derived from the Poisson probability for a sky divided amongst discrete regions or pixels.

$$\mathcal{L} = \prod_{i=1}^{N_{bins}} \frac{\lambda_i^{n_i} e^{-\lambda_i}}{n_i!} \tag{7.3}$$

The symbol λ_i is the rate per bin of observing an event in the i^{th} pixel and n_i is the number of events observed. Taking the log of the likelihood we get:

$$\ln \mathcal{L} = \sum_{i=1}^{N_{bins}} n_i \ln \lambda_i - \lambda_i - \ln n_i! \tag{7.4}$$

and as we take the limit of N_{bins} to infinity, n_i becomes either 0 or 1 in each bin. Hence the likelihood function takes two modes:

- If $n_i = 0$, then the contribution for index i to $\ln \mathcal{L}$ is: $-\lambda_i$
- Otherwise if $n_i = 1$, then the contribution for index i to $\ln \mathcal{L}$ is: $\ln \lambda_i - \lambda_i$

Next, we can define a new index j, running from 1 to N_{obs} events to create two components to the likelihood function evaluation.

$$\ln \mathcal{L} = \sum_{j}^{N_{obs}} \ln \lambda_j - \sum_{i}^{N_{bins}} \lambda_i \tag{7.5}$$

We define $\lambda_{tot} = \sum_{i}^{N_{bins}} \lambda_i$, leading to:

$$\ln \mathcal{L} = \sum_{i}^{N_{bins}} \ln \lambda_i - \lambda_{tot} \tag{7.6}$$

Hence we obtain a signal likelihood defined in terms of the event rate per bin.

7.2.1 Application to Unbinned Point Source Analyses

We take the unbinned limit of the Poisson likelihood to derive our point source likelihood function. If λ_i is the rate of observing event i, then λ_{tot} is the total event rate across the entire parameter space: energy, flavour and arrival direction. One can create a model that predicts the event rate for a given set of parameters, describing the event rate distribution with some function $\Lambda_j(x_i, E_i, f_i)$. This function has a dependence on the event arrival direction x_i, energy E_i, flavour f_i and sky pixel j. We use this value for the given event parameters to weight the event point spread function ρ_{ij} to find the event rate:

$$\lambda_i = \sum_{j}^{N_{pix}} \rho_{ij} \Lambda_j(x_i, E_i, f_i) \tag{7.7}$$

For the point source analysis discussed in chapter 9, only track events are considered so event flavour can be neglected as a parameter. For an IceCube point source analysis, where the detector is situated at the South Pole, one can calculate the background rate of events simply by

scrambling the real data in azimuth ϕ or right-ascension α (as $\alpha \equiv \phi$ in this case). Alternatively we can derive the event rate from simulations, allowing us to deconvolve the distribution into different components. The latter is the approach used by the IceCube diffuse analysis and some point source analyses, including the one discussed in this thesis.

7.2.2 Expected event rate distributions

We incorporate models of event energy, arrival direction and flavour distributions from astrophysical and atmospheric origins into our analysis. The astrophysical flux is further divided into *diffuse* and *point-source* components. Diffuse in this case may be something of a misnomer as in this context "diffuse" refers to the observational status of the data rather than the true origin of the events. If we are unable presently to resolve any point sources in astrophysical samples, we may still consider that the events originate in point-like objects (i.e. AGN or starburst galaxies) instead of a truly diffuse origin (e.g. neutrino production tracing the gas in the galactic halo). Additionally, the atmospheric flux is deconvolved into *conventional* and *prompt* fluxes. "Conventional" and "prompt" refer to different hadronic production mechanisms. Conventional atmospheric neutrinos are generated by pion and kaon species in air-showers whilst prompt atmospheric neutrinos are generated by heavier meson species containing charm quarks. The prompt hadron component of the shower decays faster than the lighter species, changing the observed energy and flavour spectrum seen in the detector.

The event rate distribution $\Lambda_j(x_i, E_i, f_i)$ can be found to be the linear combination of the different components of the flux, as shown in equation 7.8.

$$\begin{aligned}\Lambda_j(x_i, E_i, f_i) = n_s\Phi_{\text{ptsrc}}(x_s, x_i, E_i, f_i)_j + n_a\Phi_{\text{astro}}(x_i, E_i, f_i)_j \\ + n_c\Phi_{\text{conv}}(x_i, E_i, f_i)_j + n_p\Phi_{\text{prompt}}(x_i, E_i, f_i)_j\end{aligned} \tag{7.8}$$

The different Φ symbols denote the normalized event distribution across the (x_i, E_i, f_i) parameter space. The diffuse, conventional and prompt components have non-zero values across the sky while the point source component is non-zero only at the point-source location in the binned case. All components add to the flux and hence cannot subtract from the total event rate. The point source rate predicts events only at a single pixel denoted by the point source location x_s, thus we express the point source flux Φ_{ptsrc} as $\Phi_{\text{ptsrc}}(x_s, x_i, E_i, f_i)$.

7.2.3 Total Event Rate

The fits from our model must predict the total number of events across the sky for our sample, from each component to the flux,

$$\lambda_{tot} = n_s \sum \Phi_{\text{ptsrc}} + n_a \sum \Phi_{\text{astro}} + n_c \sum \Phi_{\text{conv}} + n_p \sum \Phi_{\text{prompt}} \tag{7.9}$$

and, since all our distributions are normalized we find:

$$\lambda_{tot} = n_s + n_a + n_c + n_p \tag{7.10}$$

Having N events means that we can fit λ such that $N = \lambda$.

7.2.4 Simplifying the Likelihood Function

Incorporating equations (7.8) and (7.7) into (7.4) we obtain the result:

$$\begin{aligned}\ln\mathcal{L} = \sum_i^{N_{bins}} \ln[\sum_j^{N_{pix}} n_s\rho_{ij}\Phi_{\text{ptsrc}}(x_s, x_i, E_i, f_i)_j + n_a\rho_{ij}\Phi_{\text{astro}}(x_i, E_i, f_i)_j \\ + n_c\rho_{ij}\phi_{\text{conv}}(x_i, E_i, f_i)_j + n_p\rho_{ij}\Phi_{\text{prompt}}(x_i, E_i, f_i)_j] - [n_s + n_a + n_c + n_p]\end{aligned} \tag{7.11}$$

To simplify this equation, we define new terms S_i, A_i, C_i and P_i as shorthand, accounting for both the parameter distributions and event PSFs:

$$\sum_{j}^{N_{pix}} \rho_{ij}\Phi_{\text{ptsrc}}(x_s, x_i, E_i, f_i)_j = S(x_s, x_i, E_i, f_i) = S_i(x_s) \tag{7.12}$$

$$\sum_{j}^{N_{pix}} \rho_{ij}\Phi_{\text{astro}}(x_i, E_i, f_i)_j = A(x_i, E_i, f_i) = A_i \tag{7.13}$$

$$\sum_{j}^{N_{pix}} \rho_{ij}\Phi_{\text{conv}}(x_i, E_i, f_i)_j = C(x_i, E_i, f_i) = C_i \tag{7.14}$$

$$\sum_{j}^{N_{pix}} \rho_{ij}\Phi_{\text{prompt}}(x_i, E_i, f_i)_j = P(x_i, E_i, f_i) = P_i \tag{7.15}$$

By substituting the far-right terms into 7.11 we obtain:

$$\ln \mathcal{L} = \sum_{i}^{N_{bins}} [\ln(n_s S_i + n_a A_i + n_c C_i + n_p P_i)] - [n_s + n_a + n_c + n_p] \tag{7.16}$$

we can further reduce the likelihood function by taking: $N = N_\nu = \lambda_{tot} = n_s + n_a + n_c + n_p$, and with some further rearranging:

$$\ln \mathcal{L} = \sum_{i}^{N} [\ln(\frac{n_s}{N} S_i + \frac{n_a}{N} A_i + \frac{n_c}{N} C_i + \frac{n_p}{N} P_i)] + N \ln N - N \tag{7.17}$$

since $N \ln N - N$ is a constant term it can be ignored. We can also define reasonable constraints such as the total observed event number as the sum of : $N = n_s + n_a + n_c + n_p$ and specifying that the proportion of astrophysical events be constant as the sum of the point source and astrophysical components, $N_{ast} = n_a + n_s$. Additionally for the diffuse up-going analysis, it can be assumed that there is no prompt component[4]. Hence we obtain our equation of a single point source likelihood:

$$\ln \mathcal{L}(n_s, x_{src}) = \sum_{i}^{N_{obs}} [\ln(\frac{n_s}{N} S_i + \frac{N_{ast} - n_s}{N} A_i + \frac{n_c}{N} C_i)] \tag{7.18}$$

One can obtain the most likely location and signal strength of a point source in the data by optimizing equation 7.18. However if we wish to find most likely signal strength from the locations of a predefined set of sources we use a *stacked* likelihood function. We previously defined the signal PDF as $S_i = S(x_s, x_i, E_i, f_i)$. However we can also define the signal PDF as a linear combination of individual signal PDFs defined using a set of source positions obtained from some catalogue $\vec{x}_{s,cat} = (x_{s,1}, x_{s,2}, ...)$:

$$S(\vec{x}_{s,cat}, x_i, E_i, f_i) = \sum_{j}^{N_{src}} S(x_{s,j}, x_i, E_i, f_i) \tag{7.19}$$

The number of sources in the tested catalogue is defined with the symbol N_{src}. Since the single source signal PDF is defined with a point spread function we can define the multi-source signal

PDF as the sum of point spread functions:

$$S(\vec{x}_{s,cat}, x_i, E_i, f_i) = \sum_j^{N_{src}} \rho_j(x_{s,j}, x_i) g(E_i, f_i) \tag{7.20}$$

The other effects on the signal probability, which are dependent on energy and flavour are described with $g(E_i, f_i)$. Note that in equation 7.20 the source PDFs are weighted equally and as such there is an equal probability of measuring an event across the sources. To account for situations where some sources are brighter, and hence more likely to produce neutrino events, we introduce source weight w_j

$$S(\vec{x}_{s,cat}, x_i, E_i, f_i) = \sum_j^{N_{src}} \frac{w_j}{\sum w_j} \rho_j(x_{s,j}, x_i) g(E_i, f_i) = \sum_j^{N_{src}} \bar{w}_j \rho_j(x_{s,j}, x_i) g(E_i, f_i) \tag{7.21}$$

The term $\bar{w}_j$ is the relative weight per source. The weight of the source may be dependent on the characteristics of the source, such as its flux normalization Φ_j and spectral index Γ_j. Additionally we can also use weight to account for different detector acceptances across the sky. As such we can define the source weight such that $w_j = w(x_{s,j}, \Phi_j, \Gamma_j)$. Hence we obtain:

$$S_i = S(\vec{x}_{s,cat}, x_i, E_i, f_i) = \sum_j^{N_{src}} \bar{w}_j(x_{s,j}, \Phi_j, \Gamma_j) \rho_j(x_{s,j}, x_i) g(E_i, f_i) \tag{7.22}$$

Thus, with a change of definition of the signal PDF, equation 7.18 is valid likelihood function for a single source likelihood and a multiple source stacked-likelihood.

$$\ln \mathcal{L}(n_s) = \sum_i^{N_{obs}} [\ln(\frac{n_s}{N} S_i(\vec{x}_{s,cat}) + \frac{N_{ast} - n_s}{N} A_i + \frac{n_c}{N} C_i)] \tag{7.23}$$

7.3 Summary

From the Poisson likelihood for observing an event in a discrete region of the sky we were able to derive the un-binned stacked likelihood function of observing a point source under a signal hypothesis specified with the signal PDF. We showed that the likelihood function can be generalized from a single point source into a observing a signal from a catalogue of point sources.

Chapter 8

Event and Sky Simulations

The simulation of "signal-like" neutrino skies is crucial for testing the sensitivity of an analysis to a point source component of the neutrino flux. To that end we developed a software program that simulated the composition of neutrino data, sampling from known background distributions and a signal distribution that reflects the examined hypothesis. The signal component should manifest as the clustering of neutrino events around the positions of point sources.

We utilise simulations of the three year up-going diffuse sample with an 86 string configuration (IC-86). The effects on the sample neutrino population from Earth absorption, detector acceptance, reconstruction and data cuts to develop the sample are folded into the simulation. The three year up-going muon-neutrino sample (see chapter 3) contains $N \gtrsim 10^5$ events, the majority of which are atmospheric events while a smaller proportion are astrophysical events, out of which some proportion may originate from point sources while the rest are "diffuse" in origin. As mentioned in chapter 7 the term "diffuse" is an observational designation, the diffuse events may well originate from point-like sources that are too weak or distant to be resolved in the point source analysis. "Diffuse" should not be taken to imply that the neutrinos are produced by diffuse objects such as the local galactic halo. The proportions of atmospheric, diffuse and signal astrophysical events are controlled by the parameters: the number of conventional atmospheric event N_C, diffuse astrophysical events $N_{A,\text{diff}}$ and astrophysical signal events n_s, in which $N = N_C + N_A$ and $N_A = n_s + N_{A,\text{diff}}$.

Given probability densities of the conventional and astrophysical backgrounds $C(E, \sin\delta)$ and $A(E, \sin\delta)$ and the signal $S(E, \alpha, \delta, \sigma, \Gamma)$ we can generate simulations of the up-going neutrino sample that reflect the signal flux we wish to test for. The parameters of the PDFs are energy, positions and, for the signal, the spectral index of the sources and the angular resolution of the events. We hence sample n_s events from the signal PDF $S(E, \alpha, \delta, \sigma, \Gamma)$, $N_{A,\text{diff}}$ from the diffuse astrophysical PDF $A(E, \sin\delta)$ and N_C from the atmospheric PDF $C(E, \sin\delta)$ to produce a list of N total events. The procedure for doing so is outlined in this chapter.

8.1 Background Event Generation

The relevant phase space of observables for our events are in the reconstructed muon energy E and in the arrival declination δ. Given the detector's position at the south pole we can assume azimuthal symmetry and ignore right ascension α. Many analyses use local detector coordinates: zenith angle θ and azimuth ϕ. However in this analysis, with its astronomical focus, we will use the equatorial coordinates more common in astronomy.

The simulation is weighted by the probability of the event being from the conventional or diffuse astrophysical background and filled into a two-dimensional ROOT histogram (see figures 8.1 and

8.2).

- 100 bins in the log of energy: $2 < \log_{10}(E/\text{GeV}) < 8$.
- 60 bins in the sine of declination: $-1 < \sin\delta < 1$.

The histograms are defined using the logarithm of the energy across 6 decades, from 10^2 GeV to 10^8 GeV (or 100 PeV). Note that the highest energy neutrino events so far measured are only in the PeV range. The sine of declination forms the other histogram dimension, from $\sin\delta = 1$ (the north celestial pole) to $\sin\delta = -1$ (the south celestial pole). In this case only up-going events are considered with $\delta \geq -5°$. The number of total astrophysical events N_A and conventional atmospheric events N_C are set *a priori*. Accordingly N_C and $N_{A,\text{diff}}$ events are generated with $\log_{10}(E/\text{GeV})$ and $\sin\delta$ sampled from the respective histograms using the TRandom class in ROOT (see figures 8.1 and 8.2). The right ascension values are simply random numbers between 0 and 2π in radians. An additional histogram containing the event resolutions from the real data is used to generate the angular uncertainty per event.

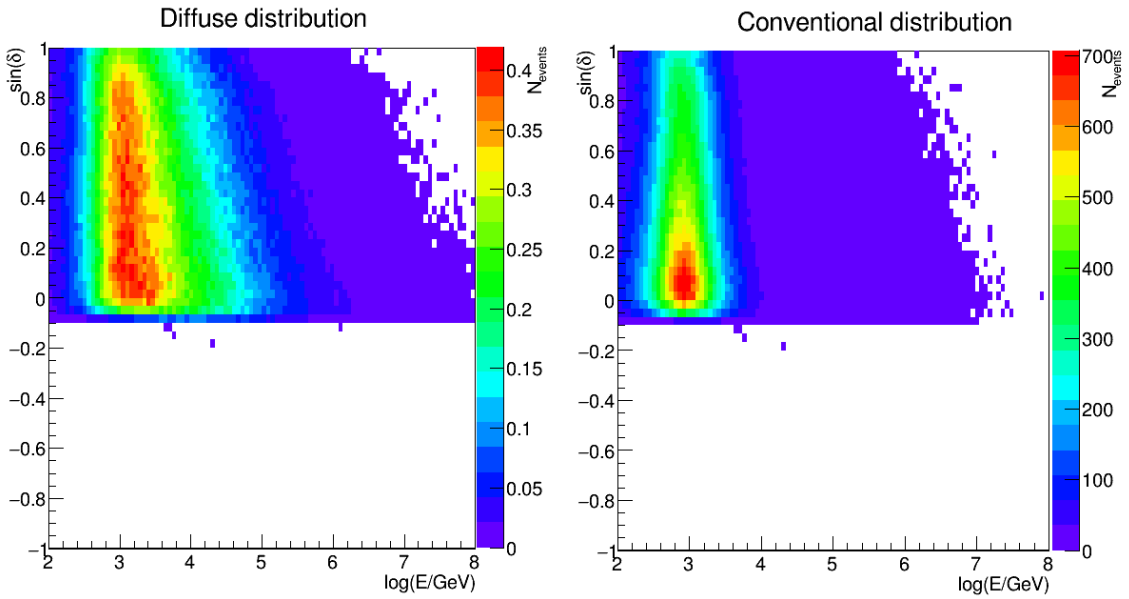

Figure 8.1: The event number density of diffuse-astrophysical events (left) and conventional atmospheric events (right) in $\log_{10}(E/\text{GeV})$ and $\sin\delta$. The colour scale represents the number of events per bin.

8.1.1 Energy distribution

The energy spectrum of the neutrinos can be found by taking the x-axis projection of the histograms (shown in figure 8.1 and 8.2). In both cases the measured event rate falls off at low energies $E \leq 100$ GeV (see figure 8.3). This is because lower energy events generate lower photon counts which fall below the threshold for event reconstruction. The atmospheric events follow a steeper power curve ($\Phi_C(E) \propto E^{-3}$) due to meson energy losses in the atmosphere and fall off more rapidly than the astrophysical events ($\Phi_A(E) \propto E^{-2}$) which dominate the event rate at $E \geq 100$ TeV. Event statistics at high energies are limited both by the flux falling off and the limited volume of the detector.

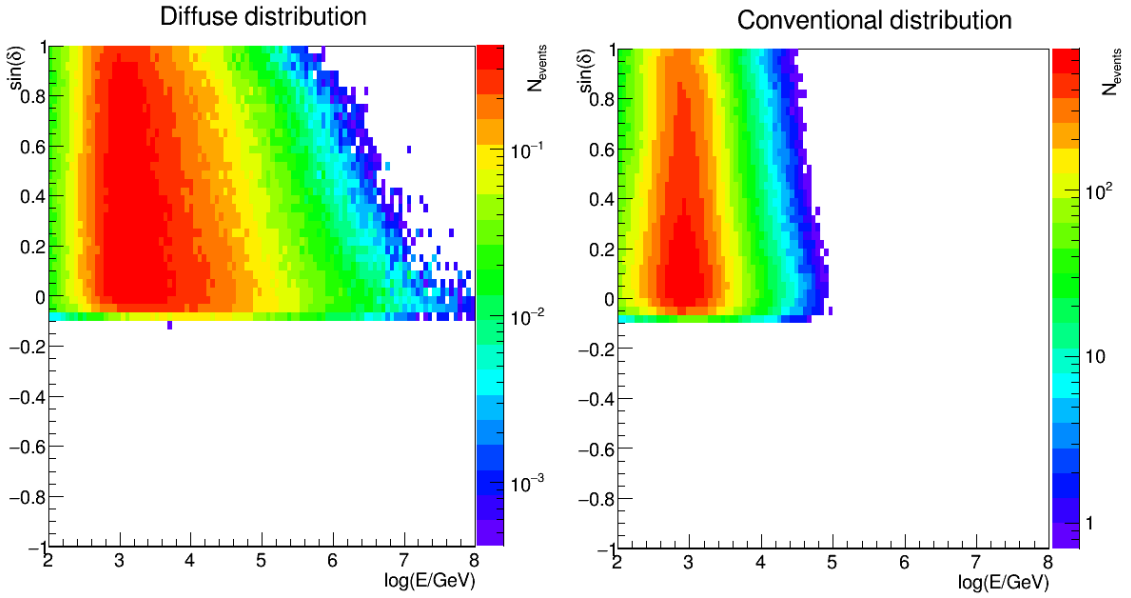

Figure 8.2: The logarithmic-scale of the distribution in figure 8.1. Note that the white space is empty of any event probability.

Spectral Index

The simulation of up-going astrophysical muons is generated under the assumption of a standard power-law $\Phi_A(E) \propto E^{-2}$. However current analyses [42] find the spectral best fit to be around $\Gamma = 2.6$. In order to test different power laws we fold this into the astrophysical weights:

$$w_{astro} = w_{E^{-2}} \rightarrow w_{astro} = \frac{\Phi_{E^{-\Gamma}} E^{-\Gamma}}{\Phi_{E^{-2}} E^{-2}} \times w_{E^{-2}} \tag{8.1}$$

The respective flux normalizations $\Phi_{E^{-\Gamma}}$ and $\Phi_{E^{-2}}$ are divided to conserve the total signal event number in equation 8.1. The changes in the E-sin δ distribution with spectral index Γ are shown in figure 8.4. Note that in the stacking analysis discussed in chapter 9 we only consider the case of $\Gamma = 2$.

8.1.2 Declination distribution

Across the northern sky the conventional atmospheric flux dominates the diffuse astrophysical flux by around 3 orders of magnitude (see figure 8.5, where the astrophysical distribution is scaled up by a factor of 700). In both cases event rates peak towards the equator (sin $\delta \sim 0$) and decrease with increasing declination towards the north celestial pole. This can be explained by increased event absorption as the neutrino path through the Earth increases with declination.

8.2 Signal Generation

Generating signal events involves sampling the event arrival directions from the probability density of the signal $S(E, \alpha, \delta, \sigma, \Gamma)$ defined from multiple sources. For a given event, its signal probability is defined as the sum of the sources' point spread functions $\rho_{src}(\alpha, \delta)$ multiplied by the sources' energy distribution $g_{src}(E, \Gamma)$ which is dependent on the assumed spectral index. Each source is given a weight w_j that corresponds to its relative neutrino flux. For event i the

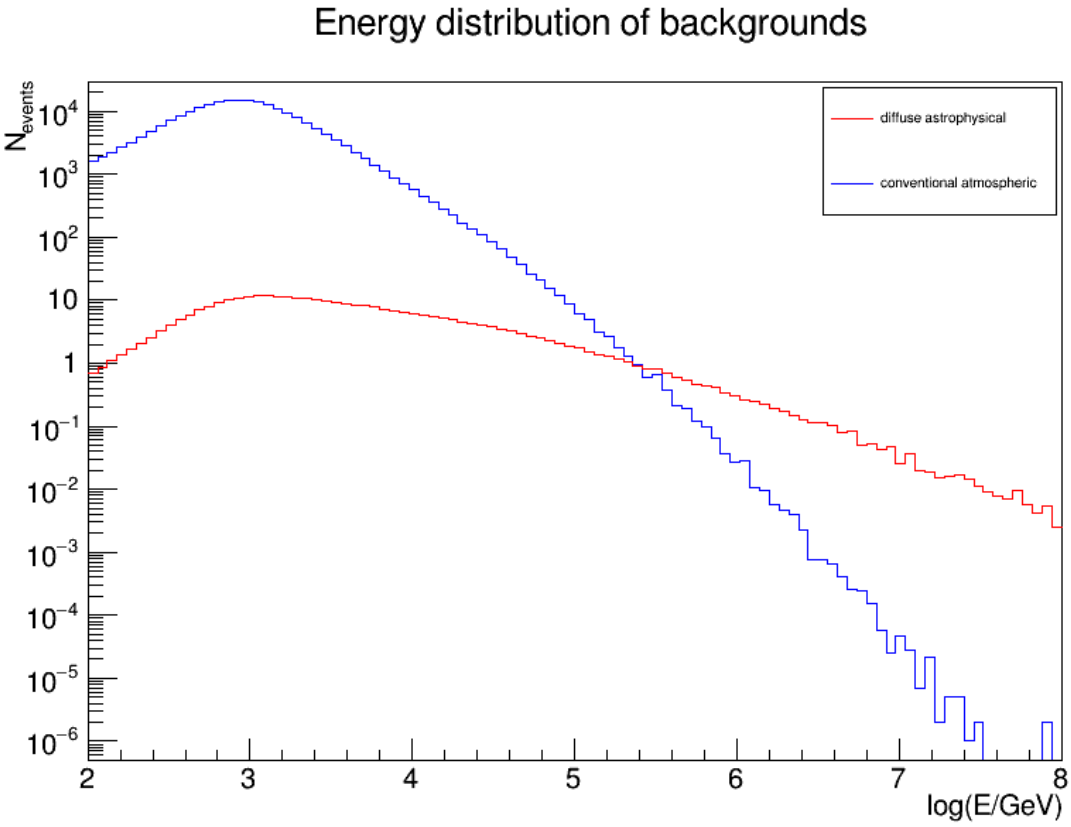

Figure 8.3: The reconstructed energy E distribution of the atmospheric (blue) and astrophysical events (red). The distribution is displayed with the frequency of events per logarithmic bin of energy on the y-axis and the logarithmic reconstructed energy ($\log_{10}(E/\text{GeV})$) on the x-axis. The shape of the spectra reflect the respective spectral indices: $\Phi_C(E) \propto E^{-3}$ for atmospheric events while $\Phi_A(E) \propto E^{-2}$ for the astrophysical events. However the displayed reconstructed energy distributions are both harder due to the effects of the detector.

signal probability density is:

$$S(E_i, \alpha_i, \delta_i, \sigma_i, \Gamma) = \sum_j^{N_{src}} \frac{w_j}{\sum_j w_j} \rho_{src}(\alpha_i, \delta_i, \sigma_i) g_j(E_i, \Gamma) = \sum_j^{N_{src}} \hat{w}_j \rho_{src}(\alpha_i, \delta_i, \sigma_i) g_j(E_i, \Gamma) \quad (8.2)$$

The point spread function ρ_{src} is defined using a von Mises function, a continuous probability distribution defined on a spherical surface and a close approximation of a wrapped normal distribution. For a given event i and source j we find the von Mises function to be:

$$\rho_j(\alpha_i, \delta_i, \sigma_i) = \frac{k_i}{2\pi I_0(k)} e^{k_i \cos \Delta\theta_{ij}} \quad (8.3)$$

where $\Delta\theta_{ij}$ is the angular separation between the event and source and k_i is dependent on the angular resolution of the i^{th} event:

$$k_i \sim \ln(0.5)/(\cos \sigma_i - 1) \quad (8.4)$$

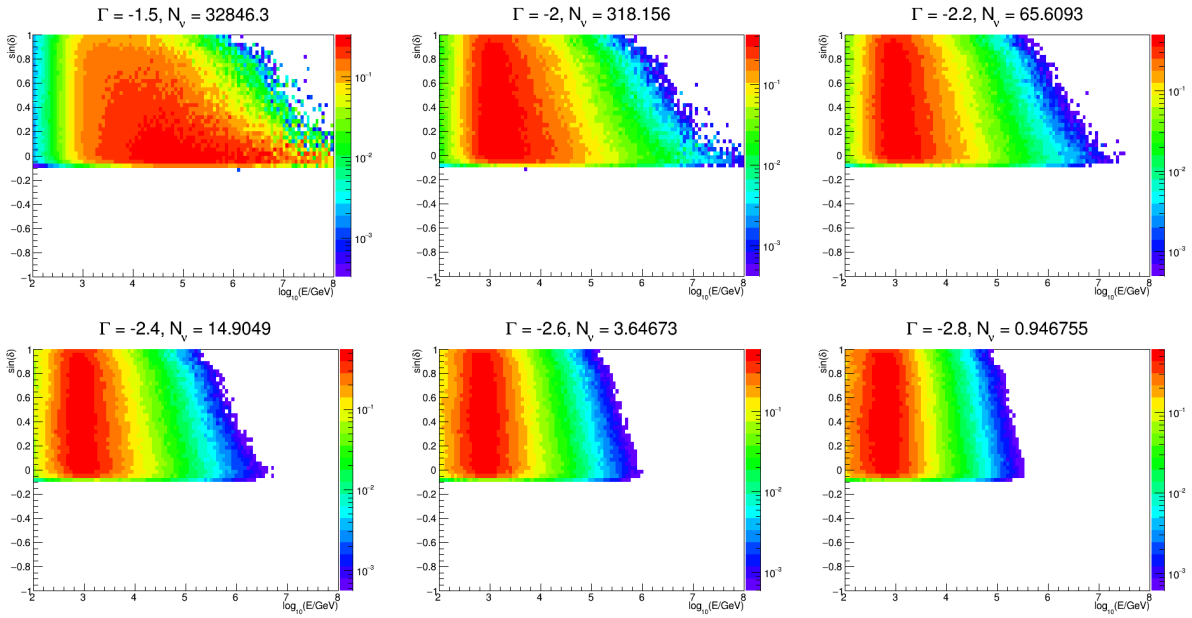

Figure 8.4: The background distributions for $\Gamma = 1.5, 2, 2.2, 2.4, 2.6, 2.8$ are shown from left to right. The value N_ν indicated above each plot is the number of astrophysical events expected for a given spectral index Γ if the total energy flux is conserved. Harder spectral indices will lead to large proportions of high energy events (as is the case for $\Gamma = 1.5$ and $\Gamma = 2$) while softer spectral indices lead to smaller proportions. Eventually the softer values of spectral index result in an event distribution similar in appearance to that of the conventional atmospheric background.

The term $I_0(k)$ is the modified Bessel function of order 0. For small values of k we can simplify equation 8.3 to:

$$\rho_j(\alpha_i, \delta_i, \sigma_i) = \frac{k_i}{4\pi \sinh(k_i)} e^{k_i \cos \Delta\theta_{ij}} = \frac{k_i}{2\pi(e^{k_i} - e^{-k_i})} e^{k_i \cos \Delta\theta_{ij}} \tag{8.5}$$

Each source has equatorial coordinates α_{src} and δ_{src} and a neutrino intensity or flux, which is not known *a priori* and is inferred from a model. One approach would be to assume that the sources are equally intense [5] and hence have approximately equal numbers of neutrino events from each. A different approach would be to use a model in which the neutrino flux is proportional to some observable electromagnetic emission from the same galaxy. The latter approach usually utilizes γ-ray emission as this is expected to correlate with neutrino emission. In the case of a starburst galaxy, we use the arguments from chapter 6 to predict that the neutrino flux is proportional to the far infra-red flux associated with star-formation, with the peak around $60\mu m$ to $100\mu m$. As we will see, the distribution of intensities amongst the sources is far from uniform, in fact under an infra-red to neutrino model the brightest 20 sources account for the majority of the neutrino emission. The latter approach is used to weight the sources in the analysis in chapter 9, where the sources are northern sky starburst galaxies extracted from the IRAS Revised Bright Galaxy Sample (see figure 8.6 for a sky-map of the IRAS sample).

The procedure for generating n_s events from a distribution of sources follows several steps.

1. Select the source to sample events from (randomly selected from a 1-D histogram of source weights, see figure 8.7).

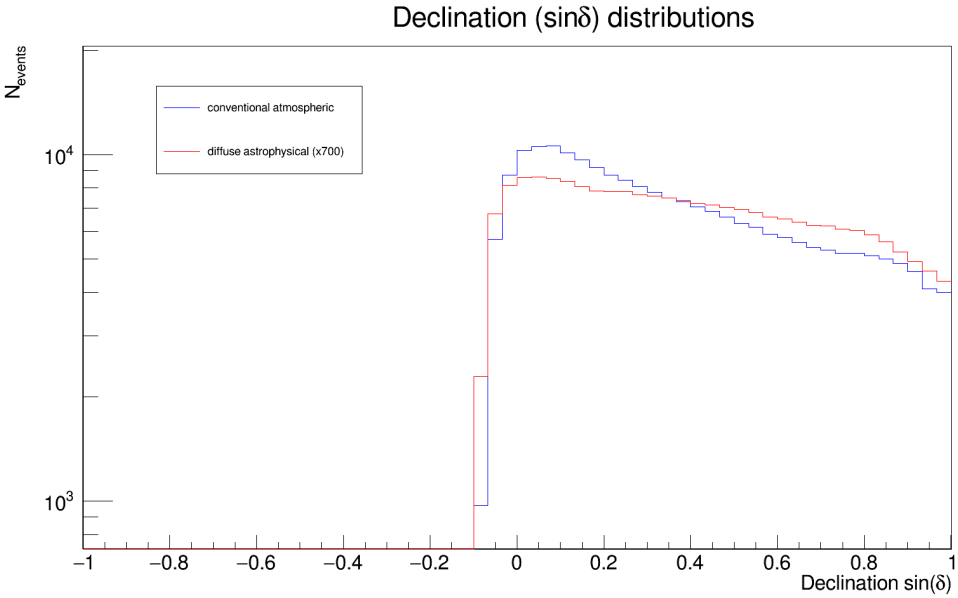

Figure 8.5: Declination distribution of astrophysical and atmospheric backgrounds. The astrophysical distribution is scaled by a factor of 700 to demonstrate the differences between the distributions. The astrophysical distribution is flatter across declination than the atmospheric distribution. Note that solid angle per bin $\Delta\Omega$ is equal for a $\sin\delta$ distribution.

2. Select the event energy according to $g_{src}(E, \Gamma)$.
3. Sample the angular separation $\Delta\theta$ from the von Mises function.
4. Transform the spherical coordinates of the source and event into Cartesian vectors.
5. Define the source vector as an axis of rotation.
6. Rotate event vector about the axis by some random polar angle $\zeta \in (0, 2\pi)$.

By following this procedure for n_s events we obtain a list of signal-like events that follow a signal distribution in the parameter space of observables (see figure 8.9 for the distribution of signal events across the sky).

8.2.1 Selecting the source and event energy

Since we do not know the intrinsic neutrino intensity per source in the analysis, we use a model to predict what the intensity would be based on electromagnetic emission expected to correlate with neutrino emission. Since we are testing star-formation as a predictor of neutrino intensity, we use infra-red emission in the 100-micron band (flux density: $S_{100\mu m}$ [Jy]) to weight the expected neutrino strength per galaxy [50]. The infra-red flux per galaxy is not equitably distributed, instead the brightest 20 sources collectively emit more than half of the total infra-red intensity [78], and the distribution of sources follows a power-law spectrum. Hence we form a histogram of sources from brightest to dimmest, with the bin number corresponding to the flux-rank and the value of the bin corresponding to the relative flux (see figure 8.7). The distribution is normalized such that the integral of the distribution is equal to the entire neutrino flux. We sample events from the distribution, such that more events will be sampled from the brighter sources on average (see figure 8.7). Each source has an energy spectrum, which is found by taking the x-axis projection of the energy-$\sin\delta$ histogram for $\sin\delta_{src}$. The resulting 1-dimensional histogram will show the energy distribution of the source weighted by its position in the sky, with attenuation

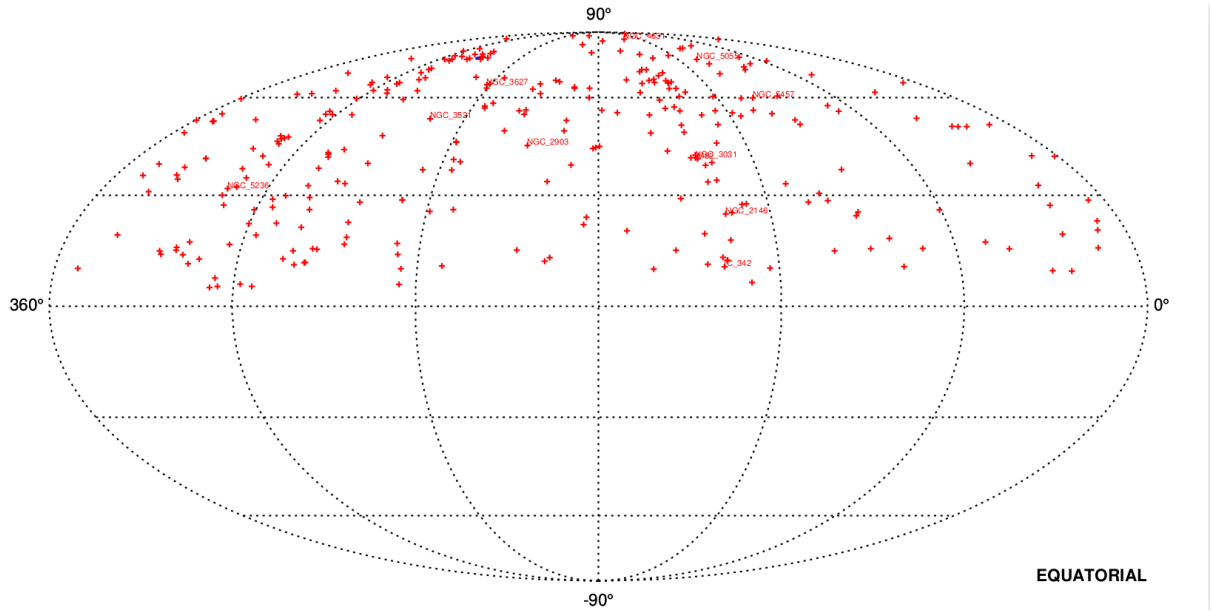

Figure 8.6: A sky-map of the northern objects in the IRAS Revised Bright Sample. The northern sky starburst galaxies are denoted with red crosses with the brightest 10 labelled.

increasing for higher declination values. The energy of the event is sampled from the histogram (see figure 8.8).

8.2.2 Sampling arrival directions

To extract the angular separation $\Delta\theta_{ij}$ between event i and source j we sample from the source's point spread function, using the sample-by-integration method. The point spread function ρ is defined with a von Mises function with a width defined by the event's angular resolution σ_i. We integrate the von Mises function over $\cos\theta$ and set it equal to a random number between 1 and 0: $R \in (1, 0)$

$$R = \int_1^{\cos\Delta\theta} \frac{k}{2\pi(e^k - e^{-k})} e^{k\cos\theta'} d\cos\theta' \tag{8.6}$$

Under the assumption of a small resolution (and therefore large $k > 700$):

$$\cos\Delta\theta = 1 + \frac{1}{k}\ln(1 - R) \tag{8.7}$$

Since only track objects are considered, this assumption is used throughout the analysis. A minor quality cut $\sigma < 5^0$ is applied to remove the small number of poorly resolved events. The newly generated event is offset from the source coordinates according to the sampled angular distance $\Delta\theta = \cos^{-1}(1 + \frac{1}{k}\ln(1 - X))$.

8.2.3 Vector Rotation

Having calculated the angular distance between the event and source, we assign a polar angle to the event. We use the astronomical coordinates (α, δ) to define unit vectors $(|\vec{r}| = 1)$ in a spherical coordinate system (r, θ, ϕ). We then perform a standard transformation to convert them into Cartesian vectors:

$$x = \sin\theta\cos\phi = \cos\delta\cos\alpha \tag{8.8}$$

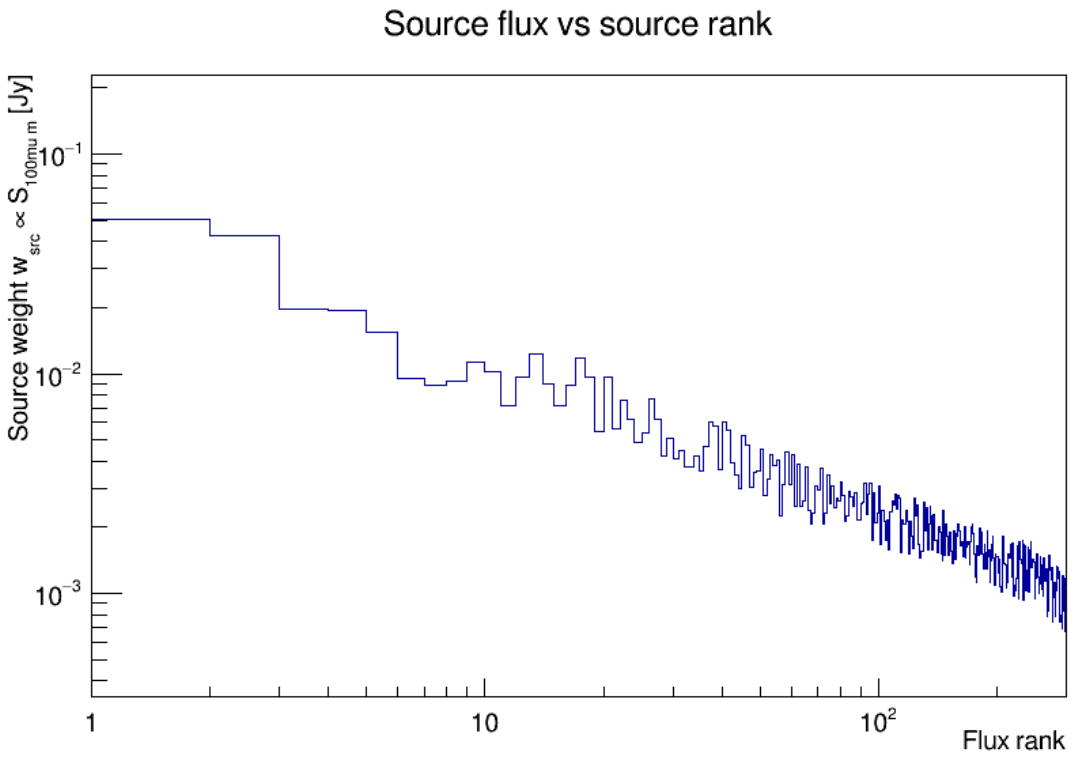

Figure 8.7: Distribution of weights $\hat{w} \propto S_{100\mu m}$ by source "rank'. The distribution is displayed logarithmically on both axes, resulting in the compression of the bins across the x-axis. The first twenty sources account for the majority of the collective neutrino production.

$$y = \sin\theta \sin\phi = \cos\delta \sin\alpha \tag{8.9}$$

$$z = \cos\theta = \sin\delta \tag{8.10}$$

We define a source vector $\vec{u}$ and a preliminary event vector $\vec{v}'$ which is initially assigned a declination: $\delta_\nu = \delta_{src} - \Delta\theta$. The source vector $\vec{u}$ is used to define the axis of rotation, and the preliminary event vector is rotated about the axis by some polar angle ζ using Rodrigues' rotation formula [34]:

$$\vec{v} = \vec{v}' \cos\zeta + (\vec{u} \times \vec{v}') \sin\zeta + \vec{u}(\vec{u} \cdot \vec{v}')(1 - \cos\zeta) \tag{8.11}$$

The final event position is defined with the resultant cartesian vector $\vec{v}$, from which the final event coordinates are found by converting to spherical coordinates.

We have outlined the procedure for drawing n_s events from$S(E, \delta, \alpha, \sigma, \Gamma)$, $N_{A,\text{diff}}$ events from $A(E, \sin\delta)$ and N_C events from $C(E, \sin\delta)$. Example simulated neutrino skies are shown in figures 8.9 and 8.10. The simulated event lists are used to test the starburst stacking analysis in chapter 9.

8.3 Summary

Generating realistic distributions of neutrino events with signal and background components is necessary to test the sensitivity and discovery potential of the point source analysis. Background events are sampled from two dimensional histograms of reconstructed energy and declination

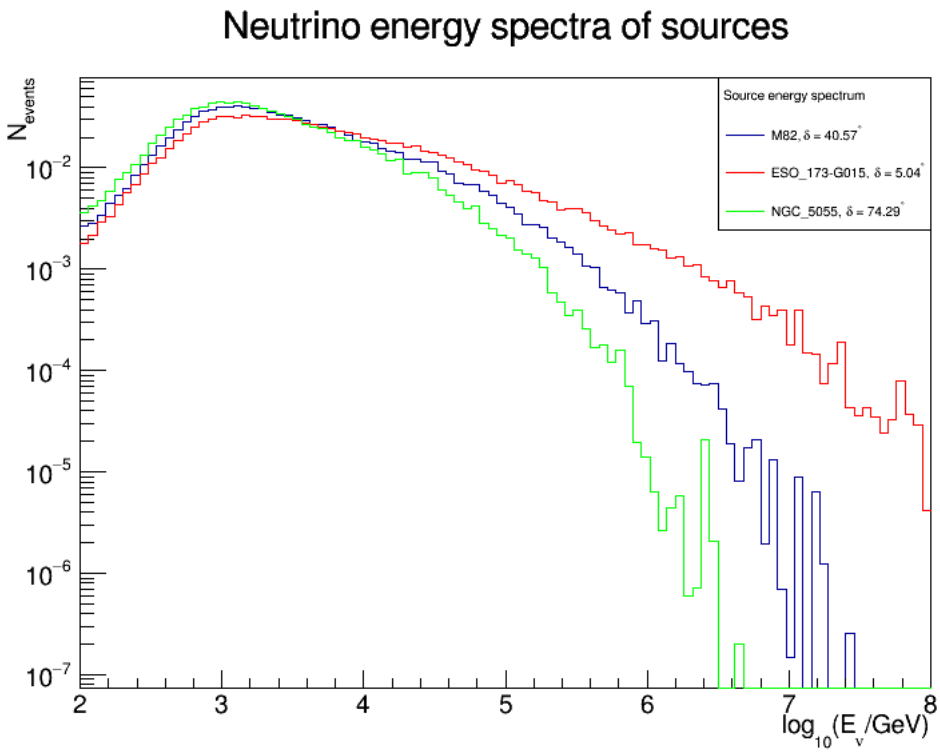

Figure 8.8: The energy spectra of IRAS galaxies M82, ES0 173 G015 and NGC 5055 (M63), with declinations δ at 40.57°, 5.04° and 74.29° respectively. The energy distributions are equally normalized, although the sources are weighted differently. These galaxies are displayed to demonstrate how the arrival declination of a neutrino source affects its energy distribution observed at Earth. The spectrum of higher declination sources will be suppressed at higher energies relative to low declination sources. All sources displayed have an assumed spectral index of $\Gamma = 2$.

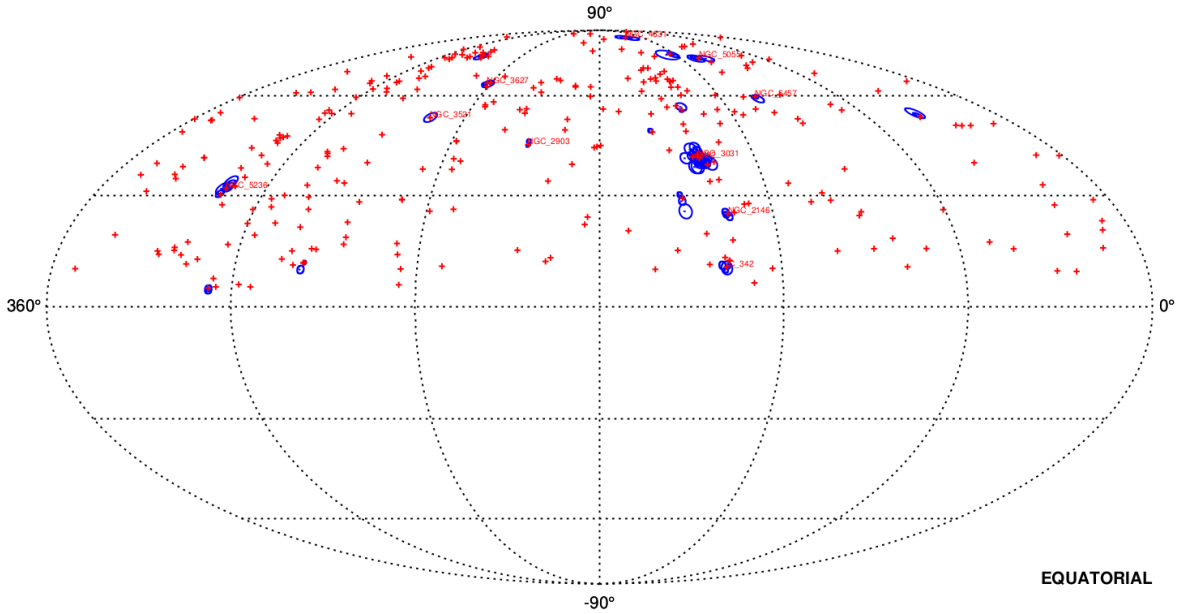

Figure 8.9: Example sky-map, 100 events sampled from brightest 100 sources (shown with red crosses). Signal events are indicated with blue circles whose radii are equal to the events' median angular resolution.

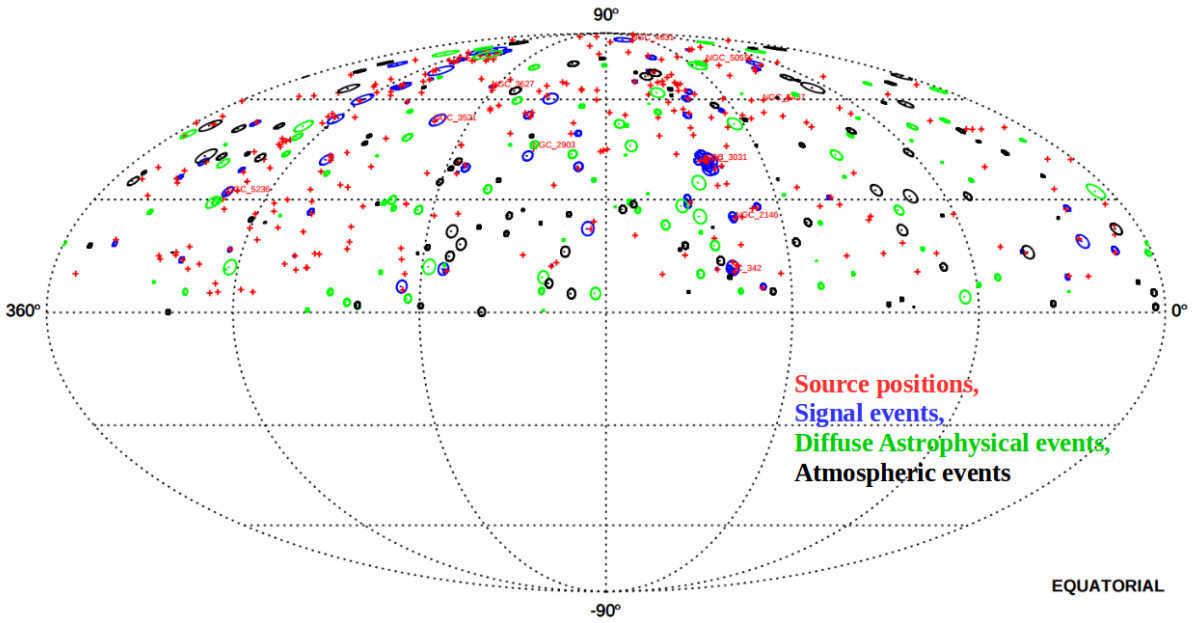

Figure 8.10: A simulated sky with 100 signal events (blue), 100 astrophysical background events (green) and 100 conventional atmospheric events (black) with the IRAS RBGS (red crosses), with the brightest 10 labelled. Note that signal events cluster into hotspots around the brightest 20. The relative astrophysical and atmospheric event numbers are not realistic in this example, equal numbers are assumed for the purpose of illustration.

and then assigned random right-ascension coordinates. Signal events are sampled from the point spread functions centred on the coordinates of catalogue sources, with events assigned per source according to the source weight under the signal hypothesis. The ratios between the three components: signal, astrophysical background and atmospheric background are controlled by the analysis parameter n_s and nuisance parameters N_A and N_C. The energy distribution of astrophysical events is set by default to $\Gamma = 2$ but can also be re-weighted in the case of other spectral indices. The sampling algorithm is employed to simulate the flux from starburst galaxies.

Chapter 9

Starburst Stacking Analysis

In chapter 6 we devised energetics arguments for calculating the starburst contribution to the neutrino flux, finding star-forming galaxies may account for the majority of the neutrino flux under the most optimistic assumptions. Given the evolution of the star-formation rate we expect that a some fraction (up to $\sim 2\%$) of the starburst-neutrino flux would be distributed amongst starburst galaxies in the local Universe (such as those represented in the IRAS sample). Given a sufficiently high flux, it would be possible to observe an excess number of events coming from the direction of the brightest nearby starburst galaxies, producing a distribution of neutrino events incompatible with a purely diffuse neutrino sky. In this chapter, a stacked point source analysis is performed on simulations of the up-going (northern sky) muons described in chapter 3 [6] using the methods described in chapter 8. This is done for the purpose of measuring the sensitivity and discovery potential of the analysis to a starburst neutrino signal. Application of this analysis to real data (known as analysis "unbinding") requires review and then approval from the IceCube collaboration and is intended at a later stage but is beyond the scope of this chapter and thesis. We used the coordinates of starburst galaxies from the IRAS Revised Bright Galaxy Sample to fix the source positions. The analysis is sensitive to the fraction of neutrino events that are signal-derived as opposed to originating from the diffuse backgrounds. The analysis measures the proportion of signal events n_s/N for a given neutrino sky that are a best fit to the expected strength of the catalogue sources and finds the likelihood of the observed signal given the background-only hypothesis.

Throughout this chapter we implicitly assume a spectral index of $\Gamma = 2$ in the sampling and fitting. As a result the values of the energy flux remain constant with logarithmic intervals of energy. The values tested are shown in values of the point source energy flux $E^2 d\Phi_0/dE$ and as a fraction of the astrophysical diffuse energy flux $E^2 d\Phi_{ast}/dE$. As a form of shorthand we define units $\hat{\Phi}_0$ and $\hat{\Phi}_{ast}$ where the former is set to:

$$\hat{\Phi}_0 = E^2 \frac{d\Phi_0}{dE} = 10^{-12}\,\mathrm{TeV cm^{-2} s^{-1}} \tag{9.1}$$

while the latter is:

$$\hat{\Phi}_{ast} = E^2 \frac{d\Phi_{ast}}{dE} = 10^{-8}\,\mathrm{GeV cm^{-2} s^{-1} sr^{-1}} \tag{9.2}$$

The value of Φ_{ast} is taken from the flux normalization of the up-going muon sample[6]. Note that $\hat{\Phi}_{ast}$ should classically be considered an intensity since it is defined in units of solid angle [76]. However it is common practice in IceCube to use flux to refer to intensity, so we will follow a convention of distinguishing between a point source flux ($\Phi_{\mathrm{ptsrc}}[\mathrm{cm^{-2} s^{-1}}]$) and a diffuse flux ($\Phi_{\mathrm{diff}}[\mathrm{cm^{-2} s^{-1} sr^{-1}}]$).

9.1 Method

In this analysis we use a stacked likelihood function to test for the presence of a signal component in the ensemble of simulated skies. In this section we define the form of the likelihood function, the hypothesis being tested and the terms *sensitivity* and *discovery potential* which are used to quantify the effectiveness of our analysis.

9.1.1 Likelihood Function

To determine the character of the flux from a given source class, in this case starburst galaxies, we would fit the expected number of signal events n_s and the spectral index Γ of the starburst flux using a likelihood function accounting for the relative contribution of different backgrounds. However as noted before in this study we simplify matters by keeping the spectral index fixed at $\Gamma = 2$. Two approaches could be taken in estimating the background probability per event:

1. Bin real event data in energy and declination, effectively scrambling the data (removing any signal-like clusters present) to create a single background distribution: $B = B(E, \sin\delta)$

2. Use simulation derived background distributions to create separate background PDFs for diffuse astrophysical $A(E, \sin\delta)$ and atmospheric (conventional) $C(E, \sin\delta)$ background. Note that the prompt background is ignored as the prompt component is negligible in the up-going muon sample [32].

Given these approaches, there are two ways of finding the Likelihood function:

Scrambling LLH

The likelihood function with a background obtained via scrambling is shown in equation 9.3.

$$\mathcal{L}(n_s, \Gamma) = \prod_i^N \frac{n_s}{N} S(E_i, \alpha_i, \delta_i, \sigma_i, \Gamma) + (1 - \frac{n_s}{N}) B(E_i, \sin\delta_i) \tag{9.3}$$

The scrambling method defines its background PDF from the real data with the event azimuth (or right ascension) scrambled. The method has the advantage of decoupling our analysis from the accuracy of a given simulation model and minimizes nuisance parameters.

Simulation LLH

The likelihood function with a simulation derived background is shown in equation 9.4.

$$\mathcal{L}(n_s, \Gamma) = \prod_i^N \frac{n_s}{N} S(E_i, \alpha_i, \delta_i, \sigma_i, \Gamma) + \frac{N_A - n_s}{N} A(E_i, \sin\delta_i) + \frac{N_C}{N} C(E_i, \sin\delta_i) \tag{9.4}$$

The simulation method relies on simulated distributions of the atmospheric and diffuse fluxes, allowing us to probe the effects of different neutrino distributions on the performance of the analysis. However it introduces two nuisance parameters: the number of astrophysical events, $N_A = N_{A,\text{diff}} + n_s$, and the number of atmospheric (conventional) events N_C. We impose the natural constraints, $N_C + N_A = N$ and $n_s \leq N_A$. In this chapter we use the simulation method to obtain our sensitivities.

In practice we fit the parameters using the log of the likelihood:

$$\begin{aligned}\ln \mathcal{L}(n_s, \Gamma) &= \sum_i^N \ln[\frac{n_s}{N} S(E_i, \alpha_i, \delta_i, \sigma_i, \Gamma) + \frac{(N_A - n_s)}{N} A(E_i, \sin(\delta_i)) + \frac{N_C}{N} C(E_i, \sin\delta_i)] \\ &= \sum_i^N [\ln(n_s S(E_i, \alpha_i, \delta_i, \sigma_i, \Gamma) + (N_A - n_s) A(E_i, \sin\delta_i) + N_C C(E_i, \sin\delta_i))] - N \ln N\end{aligned} \tag{9.5}$$

The term $N \ln N$ is constant and as such it is dropped. The signal probability distribution function (PDF) is taken as the sum of point spread functions of the sources, weighted by their expected flux and energy spectra. The PSF is defined using the von Mises function:

$$S(E_i, \alpha_i, \delta_i, \sigma_i, \gamma) = \sum_j^{N_{src}} \frac{\bar{w}_j k_i}{2\pi(e^k - e^{-k})} e^{k_i \cos(\Delta\theta_{ij})} g_j(E_i, \Gamma) \tag{9.6}$$

where $k_i \sim \ln(0.5)/(\cos(\theta_i) - 1)$ and $\Delta\theta_{ij}$ is the angular distance between the i^{th} event and j^{th} source. The normalized energy PDF $g_j(E_i, \gamma)$ of the j^{th} source accounts for the acceptance of the source at δ_j and the spectral index γ, assumed to be uniform for each source. The relative weight of the source is denoted by $\bar{w}_j$:

$$\bar{w}_j = \frac{w_j}{\sum_j^{N_{src}} w_j} \tag{9.7}$$

The weight w_j is derived from the contribution of the source to the flux i.e. the total number of events expected:

$$w_j = \int_{E_{\nu,min}}^{E_{\nu,max}} \Phi_{0,j} h_j(E_\nu) A_{\text{eff}}(\theta_j, E_\nu) dE_\nu \tag{9.8}$$

where $A_{\text{eff}}(\theta_j, E_\nu)$ is the effective area for a muon neutrino for a given zenith angle θ_j and energy E_i, $h_j(E_\nu)$ accounts for the energy spectrum of the source and $\phi_{0,j}$ is the overall flux normalization. In this case we set the energy bounds to: $E_{\nu,min} = 10^2$ GeV and $E_{\nu,max} = 10^8$ GeV. We assume that all sources share the same spectral index and hence simplify w_j to:

$$\begin{aligned}w_j &= [\phi_{0,j}] \cdot [\int_{E_{\nu,min}}^{E_{\nu,max}} h(E_\nu, \Gamma) A_{\text{eff}}(\theta_j, E_\nu) dE_\nu] \\ &= [C w_{j,model}] \cdot [w_{acc}(\theta_i, \Gamma)]\end{aligned} \tag{9.9}$$

which splits the weight into a model term with $w_{j,model}$ being proportional to the relative expected neutrino flux and an acceptance component $w_{acc}(\theta, \Gamma)$ which is determined by the source's position in the sky θ_j and spectral index Γ. Since we use a relative weight $\bar{w}_j$, the conversion factor C, assumed to be constant, does not need to be known explicitly.

9.1.2 Model Assumptions

We do not know the neutrino flux of a given source ahead of time, so $w_{j,model}$ is dependent on the model assumed for the neutrino emission. The approach taken by a previous blazar stacking analysis [5] is to set the weight equal to the γ-ray emission measure by Fermi-LAT (see chapter 4 for a description). Specifically they use the measured energy flux in the range: $100\,\text{MeV} < E_\gamma < 100\,\text{GeV}$:

$$w_{j,\text{blazar}} = \int_{100\text{MeV}}^{100\text{GeV}} E_\gamma \frac{d\phi_{\gamma,j}}{dE_\gamma} dE_\gamma \tag{9.10}$$

In our case we assume direct correlation between the flux-density at 100 microns, $S_{100\mu m}$, and the neutrino flux, to give:

$$w_{j,\text{starburst}} = S_{100\mu m} \tag{9.11}$$

Thus we obtain the model component $w_{j,model}$ of the signal weight w_j per source.

9.1.3 Hypothesis Testing

We perform a standard maximum likelihood fit to determine the most probable values of n_s and Γ and determine the "'p-value" by estimating the test statistic X under the assumption of the truth of the background ($n_s = 0$) hypothesis. We define our test statistic X as the log of the ratio of the likelihoods for the null and signal hypotheses (see equation 9.12). Under Wilk's theorem we expect the test-statistic to follow a X^2 distribution:

$$\begin{aligned} X &= 2\ln(\frac{\mathcal{L}(\hat{n}_s, \hat{\Gamma})}{\mathcal{L}(0)}) \\ &= -2\ln(\frac{\mathcal{L}(0)}{\mathcal{L}(\hat{n}_s, \hat{\Gamma})}) \end{aligned} \tag{9.12}$$

We find the most likely values of n_s and Γ by scanning across the parameter space defined by them and selecting the parameter space coordinates for which we find the maximum value of our test statistic X. In our case we hold Γ fixed and scan across possible n_s. In practice this is achieved by finding the *minimum* value of the negative test-statistic $-X(n_s, \gamma)$

$$-X(n_s, \Gamma) = -2\ln(\frac{\mathcal{L}(\hat{n}_s, \hat{\Gamma})}{\mathcal{L}(0)}) = -2(\ln(\mathcal{L}(\hat{n}_s, \hat{\Gamma})) - \ln(\mathcal{L}(0)) \tag{9.13}$$

Significance and Statistical Power

Given a set of neutrino events $\vec{x}$, we control the origins of the events with our nuisance parameters N_C and N_A and our scanned parameter n_s. The latter parameter determines if the set of events corresponds to our null hypothesis $n_s = 0$ or to one of a number of signal hypotheses where $n_s = \hat{n}_s > 0$. For each hypothesis we create an ensemble of events, where the individual positions are random but follow distributions in space and energy determined by the signal PDF $S(E, \alpha, \delta)$ and background PDFs $A(E, \sin\delta)$, $C(E, \sin\delta)$ with proportions controlled by the aforementioned parameters. For the null hypothesis, we calculate the value of the test-statistic X for each member of an ensemble of events and find the normalized background distribution of test-statistics. The procedure is repeated for one or more signal hypotheses until we have multiple distributions. One would expect our likelihood ratio to often correspond to unity leading to a large proportion of test statistics in the zero bin as $X = \ln(\mathcal{L}(\hat{n}_s, \Gamma))/\mathcal{L}(0) = \ln(1) = 0$. We also expect signal test-statistic distributions about some average greater than zero, with a value rising for stronger signals. An example of this is displayed in figure 9.1, with overlapping distributions of the test-statistic X corresponding to the null hypothesis and alternative hypothesis along with the experimental test-statistic X_{exp}.

Suppose now that we apply our analysis to a real set of events and we measure a test statistic X_{exp} corresponding to the most likely number of signal events $\hat{n}_s$ given our data. The significance of this result is defined as the fraction of the time which our null hypothesis predicts a test statistic equal to or greater than X_{exp}, measured by integrating our null distribution from X_{exp} to infinity.

$$\alpha = \int_{X_{exp}}^{\infty} P(X, \theta_0)dX = \int_{X_{exp}}^{\infty} P(X, n_s = 0)dX \tag{9.14}$$

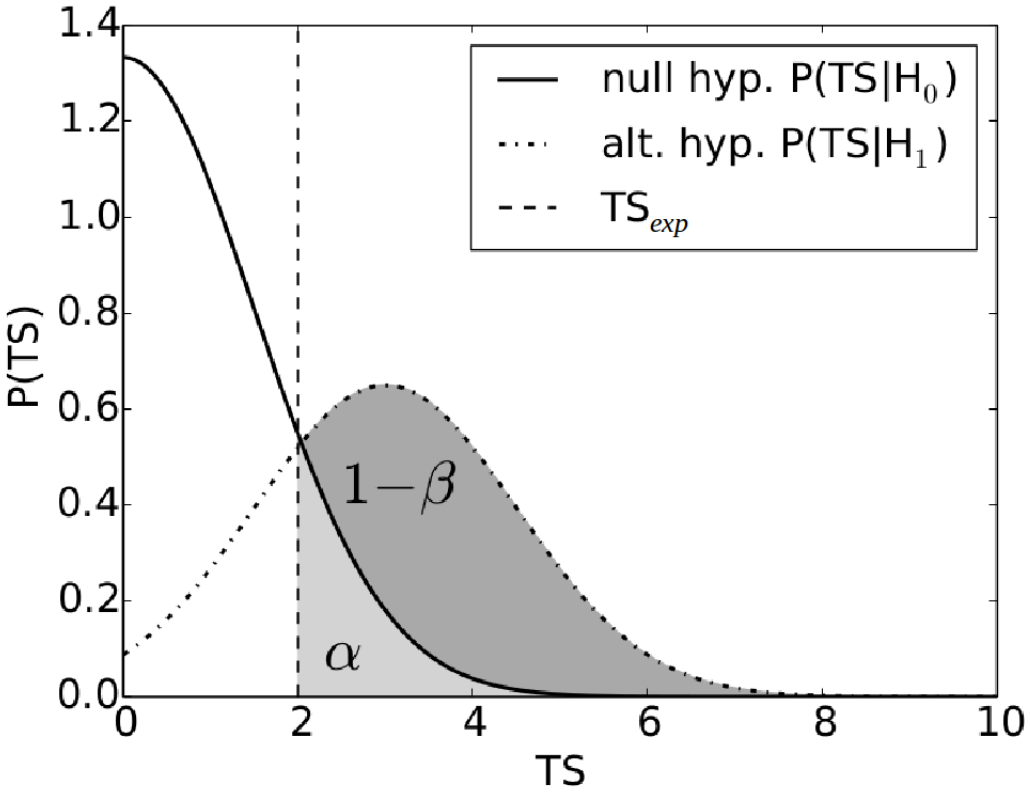

Figure 9.1: An example showing how significance α and statistical power $1-\beta$ are defined in our analysis. The critical test statistic TS_{exp} is the test-statistic for a measurement of a given signal strength. The measurement may be explained by the signal hypothesis H_1 or as a statistical fluctuation from the background H_0. The significance α is the percentage of the null hypothesis TS distribution that exceeds the experimental test statistic shown in the shaded light grey region. Statistical power is the percentage of the signal hypothesis TS exceeding $\mathrm{TS}_{\mathrm{exp}}$ shown in dark grey.

The smaller our value of α the less often the null hypothesis predicts the test-statistic and the more significant our result. This definition of α is identical to the often used p-value used in statistical sciences. The significance of our measured signal determines the probability of measuring X_{exp} (or greater) given the truth of the background hypothesis. For example a measured significance $\alpha = 0.001$ means that there is only a 0.1 % chance of observing X_{exp} under the background hypothesis. Statistical power, $(1 - \beta)$, is defined as (or greater) the fraction of the time that, given the truth of the signal hypothesis, we would see our measured test-statistic or one greater:

$$\beta = \int_0^{X_{exp}} P(X, \theta_s) dX \rightarrow 1 - \beta = \int_{X_{exp}}^{\infty} P(X, \theta_s) dX = \int_{X_{exp}}^{\infty} P(X, n_s = \bar{n}_s, \Gamma = \bar{\Gamma}) dX \quad (9.15)$$

The greater the statistical power of the test-statistic corresponding to the tested signal hypothesis, the more often we should expect our signal hypothesis to consistently predict the measurement. A statistical power of $1 - \beta = 0.9$ means that, given the truth of the signal hypothesis, there is a 90 % chance of the experimental test-statistic or one greater being measured.

Sensitivity and Discovery Potential

The ability of the analysis to place upper limits on the signal strength is known as its sensitivity, while its ability to reject the background hypothesis, given the truth of the signal hypothesis, to a high level of confidence is known as its discovery potential. Both of these values are calculated using simulations of what the distribution of events would be given a signal of strength n_s and spectral shape Γ. We define the sensitivity and discovery potential of our analysis using the significance α and the statistical power $1 - \beta$ of a measured test-statistic.

In the context of any point source analysis, sensitivity and discovery potential are defined in relation to the measurement of a point source flux Φ_{ptsrc} where the normalization of the flux directly translates to the number neutrino events originating from the point sources. The more intense the flux, the better our point source analysis is able to distinguish it from the diffuse background. The strength at which the flux can be distinguished from the background with a high level of significance (small α) and reasonable statistical power is the strength our analysis is *sensitive* to. If the strength of the flux is increased to the point where there is a negligible chance of the flux being a background fluctuation, we can claim a discovery. The value of α for which one can claim a discovery has been debated [60], but the commonly agreed value is $\alpha \sim 3 \times 10^{-7}$, the integral of a normal distribution from infinity to five standards deviations away from the mean, the famous "5σ" value. Here we adopt the following definitions:

	α	$1 - \beta$
Sensitivity	0.5	0.9
Disc. Potential	$\sim 3 \times 10^{-7}$ (5σ)	0.5

Our definition of sensitivity reflects what we expect to measure given the truth of the background hypothesis (i.e. no real signal is present). The most likely test-statistic X we expect to observe in this case is the median test-statistic of the background distribution, the measurement of which carries a significance of $\alpha = 0.5$ by definition. This observation can be used to define an upper limit and since we wish to observe this value reliably we set a requirement that that statistical power be at least $1 - \beta = 0.9$. This is known as the median 90% Neyman upper limit and it can be thought of as a $\alpha = 0.5$ discovery level. The choice of the values for the discovery potential are somewhat arbitrary. One can define discovery level to be a measured signal at 3σ confidence or 4σ or 6σ. Often the presence of a zero bin means one cannot measure α above a certain value, forcing a redefinition of sensitivity. In our case we do have sufficient test-statistic resolution to measure $\alpha \sim 0.5$ (as demonstrated in figure 9.7). Also properly measuring a 5σ discovery

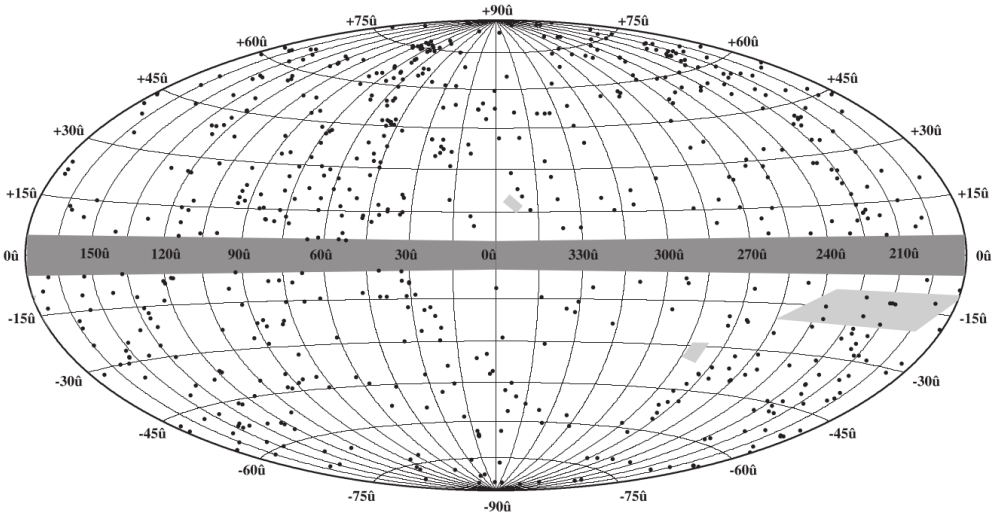

Figure 9.2: The sky map of objects in the IRAS Revised Bright Galaxy Catalogue [78]. The galactic plane region is excluded.

potential requires the generation of ensembles with at least ten million "skies" of events, each sky containing hundreds of thousands of events, unless importance sampling is used. In this chapter we define multiple discovery potentials corresponding to 2σ, 3σ, 4σ and 5σ.

9.2 Data Selection

9.2.1 Neutrino Event List

We use data from the 59-string (IC-59), 79-string (IC-79) and 86-string (IC-86) configurations of IceCube, recorded between May 2009 and April 2012. From these events, we select up-going track events $\theta > 85^0$ or $\delta > -5^0$, effectively removing contamination from air-shower muons. The remaining background consists of atmospheric neutrinos from air showers in the northern hemisphere. The events are well reconstructed with an average angular uncertainty of $\sigma \sim 0.7^\circ$ with virtually all events having $\sigma < 1^0$ at $E > 10$ TeV. The final sample consists of $N = 222813$ total events, with an estimated 318 astrophysical events [42].

9.2.2 Starburst Source Catalogue

The sources in the stacking analysis were drawn from the Revised Bright Galaxy Sample (RBGS) from the Infrared Astronomical Satellite (IRAS), the first observatory to perform an all-sky survey in the infra-red [78], containing 629 galaxies in total (see figure 9.2). Objects in close proximity to the galactic equator ($|b| < 10^\circ$) are excluded from the sample to avoid confusion with objects within the Milky Way. IRAS measured infra-red flux density at discrete bandwidths: $S_{12\mu m}$, $S_{25\mu m}$, $S_{60\mu m}$ and $S_{100\mu m}$, all of which are shown in units of the jansky (Jy). Measuring at different bandwidths allows IRAS to approximate the infra-red spectrum of the sampled galaxies, and estimate their bolometric luminosity, measured in units of solar luminosity $L_\odot$, with the following relation [29] [77]:

$$L_{8-1000\mu m}/L_\odot = 4\pi D^2 \Phi_{8-1000\mu m} = 4\pi D^2 \cdot 1.24 \times 10^{-14}(S_{100\mu m} + 2.58 S_{60\mu m}) \tag{9.16}$$

in which D is the distance to the galaxy in question in units of mega-parsecs (Mpc) and $\Phi_{8-1000\mu m}$ is the bolometric infra-red flux. The characteristics of the infra-red emission can usually be described with a two-component model; with a "hot" component from dust warmed to ~ 150 K

by an active nucleus or a starburst region observed at $12\mu m$ and $25\mu m$ and a "cold" component from dust heated to $\sim$ 40-50 K by normal stellar emission in the galactic disk seen at 60μm and 100μm [31].

Discriminating between Seyfert and starburst galaxies

Seyferts and starburst galaxies are the brightest infra-red emitting galaxies and are both represented in the IRAS bright catalogue. Often the same galaxy can fall into both categories, containing an active nucleus and a region of extreme star-formation. Distinguishing between infra-red radiation from the two mechanisms is achieved by measuring the spectral index $\alpha(\lambda_2, \lambda_1)$ between specific wavelengths λ_2 and λ_1 (where $\lambda_2 > \lambda_1$). This is approximated by measuring the ratio of the flux densities (S) at two different wavelengths (also known as the "colour ratio"):

$$-\alpha(\lambda_2, \lambda_1) = \log(\frac{S_2}{S_1})/\log(\frac{\lambda_2}{\lambda_1}) \rightarrow \frac{S_2}{S_1} = (\frac{\lambda_1}{\lambda_2})^{\alpha} \tag{9.17}$$

By measuring the colour ratios for warm ($\alpha(60\mu m, 25\mu m)$) and cold ($\alpha(100\mu m, 60\mu m)$) infrared emission one can approximate the galaxy's overall spectrum, which will fall somewhere between a blackbody and a non-thermal power-law [80]. The IR "colour" of a starburst galaxy is similar to that of a normal spiral galaxy but with an enhanced warm component [80]. The fraction of $60\mu m$ emission related to the warm emission is characteristic of a starburst galaxy. Seyfert galaxies have flatter spectra explained by non-thermal emission from the active nucleus. The infra-red properties are summarised in the following table.

- Seyfert 1: $\alpha(12\mu\text{m}, 25\mu\text{m}) < -1.5$
- Seyfert 2: $\alpha(12\mu\text{m}, 25\mu\text{m}) > -1.5$, $\alpha(25\mu\text{m}, 60\mu\text{m}) > -1.7 \rightarrow S_{25\mu\text{m}}/S_{60\mu\text{m}} < 4.43$
- Starburst: $-1.7 > \alpha(25\mu\text{m}, 60\mu\text{m}) > -2.5 \rightarrow 4.43 < S_{25\mu\text{m}}/S_{60\mu\text{m}} < 9$

Combining luminosity and the "colour ratio" we implement cuts to create a relatively pure sample of starburst galaxies in the northern sky. After selecting northern sky objects, and removing Seyfert 1 and Seyfert 2 galaxies, the remaining infra-red emission can be scaled directly to star-formation. The galactic star-formation rate Ψ is calculated from the galaxy's bolometric luminosity using the "Global Schmidt Law" [50]:

$$\frac{\Psi}{1\,\text{M}_\odot\text{yr}^{-1}} = \frac{L_{8-1000\mu m}}{2.2 \times 10^{43}\text{ergs}^{-1}} = \frac{L_{8-1000\mu m}}{5.8 \times 10^{9}\text{L}_\odot} \tag{9.18}$$

Defining a starburst galaxy as having $\Psi \geq 10\,\text{M}_\odot\text{yr}^{-1}$, we implement a cut on luminosity to produce our sample. In summary we implement the following cuts on our source catalogue:

1. $\delta > -5°$: Removes southern sky objects from the catalogue
2. $4.43 < \frac{S_{25\mu m}}{S_{60\mu m}} < 9$: Removes Seyfert 1s and 2s
3. $L_{IR} \geq 5.8 \times 10^{10} L_\odot$: Selects for high star-formation rates

These cuts leave a sample of 74 starburst galaxies in the northern sky. The final catalogue used in the analysis contains 75 galaxies with the addition of the ultra-luminous galaxy Arp220 which we consider a special case. Arp220 is the most luminous galaxy in the IRAS RBGS and has characteristics consistent with star-formation while also containing a powerful active nucleus which also features intense circum-nuclear star-formation. Arp220 was excluded as a Seyfert galaxy under the cuts but was re-added to the sample as a special case. Infra-red dust emission induced by star-formation peaks around $100\mu m$, so the flux density $S_{100\mu m}$ of a galaxy is used to weight the source in the analysis. A full list of all starburst galaxies included in this catalogue is displayed in appendix A.

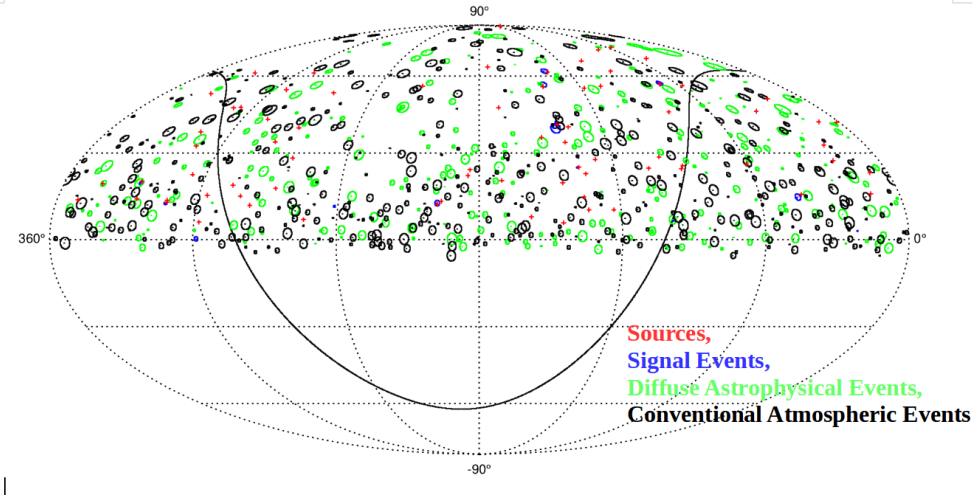

Figure 9.3: A sky-map with a flux of $\Phi_{SB} = 1.24 \times 10^{-12}\,\mathrm{TeVcm^{-2}s^{-1}}$ or 6% of the astrophysical energy flux. The black line represents the equatorial plane.

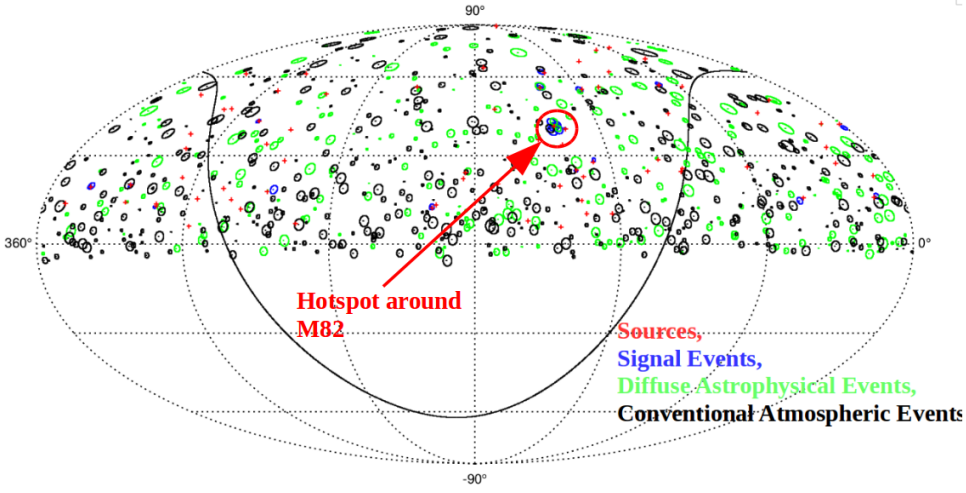

Figure 9.4: A sky map with a flux of $\Phi_{SB} = 18.6 \times 10^{-12}\,\mathrm{TeVcm^{-2}s^{-1}}$ (16% of the astrophysical flux). One can note the increasingly intense hot spot near the position of M82.

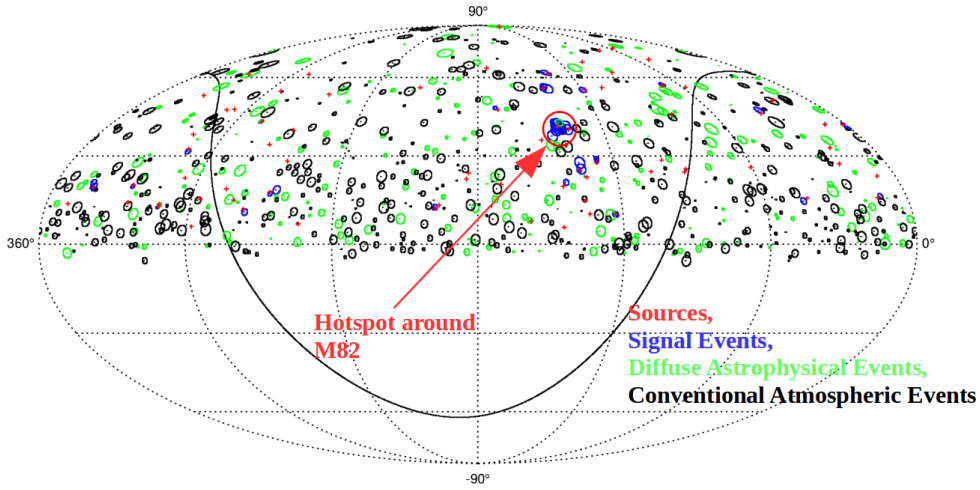

Figure 9.5: A sky-map with a flux of $\Phi_{SB} = 37.2 \times 10^{-12}\,\mathrm{TeVcm^{-2}s^{-1}}$ (31% of the astrophysical flux). This flux seems wildly unrealistic given the results of other point source analyses, as the M82 hotspot should easily be visible to the analysis.

$\Phi_{\mathrm{SB,diff}}[\mathrm{GeV^{-1}cm^{-2}s^{-1}sr^{-1}}\frac{E^{-2}}{(100\mathrm{TeV})^2}]$	$\Phi_{\mathrm{SB,ptsrc}}[\mathrm{TeVcm^{-1}s^{-1}}]$	Φ_{SB}/Φ_{ast}	$\hat{n}_s$ (Poisson Average)
0.1	1.24	0.01	3.21
0.2	2.48	0.02	6.42
0.3	3.72	0.03	9.64
0.35	4.34	0.04	11.24
0.5	6.2	0.06	16.07
1	12.4	0.11	32.13
1.5	18.6	0.16	48.19
2	24.8	0.21	64.25
3	37.2	0.31	96.37

Table 9.1: The values of the point source flux (in units of Φ_0) and fraction of the diffuse intensity (in units of Φ_{ast}) used to define signal hypotheses. The Poisson average of the signal event number $\hat{n}_s/N_{A,\mathrm{diff}} \sim \Phi_{SB}/\Phi_{ast}$ is also shown.

9.3 Results

To calculate the sensitivity and discovery potential of the analysis to the starburst-only catalogue, we generated an ensemble of test skies using the sampling method described in chapter 8. These included 10^7 skies under the null hypothesis (no signal component), which are hereafter referred to as "background skies" along with sets of 10^4 skies with various signal components given by the flux normalization (displayed in table 9.1) with a spectral index $\Gamma = -2$. It was more important to generate more background skies to find stronger levels of discovery, so more computing resources were dedicated towards background generation. Example sky-maps corresponding to the fluxes $6.2\Phi_0$, $18.6\Phi_0$ and $37.2\Phi_0$ are displayed in figures 9.3, 9.4 and 9.5.

9.3.1 Sensitivity

The test-statistic distributions for the hypotheses are shown in figure 9.6. The distributions become wider for progressively higher signals, since the number of signal events fluctuates according to a Poisson distribution. Since the spread of a Poisson distribution increases with mean, larger

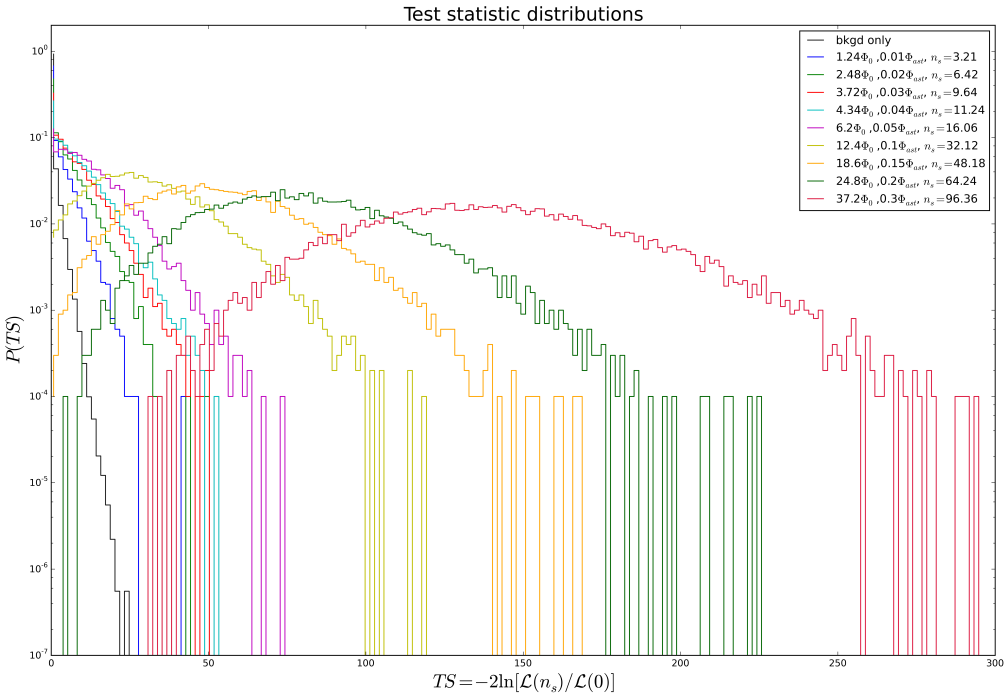

Figure 9.6: Starburst test statistic distribution, with 10^7 background skies and 10^4 for each signal hypothesis. There is no observed overlap between the background skies and the $\Phi_{SB} = 37.2\Phi_0$ (31 % of the total flux) due to the limited statistics but an overlap is expected at the next order of magnitude of sky generation.

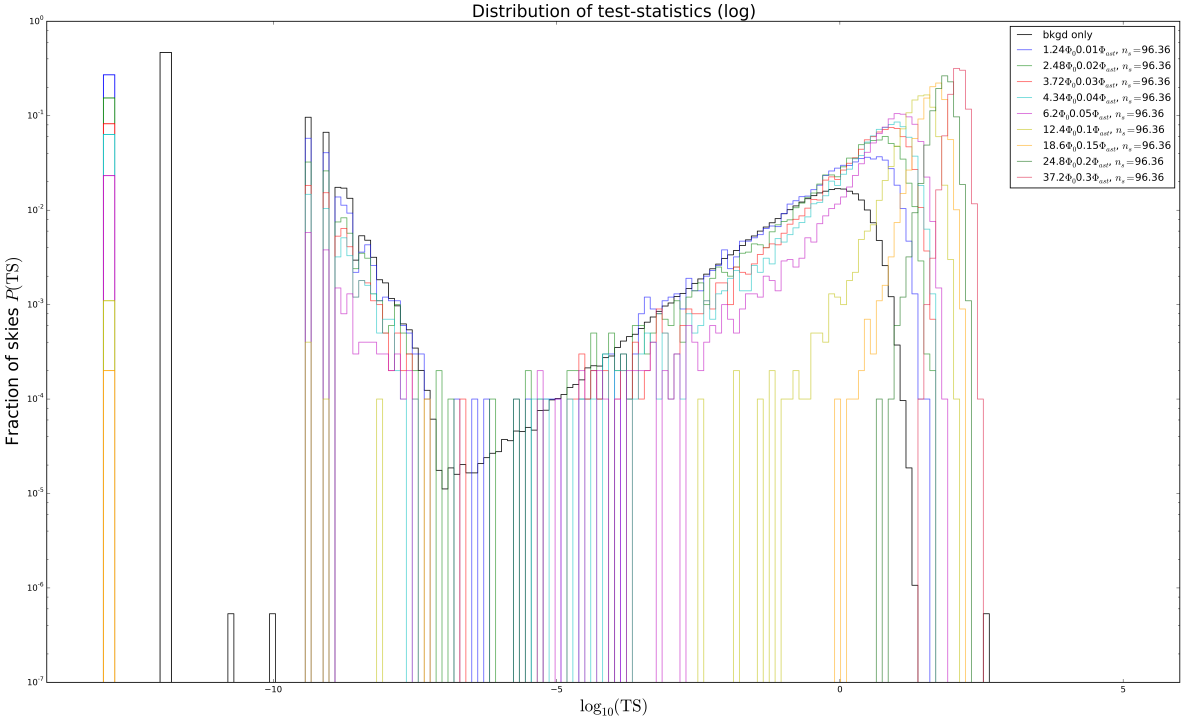

Figure 9.7: The plot of $\log_{10}(X)$ $(= \log_{10}(TS))$, with the same signal hypotheses tested as in figure 9.6. The zero values $(X = 0)$ are represented with an under-flow bin at $X = -12$ for the background distribution and $X = -13$ for the signal hypotheses. A strange valley feature in the logarithmic distribution (around $\log_{10}(X) \sim -7$) is noticeable and may be explained by random variations in the minimization of the likelihood function. Since a large proportion of skies have zero test-statistics, -random fluctuations may lead to a spill-over effect, resulting in the peak in the test-statistics at $\log_{10}(X) \lesssim -7$.

fluxes lead to larger variation in signal number n_s, an effect apparent in the increasing spread of TS distributions with flux (see figure 9.6). In the background distribution, around 47 % of the test-statistics X are equal to zero, making it impossible to measure $\alpha > 0.47$. However we can measure $\alpha = 0.5$ so it is possible to measure sensitivity using the definition of the median Neyman upper limit. Since a large proportion of test statistics much smaller than one we plot the test statistics in log-scale in figure 9.7, with the zero test-statistics shown with an under-flow bin. By integrating the TS distributions in figure 9.7 we obtain a plot of significance α against statistical power $1 - \beta$ (displayed in figure 9.8) for increasing signal strengths as indicated with coloured markers in the figure. Hereafter we refer to the significance (α) and power $(1 - \beta)$ plots for different fluxes as "power curves". Since the test-statistics are binned in log-scale, we can calculate larger values of α $(\log_{10}(\alpha) > -1)$ at higher resolution at expense of lower resolution for smaller α values $(\log_{10} < -1)$. We can obtain the sensitivity of our analysis by finding the "power curve" that intersects the point where $\alpha = 0.5$ and $1 - \beta = 0.9$. This point is indicated from by intersecting blue lines in figure 9.8. Hence we see that the sensitivity of the analysis is $E^2 d\Phi/dE = 3.72 \times 10^{-12}\,\mathrm{TeVcm^{-2}s^{-1}}$, around 3% of the value of the astrophysical flux. This corresponds to ~ 0.08 events per source or, due to the uneven distribution of source flux, 0.32 events per one of the 20 brightest sources.

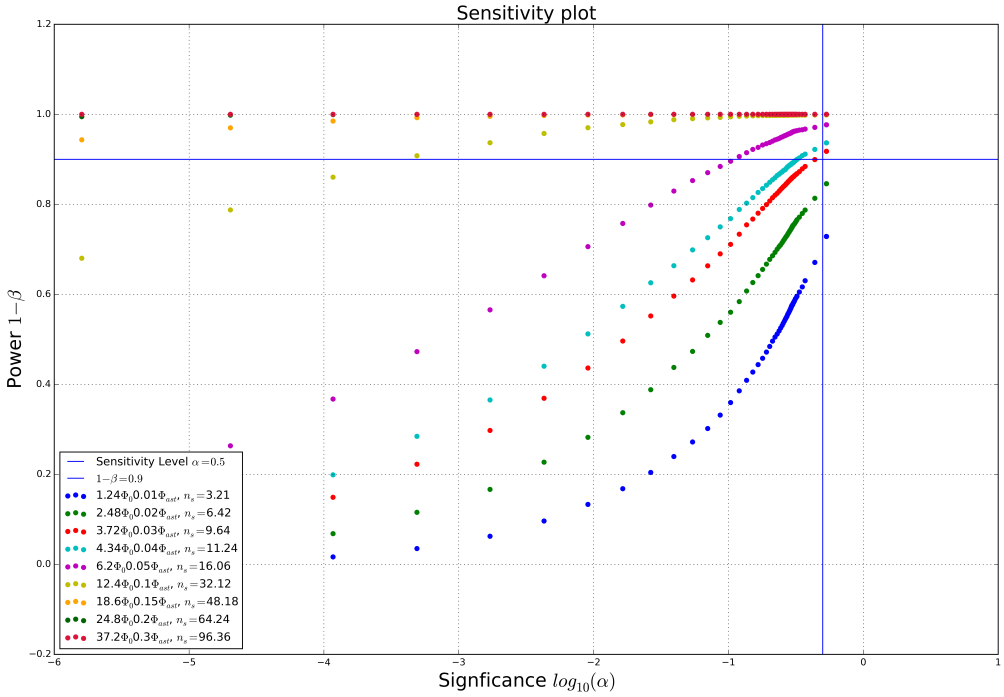

Figure 9.8: The statistical power versus significance for the signal hypotheses tested in figure 9.7. The values are calculated over a logarithmic distribution, allowing large values of α ($\log_{10} > -1$) to be calculated at the expense of smaller values (note decreasing density of markers for $\alpha < -2$). We calculated the sensitivity of the analysis ($\alpha = 0.5$ and $1 - \beta = 0.9$) to $E^2 d\Phi/dE = 3.72 \times 10^{-12}\,\mathrm{TeVcm^{-2}s^{-1}}$, around 3% of the value of the astrophysical flux. We indicate the sensitivity level ($\alpha = 0.5$ and $1 - \beta = 0.9$) with the intersecting blue lines.

	$1-\beta=0.5$	$1-\beta=0.9$
2σ	$3\Phi_0\,[0.025\Phi_{\rm ast}]$	$8\Phi_0\,[0.065\Phi_{\rm ast}]$
3σ	$5.6\Phi_0\,[0.045\Phi_{\rm ast}]$	$11\Phi_0\,[0.089\Phi_{\rm ast}]$
4σ	$6.7\Phi_0\,[0.068\Phi_{\rm ast}]$	$14.3\Phi_0\,[0.12\Phi_{\rm ast}]$
5σ	$10.8\Phi_0\,[0.088\Phi_{\rm ast}]$	$17.3\Phi_0\,[0.14\Phi_{\rm ast}]$

Table 9.2: A summary of the discovery potential of the analysis, defined at 2σ, 3σ and 4σ confidence levels. The values of statistical power $1-\beta=0.5$ and $1-\beta=0.9$ derive from our definitions of sensitivity and discovery level in section 9.1.3 (see table 9.1.3).

9.3.2 Discovery Level

From the distributions plotted in figure 9.6 we define multiple discovery levels, with 2σ, 3σ and 4σ discoveries measured at a statistical power of $1-\beta=0.5$. The power curves for the fluxes displayed in the table are shown in figure 9.9. We obtain the discovery levels (2σ, 3σ, 4σ and 5σ) by reading off power curve intersections at $1-\beta=0.5$ for the respective α values. Alternatively we can take the y-axis projection for the given values of α to calculate the change of statistical power with flux for a given significance level. The evolution of statistical power with flux for a given significance are summarized in figure 9.10. The discovery levels are summarized in table 9.3.2, but our primary result, the 5σ discovery level is $E^2 d\Phi/dE = 10.8\times10^{-12}\,\mathrm{TeVcm^{-2}s^{-1}}$ (8.88 % of the flux). This corresponds to ~ 0.72 events per source or 2.7 events per bright source (the brightest 20 sources).

9.4 Discussion

We claim a sensitivity to $\Phi_{SB}=3.72\times10^{-12}\,\mathrm{TeVcm^{-2}s^{-1}}$ (3 % of the astrophysical flux), with any flux smaller regarded as indistinguishable from the background and a 5σ discovery level at $\Phi_{SB}=10.8\times10^{-12}\,\mathrm{TeVcm^{-2}s^{-1}}$ ($\sim 9\%$ of the flux).

To fully realize the implications of the analysis on star-formation driven models of neutrino production, the analysis would need to be applied to the "unblinded" data. Future unblinding of this analysis is intended at a later stage after approval is obtained from the IceCube colloboration (see chapter 10). However, for now let us discuss the implications of a possible null observation. A non-detection would place an upper limit on the flux of $\Phi_{SB}=3.72\times10^{-12}\,\mathrm{TeVcm^{-2}s^{-1}}$ or 3 % of the total astrophysical flux. Note that by construction this is the collective flux of the nearest starburst galaxies, represented by the catalogue of IRAS starburst galaxies (section 9.2.2). It was found in chapter 6 that the starbursts contained in the IRAS sample could account for up to 2% of the overall energy flux from starburst galaxies if starbursts were the dominant neutrino producers in the Universe. Even under this scenario this stacked point source analysis may not be able to measure a signal of any signficance. The bulk of the flux would originate from distant sources ($z\sim 2$) that likely cannot be resolved by our analysis. Additionally this value for the cumulative starburst neutrino flux was contingent on the assumption of hard spectral indices for neutrinos ($\Gamma\sim 2$) in starbursts and maximal hadronic production of starburst γ-ray emission. High energy γ-ray observations of the two nearest starburst galaxies, M82 and NGC 253, disfavour very hard spectral indices ($\Gamma_{\gamma,M82}\sim 2.25$). Moreover, leptonic γ-ray production in Pulsar Wind Nebulae could also explain the majority of starburst γ-ray emission [67]. The combination of these facts means that it is unlikely that the stacked point source analysis would be sensitive to a realistic starburst neutrino flux, as it is likely much smaller than the total astrophysical flux. However if this analysis were repeated using the four additional years of muon-neutrino data recorded as of the time of writing, the resulting improvement in sensitivity may increase the chances of measuring a starburst neutrino flux under the aforementioned optimistic assumptions.

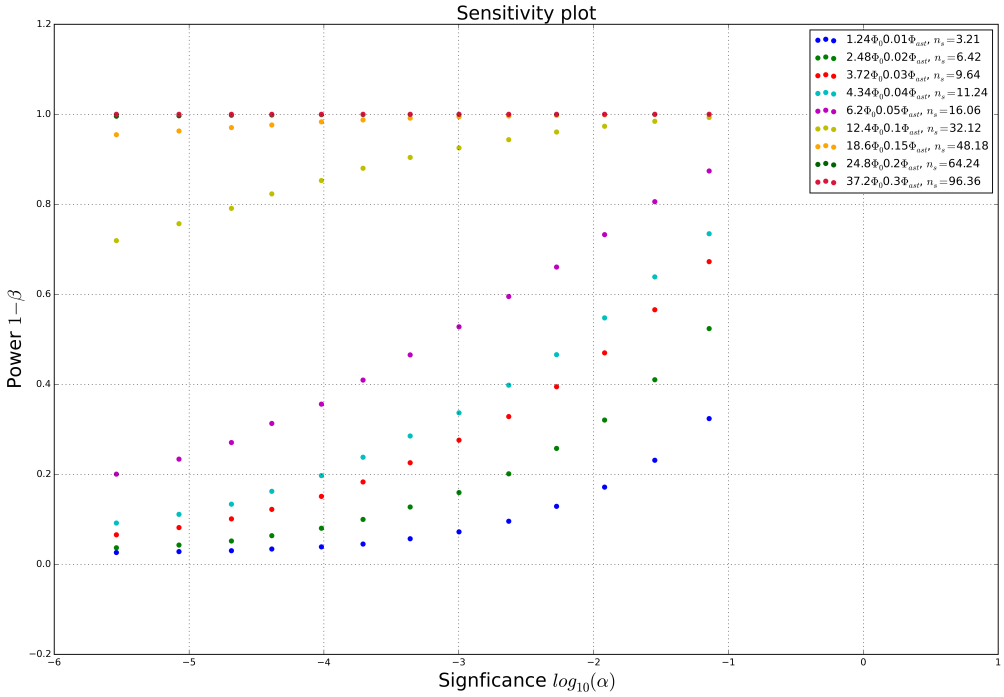

Figure 9.9: The power curves of the test-statistic distributions in linear scale from figure 9.6. Due to the linear scaling, the bulk of very small TS values ($TS \ll 1$) are merged into a single bin, making it impossible to measure $\alpha > 0.2$. However the linear-scaling allows for greater resolution for smaller values of α (< 0.1), hence we obtain discovery levels from the power curves displayed here. We find the 5σ discovery level by reading off the power curve that intersects $1-\beta = 0.5$ and $\alpha \sim 3\times10^{-7}$. The power curve corresponds to a flux of $E^2 d\Phi(E)/dE = 10.8\times10^{-12}$ TeVcm^{-2}s^{-1}.

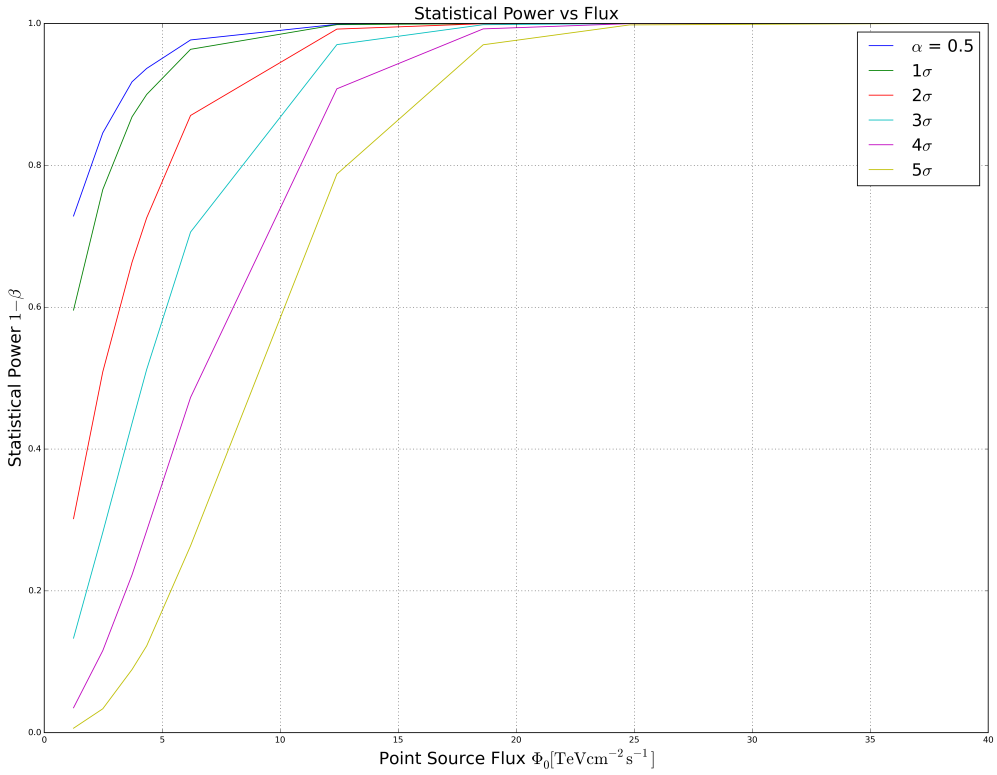

Figure 9.10: The statistical power versus flux for given discovery levels. We obtain this graph by taking a slice along the y-axis of figure 9.9 for a value of α corresponding to a significance level of 2σ, $3\,\sigma$, 4σ or $5\,\sigma$. Note that additional point source fluxes are represented here than thfigures 9.9 and 9.6. The discovery potential of our analysis is deduced from this graph, with a 5σ discovery found for a flux of $E^2 d\Phi(E)/dE = 10.3 \times 10^{-12}\,\mathrm{TeVcm}^{-2}\mathrm{s}^{-1}$ ($\sim 9\%$ of the astrophysical flux).

As noted previously, the flux per source rank follows an approximate power-law, with the brightest 20 sources dominating the overall flux. The brightest galaxy, M82, accounts for $\sim 18.6\%$ of the flux of the sample. By simply applying this fraction to the example flux upper-limit $\Phi_{SB,\mathrm{upper}} = 3.72\Phi_0$ we discuss the implications of starburst energetics (chapter 6).

Assuming a relative flux of $0.182\Phi_{SB,\mathrm{upper}}$, we calculate the luminosity L_{M82} of M82 to be:

$$L_{M82} = 4\pi D_{M82}^2 \Phi_{M82} = 4\pi D_{M82}^2 0.186 \Phi_{SB,\mathrm{upper}} \tag{9.19}$$

where $D_{M82} = 3.53 \pm 0.08$ Mpc and $\Phi_{M82} \leq 6.85 \times 10^{-13}\,\mathrm{TeVcm^{-2}s^{-1}}$. This flux value is similar to the upper limit obtained by a single point source search conducted at the position of M82[3]. Thus the upper-limit to M82's neutrino luminosity is $L_{M82} \lesssim 5.11 \times 10^{37}\,\mathrm{ergs^{-1}}$, around an order of magnitude lower ($L_\gamma \sim 10^{38}\,\mathrm{ergs^{-1}}$) [67] to approximately equal to the local γ-ray luminosity ($L_\gamma \sim 5 \times 10^{37}\,\mathrm{ergs^{-1}}$) [47]. Note however that the two results use different spectral indices $\Gamma_\nu = -2$ (assumed) and $\Gamma_\gamma = -2.25$ (measured up to $E_\gamma \sim 10\,\mathrm{TeV}$)[47]. A null detection of a neutrino flux would rule out exact equivalence between neutrinos and γ-rays in M82, as we would expect to observe a neutrino signal in that case. This would imply a predominantly leptonic mechanism for γ-ray emission in M82. In chapter 6 we found the accumulative neutrino flux of star-forming galaxies given the star-formation rate and luminosity per galaxy. This equation can also be used to calculate the average luminosity per starburst galaxy given knowledge of the flux.

$$\Phi_{\nu,SB} = \frac{c}{H_0 \Psi_0} \int_0^5 \frac{\Psi(z) f_{SB}(z) L_\nu(z)}{(1+z)^2 E(z)} dz \tag{9.20}$$

Using our upper limit, we find the average starburst luminosity to be $L_{SB} = 1.2 \times 10^{40}\mathrm{ergs^{-1}}$ around an order of magnitude higher than the average starburst luminosity estimated in chapter 6.

9.5 Summary

In this chapter we found the sensitivity of the stacked point source analysis of the northern sky IRAS Starburst sample using the 3 year up-going muon data. The analysis was found to have a sensitivity to a IRAS starburst signal component of 3% of the astrophysical flux $\Phi_{SB} = 3.72 \times 10^{-12}\,\mathrm{TeVcm^{-2}s^{-1}}$. We find 3σ, 4σ and 5σ discovery levels at 4.5 % , 6.8% and 8.8 % respectively. The sensitivity of the analysis falls slightly short being able to measure the cumulative emission of IRAS starbursts estimated in chapter 6.

Chapter 10

Conclusion

As shown in chapter 9, a stacked point source analysis of starburst galaxies would be sensitive to a cumulative energy flux of $E^2 d\Phi_{ptsrc}(E)/dE = 3.72 \times 10^{-12}\mathrm{GeVcm}^{-2}\mathrm{s}^{-1}$ (or around 3 % of the total astrophysical flux) from starburst galaxies in the IRAS bright galaxy catalogue. From our arguments in chapter 6 we find that this sensitivity level is near the energy flux from the IRAS starbursts, given hard spectral indices close to $\Gamma = 2$ and an assumed total hadronic origin for starburst γ-ray emission. Given the cosmic star-formation rate, the vast majority of the starburst neutrino emission would be distributed amongst distant sources around $z = 2$ that are too faint to realistically be resolved as point sources. Star-forming galaxies would have to produce the majority of the astrophysical neutrino flux for the stacking analysis to detect neutrino emission from the IRAS starburst sample. From chapter 6 we find that this condition itself is subject to two futher conditions:

1. The majority of γ-ray emission in starburst galaxies is produced by neutral pion decays from cosmic ray interactions.
2. The spectral index Γ of starburst neutrino galaxies would need to be close to $\Gamma = 2$.

Since TeV γ-ray observations of M82 and NGC 253 favour softer γ-ray spectral indices of $\Gamma = 2.3$ and the combined IceCube analysis further implies neutrino spectral indices near $\Gamma = 2.5$, it appears unlikely that starburst galaxies form the majority of the neutrino flux. Therefore a stacked point source analysis is unlikely to detect neutrino emission from starburst galaxies in the three year up-going muon sample. However increased event statistics from later event samples would improve this sensitivity.

Future Work

Many questions were left unexamined in the course of this thesis. We were limited to using only three years of up-going muon data when at least seven years have been made available as of the time of writing. Additionally, although the capabilities of the analysis were demonstrated we did not apply it to the real IceCube up-going muon data, which remains "blinded". Future extensions to the work presented in this thesis would include:

- Apply analysis to "unblinded" neutrino data to discover or find an upper-limit on the cumulative neutrino flux of nearby starburst galaxies.
- Measure the effect of the starbursts' neutrino spectral index Γ_{SB} on the sensitivity of the analysis. In the analysis we assumed $\Gamma = 2$.
- Calculate the sensitivity of the analysis using the full seven year up-going muon sample.
- Run analysis using larger catalogues of starburst galaxies obtained from Spizter and Herschel.

In summary starburst galaxies are not considered likely to produce the majority of the astrophysical neutrinos measured by IceCube based on our arguments in chapter 6. However we can not yet exclude starburst galaxies as being one amongst multiple classes of neutrino sources, perhaps including active galaxies and galactic sources. We also find that a stacked point source analysis is only likely to detect nearby starburst galaxies if starbursts do produce the majority of cosmic neutrino emission. This case is only plausible if the neutrino spectral index in starbursts is very close to $\Gamma \sim 2$ and the majority of their γ-ray emission is hadronic. Further investigation with additional years of neutrino data and larger catalogues of starburst galaxies may be able to confirm or rule out this possibility.

Appendices

Appendix A

Starburst Catalogue

Our sample of starburst galaxies used in the analysis in chapter 9 were selected from the IRAS Revised Bright Galaxy Sample (RBGS) an extensive all-sky catalogue of local bright infra-red galaxies. Represented in the sample are Seyfert galaxies, starburst galaxies and normal (or main-sequence) star-forming galaxies (see chapter 4 for descriptions of these galaxy types). To remove Seyfert galaxies we exploit the different spectral shape of Seyfert galaxies in the far infra-red which is expected to follow a power-law spectrum while starburst galaxies have a thermal spectrum [80] (see section 9.2.2 for a more detailed explanation). The shape of the infra-red spectrum is approximated using the ratio of $S_{12\mu\mathrm{m}}$ to $S_{25\mu\mathrm{m}}$ flux density and between $S_{25\mu\mathrm{m}}$ and $S_{60\mu\mathrm{m}}$. Normal star-forming galaxies are removed with a cut on the bolometric infra-red luminosity $L_{8-1000\mu\mathrm{m}}$, which is proportional to the local star-forming rate Ψ[52].

In summary we implement the following cuts on our source catalogue:

1. $\delta > -5°$: Removes southern sky objects from the catalogue
2. $4.43 < \frac{S_{25\mu m}}{S_{60\mu m}} < 9$: Removes Seyfert 1s and 2s
3. $L_{IR} \geq 5.8 \times 10^{10} L_{\odot}$: Selects for high star-formation rates

Our final list of starburst galaxies is summarized in the table included in this appendix and shown in the sky-map A.1.

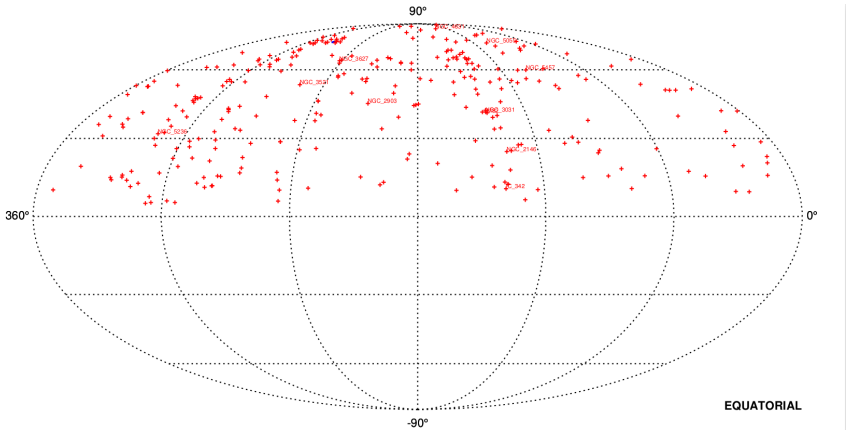

Figure A.1: Northern starburst galaxies from IRAS catalogue denoted with red crosses, the brightest 10 are labelled.

Identifier	α deg	δ deg	$S_{12\mu m}$ Jy	$S_{25\mu m}$ Jy	$S_{60\mu m}$ Jy	$S_{100\mu m}$ Jy	cz kms^{-1}	D Mpc	$\log \frac{L_{IR}}{L_\odot}$
M82	141.41	40.57	79.43	332.63	1480.42	1373.69	187	3.63	10.77
NGC 2146	135.65	24.9	6.83	18.81	146.69	194.05	885	16.47	11.07
NGC 3256	277.38	11.73	3.57	15.69	102.63	114.31	2781	35.35	11.56
NGC 3690	141.9	55.41	3.97	24.51	113.05	111.42	3159	47.74	11.88
NGC 4038/9	286.97	42.45	1.94	6.54	45.16	87.09	1563	21.54	10.84
NGC 6000	343.3	19.17	1.48	5.35	35.64	54.94	2173	28.9	10.97
NGC 4418	290.05	61.38	0.99	9.67	43.89	31.94	2104	31.9	11.08
NGC 2339	197.84	12.06	0.59	2.4	17.6	31.82	2206	32.1	10.76
NGC 5135	311.74	32.45	0.63	2.38	16.86	30.97	4114	52.15	11.17
NGC 3147	136.29	39.47	1.95	1.03	8.17	29.61	2756	41.41	10.91
MCG +12-02-001	123.13	10.22	0.78	3.51	21.92	29.11	4706	64.28	11.44
NGC 2276	127.67	27.71	1.07	1.63	14.29	28.97	2380	35.83	10.81
NGC 4793	101.57	88.05	1.08	1.57	12.42	28.11	2523	40.5	10.89
NGC 6240	20.73	27.29	0.59	3.55	22.94	26.49	7298	103.86	11.85
NGC 6574	42.15	15.41	0.91	1.73	14.57	26.03	2286	35.94	10.8
NGC 2633	139.68	33.87	0.92	2.47	15.98	25.43	2187	33.65	10.77
NGC 5427	333.28	52.55	1.29	1.48	10.24	25.29	2618	38.02	10.8
NGC 4194	134.39	61.76	0.99	4.51	23.2	25.16	2555	40.33	11.06
NGC 2388	185.05	21.97	0.69	1.98	16.74	24.58	4134	57.8	11.23
NGC 2342	196.2	13.04	0.46	1.64	7.73	24.1	5276	72.21	11.25
NGC 4433	292.84	54.13	0.63	1.52	13.35	23.83	2913	41.68	10.87
NGC 1961	143.82	19.47	0.9	0.99	7.17	23.37	3975	55.27	11.02
NGC 5653	49.6	68.11	0.64	1.37	10.57	23.03	3572	54.88	11.06
NGC 5394	73.25	72.5	0.59	1.4	9.38	22.02	3472	53.4	11
ESO 221	312.86	12.66	0.74	1.82	12.92	22	3028	58.21	11.17
NGC 5010	310.31	46.77	0.37	1.44	10.29	21.69	6400	94.33	11.5
NGC 5937	1.33	41.31	0.68	1.47	10.41	21.47	2807	42.45	10.83
NGC 5430	107.31	55.65	0.5	1.94	10.1	20.34	2960	45.63	10.88
NGC 6701	90.4	24.4	0.55	1.32	10.05	20.05	3933	56.64	11.05
NGC 5257	328.81	61.25	0.57	1.34	10.73	19.97	6798	98.63	11.55
IRAS F17138-1017	12.24	15.67	0.63	2.12	15.18	19.02	5197	75.84	11.42
NGC 3221	213.98	55.71	0.52	0.93	7.72	18.76	3971	58.68	11
NGC 5936	20.06	50.38	0.48	1.47	8.73	17.66	4013	60.81	11.07
NGC 5990	10.02	41.45	0.6	1.6	9.59	17.14	3863	58.42	11.06
NGC 3597	276.02	34.04	0.67	2.18	12.84	16.21	3485	48.31	10.97
ESO500-G034	264.5	28.14	0.38	1.43	10.46	16.01	3662	52.1	10.94
IRAS F16399-0937	7.89	22.98	0.27	1.13	8.42	14.72	8098	114.61	11.56
NGC 6670A	89.31	25.42	0.36	1.05	8.98	14.2	8684	118.38	11.6
NGC 3508	268.55	39.24	0.52	0.91	6.82	13.9	3889	56.26	10.9
IC 518A	326.12	13.98	0.36	1.53	8.07	13.65	4715	69.94	11.13
NGC 2415	184.14	23.98	0.61	1.19	8.75	13.58	3784	53.41	10.92

IRAS 12116-5615	297.81	5.96	0.35	1.12	9.78	12.95	8125	115.68	11.59
UGC 1041	60.52	26.02	0.51	0.69	5.84	12.78	4843	69.92	11.04
VV 250a	118.04	54.77	0.35	1.95	11.39	12.41	9313	127.99	11.74
IC 280	314.9	37.7	0.38	0.68	6.1	12.36	4930	74.67	11.08
ESO 264-G057	282.21	14.86	0.34	0.81	5.69	12.16	5156	75.74	11.08
NGC 6621	98.47	28.6	0.31	0.97	6.78	12.01	6234	86.42	11.23
NGC 5433	56.45	73.67	0.27	0.85	6.31	11.67	4352	65.3	10.95
UGC˙3608	170.23	20.28	0.41	1.2	8.05	11.33	6538	88.51	11.3
CGCG 052-037	19.27	32.9	0.25	0.81	7	11.23	7342	104.72	11.38
ESO 267-G030	296.4	15.17	0.35	0.66	5.61	11.06	5543	88.67	11.19
NGC 6786	104.72	24.54	0.43	1.42	7.58	10.77	7533	102.69	11.43
UGC 02865	135.2	14.58	0.23	0.66	5.6	10.73	4312	59.3	10.81
ESO 323-G077	306.02	22.37	0.68	1.24	5.73	10.73	4477	58.21	10.91
NGC 6052	35.31	45.47	0.28	0.83	6.79	10.57	4747	70.42	11.02
ESO 386-G019	326.74	19.83	0.31	0.79	5.99	10.36	4476	64	10.91
MCG 07-23-019	174.19	63.99	0.2	0.71	6.38	10.3	10438	143.21	11.61
NGC 5256	102.72	66.97	0.32	1.07	7.25	10.11	8285	115.83	11.49
VII Zw 031	133.18	22.61	0.2	0.62	5.51	10.09	16260	214.83	11.94
VV 705	70.35	56.49	0.29	1.42	9.02	10	12336	168.72	11.89
MCG-02-33-098/9	306.78	47.02	0.34	1.63	7.49	9.68	4861	72.5	11.11
ESO 319-G022	286.61	18.59	0.16	0.95	7.68	9.52	4902	72.26	11.04
NGC 6090	81.39	45.21	0.26	1.24	6.48	9.41	8865	122.55	11.51
ES0 432-IG006	253.92	6.83	0.58	0.84	6.48	9.31	4846	68.55	11.02
CGCG˙011-076	263.57	52.85	0.48	0.76	5.85	9.18	7464	106.27	11.37
IRAS F02572+7002	133.61	10.13	0.31	0.82	5.62	9.09	4886	66.34	10.91
IC 2545	267.84	17.49	0.28	1.21	9.79	9.02	10267	141.58	11.73
CGCG 247-020	91.29	62.12	0.15	0.84	6.01	8.47	7666	107.71	11.32
MCG +08-18-013	169.79	46.96	0.1	0.75	5.68	8.42	7777	107.06	11.28
IRAS 03582+6012	144.54	5.75	0.14	0.7	5.65	7.76	8997	119.05	11.37
IRAS 05129+5128	158.04	7.76	0.21	1.05	6.56	7.34	8224	109.16	11.36
IRAS F08339+6517	150.45	35.6	0.25	1.13	5.81	6.48	5730	79.33	11.05
IRAS F15250+3608	57.81	55.94	0.16	1.31	7.1	5.93	16535	223.49	12.02
ES0 221-IG008	312.97	13.44	0.3	1.12	5.64	5.52	3190	58.21	10.77

ES0 G005	452-	351	13.58	1.03	1.18	6.44	0	4175	61.25	10.9

Appendix B

Cross Checks to Stacking Analysis

In chapter 9 we measure the sensitivity and discovery potential of a stacked point source analysis to a selected catalogue of starburst galaxies. In addition to examining the sensitivity to the catalogue of starburst galaxies (see section 9.2.2 in chapter 9 and Appendix A), we examine the effect that our choice of galaxies would have on the analysis sensitivity. The neutrino flux expected per galaxy is weighted according to its intensity at 100 microns. Using this hypothesis we would expect that the majority of the neutrino flux should cluster around the brightest twenty galaxies, thereby the analysis would be more sensitive to the minority of bright galaxies. To establish the robustness of the analysis we require that as we increase the number of sources: N_{src}, the results will become indistinguishable from a diffuse analysis, while as $N_{src} \to 1$ we expect the results to appear identical to that of a single point source search. We therefore apply the following tests to the analysis:

1. Perform the analysis on the uncut IRAS sample (maximal source numbers)
2. Remove the brightest 20 galaxies from the sample
3. Remove all but the brightest 20 galaxies from the sample
4. Apply the analysis to $N_{src} = 1$ under multiple declinations of the source

The results are displayed in figure B.1. The values are shown in unit values of the point source flux $E^2 d\Phi_0/dE$ and as a fraction of the astrophysical diffuse flux, where in the former is:

$$\hat{\Phi}_0 = E^2 \frac{d\Phi_0}{dE} = 10^{-12}\,\mathrm{TeVcm^{-2}s^{-1}} \tag{B.1}$$

while the latter is:

$$\hat{\Phi}_{ast} = E^2 \Phi_{ast} \sim 10^{-8}\,\mathrm{GeVcm^{-2}s^{-1}sr^{-1}} \tag{B.2}$$

Sensitivity is defined using a significance of $\alpha = 0.5$ and statistical power $1 - \beta = 0.9$ while the discovery levels are defined using 4σ, 5σ at statistical powers of $1 - \beta = 0.5$.

B.1 Cross Checks

The procedure for calculating the analysis sensitivity and discovery potential is outlined in chapter 9. Here we examine the effect of the choice of which sources to include in the analysis. In each case, we generate ensembles of simulated neutrino skies under a background-only hypothesis and various signal hypotheses using the procedure outlined in chapter 8. Using the stacked point source likelihood function (see 9) we calculate the best fit signal number n_s and its associated likelihood ratio, our test statistic, for each sky in the ensemble. The distributions of test-statistics for the background and signal hypotheses are then integrated to calculate the distribution of significance α (see equation B.3) and statistical power $1 - \beta$ (see equation B.4) for different signal

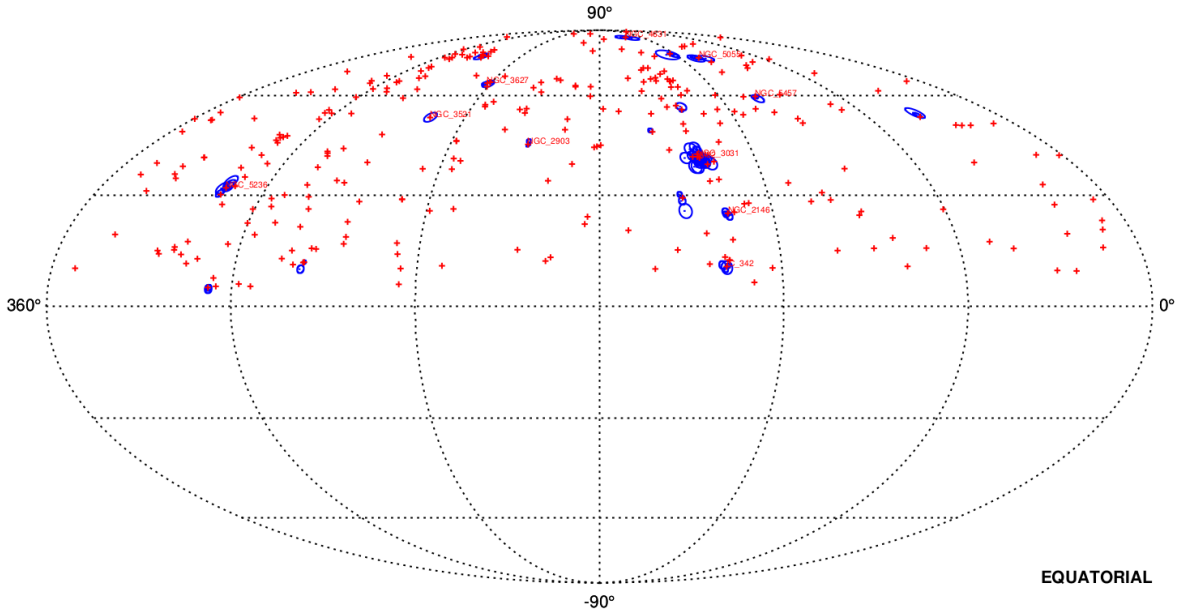

Figure B.1: Example sky-map, 100 events sampled from 300 sources. Events indicated with blue circles with radii equal to their median angular resolution.

hypotheses. We call change of power with significance for a given flux value the "power curve". By reading off the power curve that intersects $\alpha = 0.5$ and $1 - \beta$ we find the sensitivity of the analysis. A similar procedure is followed to obtain different discovery levels. However in this case, the shape of the distributions, with large fractions of very small test statistics, mean that it was difficult to measure $\alpha > 0.1$ without plotting test-statistic distributions in log-scale. Since this section is only meant to illustrate the effect of the choice of source catalogue, we elected to measure the change in 2σ and 4σ discovery levels between the different catalogues.

$$\alpha = \int_{X_{exp}}^{\infty} P(X, \theta_0) dX = \int_{X_{exp}}^{\infty} P(X, n_s = 0) dX \tag{B.3}$$

$$\beta = \int_{0}^{X_{exp}} P(X, \theta_s) dX \rightarrow 1 - \beta = \int_{X_{exp}}^{\infty} P(X, \theta_s) dX = \int_{X_{exp}}^{\infty} P(X, n_s = \bar{n}_s, \Gamma = \bar{\Gamma}) dX \tag{B.4}$$

B.1.1 300 Sources

We examine the sensitivity of the stacked analysis to all objects from the IRAS Revised Bright Galactic Sample in the northern sky, including 300 starburst galaxies, Seyfert galaxies and normal star-forming galaxies. A sky-map showing 100 signal events drawn from 300 sources is shown in figure B.1 with clear clustering around the brightest 20 sources. The test-statistic distribution and sensitivity plots are shown in figures B.2 and B.3 respectively. See table B.1 for the sensitivity and discovery potential. With the clustering of events around the brightest 20 sources, we create two additional catalogues, one with the brightest 20 sources only (section B.1.2) and one with the brightest 20 removed (section B.1.3), leaving 280 sources.

B.1.2 20 Brightest Sources

We remove all but the brightest 20 galaxies and repeat the stacked point source analysis. With fewer sources, the 20 galaxies have more events associated with them on average for the same given flux strength. We expect a smaller number of bright sources to be more easily distinguished from the diffuse background. This expectation is reflected in the increased sensitivity (see figures

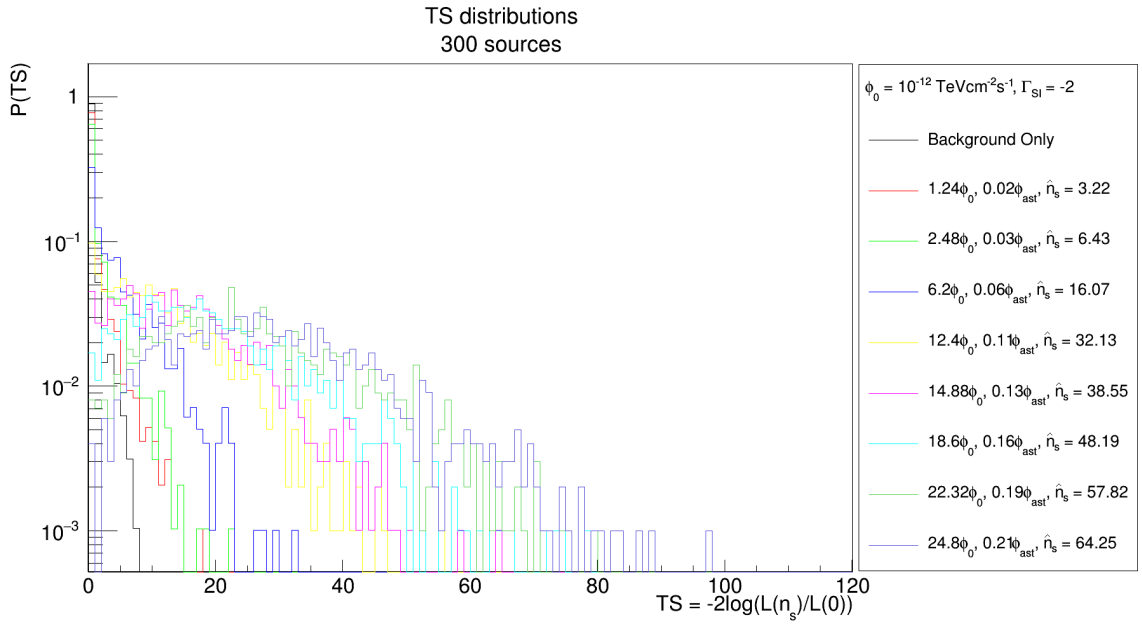

Figure B.2: Our distribution of test-statistics from a the background hypothesis (in black, far left) and a set of progressively stronger signal hypotheses (in colours increasing towards to right).

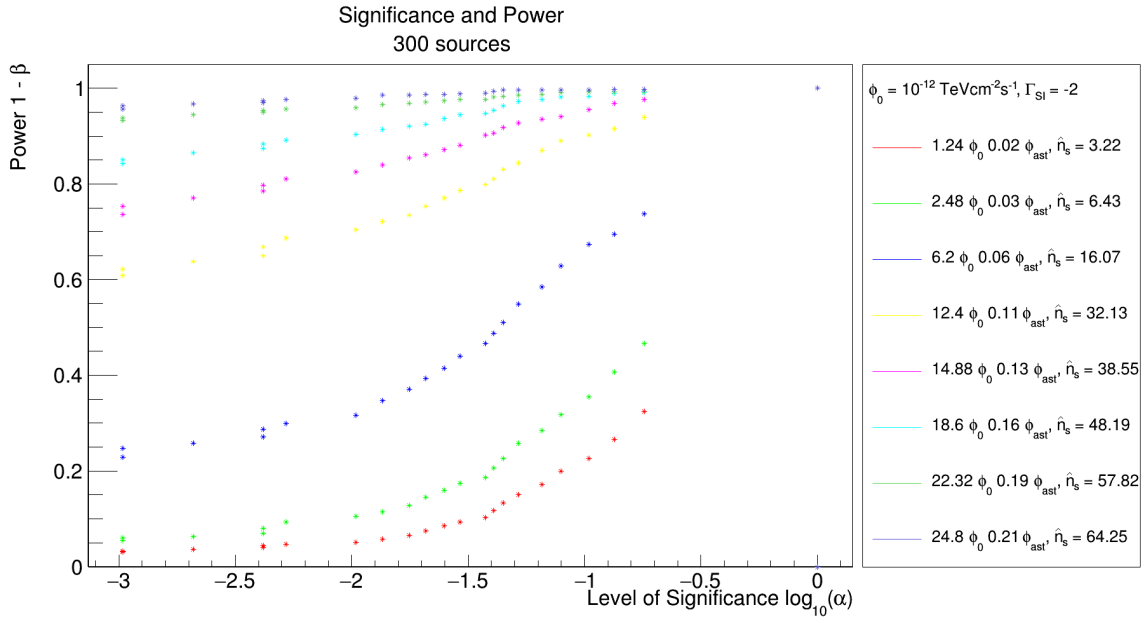

Figure B.3: The power curves obtained for the 300 source catalogue. We find the 2σ and 4σ discovery levels at $6\Phi_0$ (6 % of the astrophysical)and $21\Phi_0$ (18 %) respectively. This implies a lowering of sensitivity to overall neutrino flux.

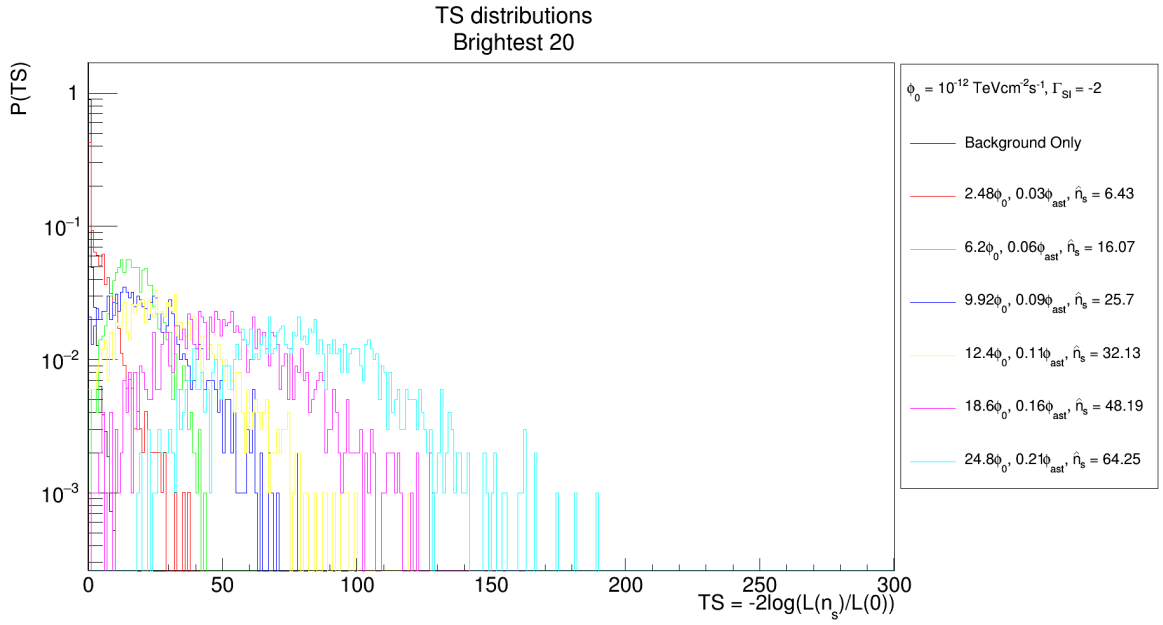

Figure B.4: The test statistic distributions for the brightest 20 sources. Note the higher level of overlap between the background and signal hypotheses. This already implies an increase in analysis sensitivity.

Label	N_{srcs}	Sensitivity (2σ) $\hat{\Phi}_0[\hat{\Phi_{ast}}]$	Discovery (4σ) $\hat{\Phi}_0[\hat{\Phi_{ast}}]$
Uncut catalogue	300	6 [0.06]	21 [0.18]
Top 20	20	1.5 [0.02]	12.5 [0.11]
Bottom 280	280	8 [0.08]	
Singe Source	1	1 [0.01]	7 [0.07]
Starburst Only	75	3 [0.03]	14.3 [0.12]

Table B.1: Summary of the sensitivity and discovery potentials of the analysis to the different source catalogues

B.4 and B.5) to lower fluxes, with $1.5\Phi_0$ measured at 2σ confidence with a statistical power of $1 - \beta = 0.5$, a two fold increase from the results in chapter 9.

B.1.3 280 Dimmer Sources

Alternatively we can remove the brightest 20 sources, leaving 280 sources that are individually weaker in individual flux. The same number of signal events will be spread more evenly over more sources, which will appear closer to a diffuse flux than in the case of section B.1.1. Indeed we find that the sensitivity reduces compared to the results for chapter 9. For the dimmer 280 sources we find the analysis sensitive to a flux of $8\Phi_0$ a 2.5 fold decrease from chapter 9 (see figures B.6 and B.7).

B.1.4 Single Source

To test the robustness of the analysis we also test the sensitivity to a single source. In this case we use the position of the brightest starburst galaxy in the northern sky, M82 (at a declination of $\delta = 69°$) to define the position of the single source. We find the sensitivity increases compared to the catalogue of the brightest 20 galaxies (section B.1.1), with the analysis being able to distinguish $1\Phi_0$ at 2σ at 50 % statistical power (see figures B.8 and B.9).

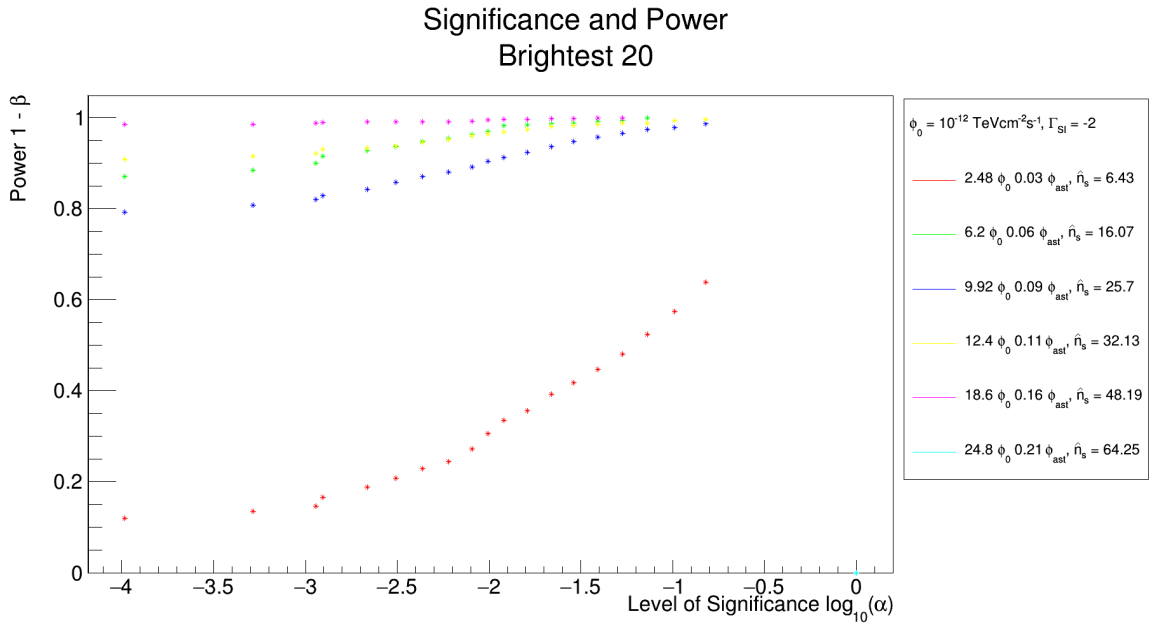

Figure B.5: Sensitivity increases for the brightest 20 sources as indicated by the shape of the power curves. We can read off the 2σ and 4σ discovery levels at $1.5\Phi_0$ and $12.5\Phi_0$ respectively.

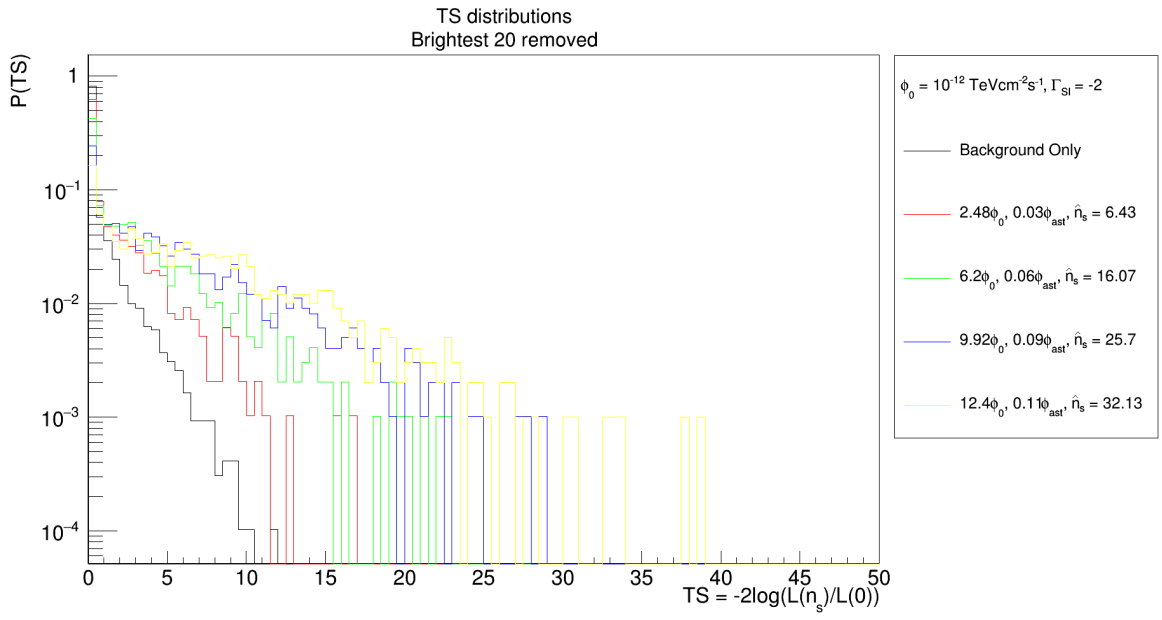

Figure B.6: The test-statistic distribution for the catalogue with the brightest 20 galaxies removed. The 280 remaining sources are more equitably distributed in flux (and hence weight), resulting in a more evenly spread flux that more closely resembles the diffuse flux. This increase offset between different signal hypotheses and lower level of overlap implies a drop in sensitivity.

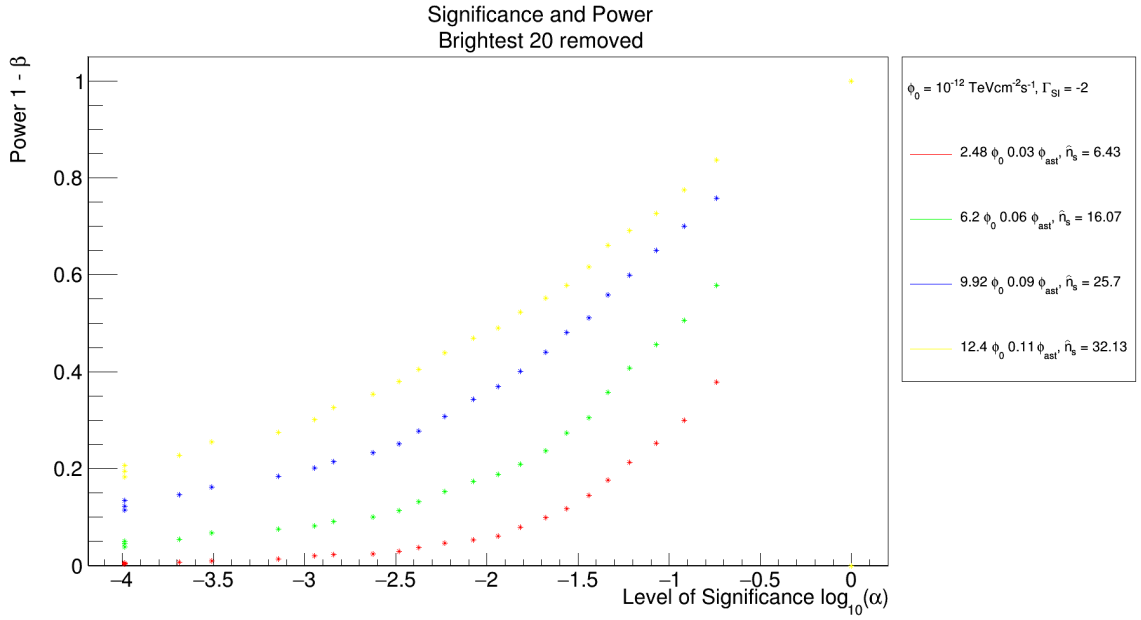

Figure B.7: The shape of the power curves indicate a drop in sensitivity when the brightest 20 sources are removed. We find a 2σ discovery level at $8\Phi_0$, a significant increase from the 2σ level obtained in the analysis in chapter 9.

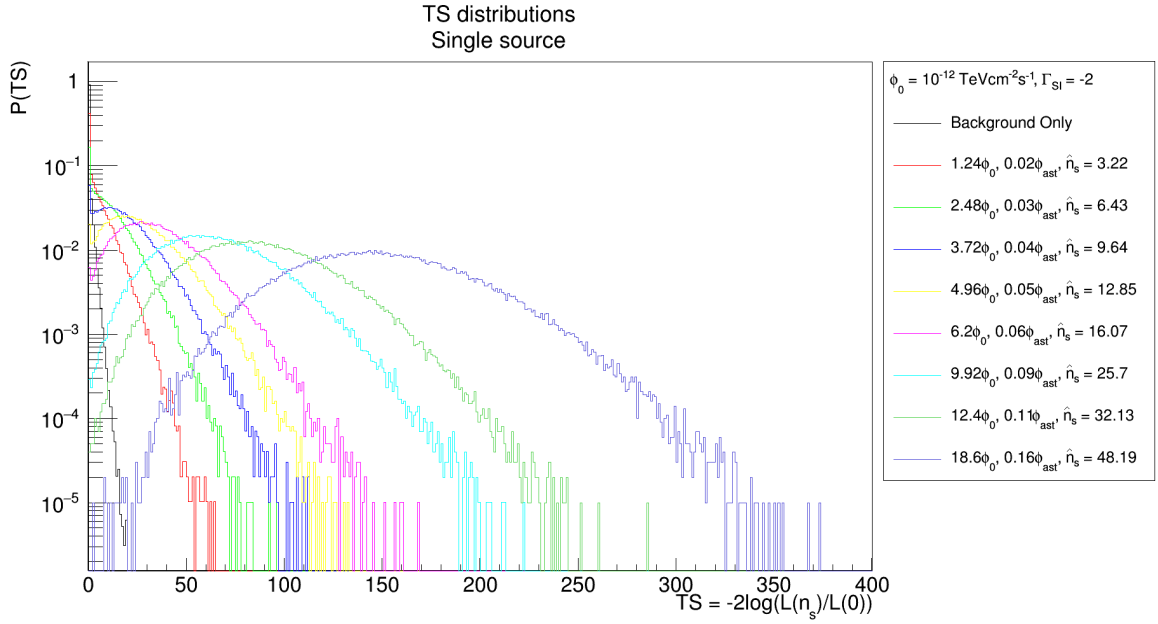

Figure B.8: The test-statistic distribution for a single source. In this case we examine a source at M82. As we only needed to generate signal events from one source, we could easily produce large numbers of skies with 10^7 represented for the background and signal hypotheses each.

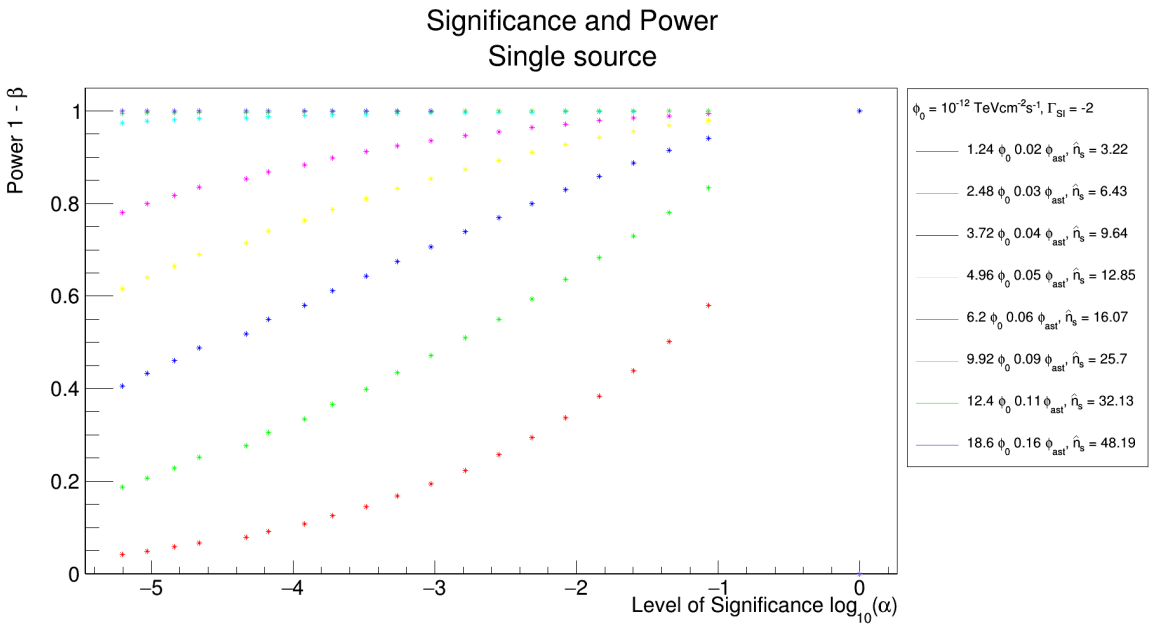

Figure B.9: The power curves obtained for different fluxes drawn from M82. We read off a 2σ discovery level at $1\Phi_0$ and the 4σ level at $7\Phi_0$.

B.2 Summary

See table B.1 for a summary of the change in analysis sensitivity with the number of catalogue sources analysed. We find that, in agreement with our expectations, the sensitivity decreases for larger numbers of sources tested. However it is interesting to note that while overall sensitivity decreases for large N_{src}, the flux per source that the analysis is sensitive to increases. For example, while we claim a 2σ discovery level at $3\Phi_0$ for the starburst catalogue in chapter 9 and $1\Phi_0$ for a single point source, this translates to an average flux $0.04\Phi_0$ per source in the former case, or $0.15\Phi_0$ per one of the brightest 20 sources. Although the sources weights are distributed unevenly, the point remains that sensitivity *per source* increases even if overall sensitivity decreases. Indeed figure B.10 shows that for sources of equal weight the flux per source that the analysis is sensitive to decreases for larger values of N_{src}. Further investigation into this effect may be merited.

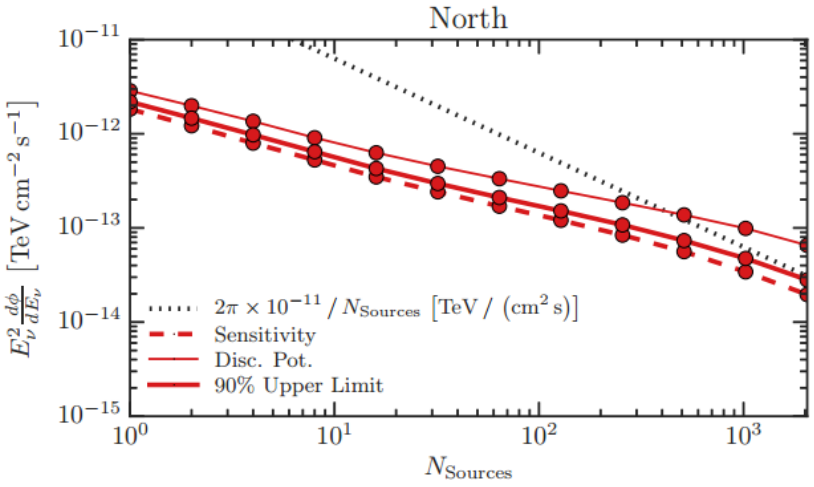

Figure B.10: The sensitivity, discovery potential and 90 % upper limit in the northern sky for uniformly distributed sources under a power law of $\Gamma = 2$. The flux is shown per source for an increasing number of isotropically distributed sources. The black dashed line shows the value per source when the astrophysical neutrino flux is evenly divided among the sources [4].

Bibliography

[1] A. Aab, P. Abreu, M. Aglietta, E. J. Ahn, I. Al Samarai, I. F. M. Albuquerque, I. Allekotte, P. Allison, A. Almela, and J. et al. Alvarez Castillo. Improved limit to the diffuse flux of ultrahigh energy neutrinos from the Pierre Auger Observatory. Phys. Rev. D, 91(9):092008, May 2015.

[2] R. Aaij, B. Adeva, M. Adinolfi, A. Affolder, Z. Ajaltouni, S. Akar, J. Albrecht, F. Alessio, M. Alexander, S. Ali, and et al. Observation of J $/\psi$ p Resonances Consistent with Pentaquark States in $\Lambda_b^0 \to J/\psi K^-$p Decays. *Physical Review Letters*, 115(7):072001, August 2015.

[3] M. G. Aartsen, K. Abraham, M. Ackermann, J. Adams, J. A. Aguilar, M. Ahlers, M. Ahrens, D. Altmann, K. Andeen, T. Anderson, and et al. All-sky Search for Time-integrated Neutrino Emission from Astrophysical Sources with 7 yr of IceCube Data. *The Astrophysical Journal*, 835:151, February 2017.

[4] M. G. Aartsen, K. Abraham, M. Ackermann, J. Adams, J. A. Aguilar, M. Ahlers, M. Ahrens, D. Altmann, K. Andeen, T. Anderson, and et al. All-sky Search for Time-integrated Neutrino Emission from Astrophysical Sources with 7 yr of IceCube Data. *The Astrophysical Journal*, 835:151, February 2017.

[5] M. G. Aartsen, K. Abraham, M. Ackermann, J. Adams, J. A. Aguilar, M. Ahlers, M. Ahrens, D. Altmann, K. Andeen, T. Anderson, and et al. The Contribution of Fermi-2LAC Blazars to Diffuse TeV-PeV Neutrino Flux. *The Astrophysical Journal*, 835:45, January 2017.

[6] M. G. Aartsen, K. Abraham, M. Ackermann, J. Adams, J. A. Aguilar, M. Ahlers, M. Ahrens, D. Altmann, T. Anderson, M. Archinger, and et al. Evidence for Astrophysical Muon Neutrinos from the Northern Sky with IceCube. *Physical Review Letters*, 115(8):081102, August 2015.

[7] M. G. Aartsen, M. Ackermann, J. Adams, J. A. Aguilar, M. Ahlers, M. Ahrens, D. Altmann, K. Andeen, T. Anderson, I. Ansseau, and et al. The IceCube Neutrino Observatory: instrumentation and online systems. *Journal of Instrumentation*, 12:P03012, March 2017.

[8] M. G. Aartsen, M. Ackermann, J. Adams, J. A. Aguilar, M. Ahlers, M. Ahrens, D. Altmann, T. Anderson, C. Arguelles, T. C. Arlen, and et al. Observation of High-Energy Astrophysical Neutrinos in Three Years of IceCube Data. *Physical Review Letters*, 113(10):101101, September 2014.

[9] M. G. Aartsen, M. Ackermann, J. Adams, J. A. Aguilar, M. Ahlers, M. Ahrens, D. Altmann, T. Anderson, C. Arguelles, T. C. Arlen, and et al. Observation of High-Energy Astrophysical Neutrinos in Three Years of IceCube Data. *Physical Review Letters*, 113(10):101101, September 2014.

[10] M. G. Aartsen, M. Ackermann, J. Adams, J. A. Aguilar, M. Ahlers, M. Ahrens, D. Altmann, T. Anderson, C. Arguelles, T. C. Arlen, and et al. Atmospheric and astrophysical neutrinos above 1 TeV interacting in IceCube. Phys. Rev. D, 91(2):022001, January 2015.

[11] M. G. Aartsen, G. C. Hill, A. Kyriacou, S. Robertson, A. Wallace, B. J. Whelan, M. Ackermann, E. Bernardini, S. Blot, F. Bradascio, and et al. Measurement of the multi-TeV neutrino interaction cross-section with IceCube using Earth absorption. Nature, 551:596–600, November 2017.

[12] R. Abbasi, Y. Abdou, T. Abu-Zayyad, M. Ackermann, J. Adams, J. A. Aguilar, M. Ahlers, M. M. Allen, D. Altmann, K. Andeen, and et al. The design and performance of IceCube DeepCore. *Astroparticle Physics*, 35:615–624, May 2012.

[13] F. Acero, M. Ackermann, M. Ajello, A. Albert, W. B. Atwood, M. Axelsson, L. Baldini, J. Ballet, G. Barbiellini, and et al. Bastieri. Fermi Large Area Telescope Third Source Catalog. ApJS, 218:23, June 2015.

[14] M. Ackermann, M. Ajello, A. Allafort, L. Baldini, J. Ballet, D. Bastieri, K. Bechtol, R. Bellazzini, B. Berenji, E. D. Bloom, and et al. GeV Observations of Star-forming Galaxies with the Fermi Large Area Telescope. *The Astrophysical Journal*, 755:164, August 2012.

[15] L. Alfredo Anchordoqui. Ultrahigh Energy Cosmic Rays: Facts, Myths, and Legends. *ArXiv e-prints*, April 2011.

[16] J. J. Beatty, J. Matthews, and Wakely S. P. *Particle Physics Review D.*, chapter 27. Cosmic Rays. 2015.

[17] K. Bechtol, M. Ahlers, M. Di Mauro, M. Ajello, and J. Vandenbroucke. Evidence against Star-forming Galaxies as the Dominant Source of Icecube Neutrinos. *The Astrophysical Journal*, 836:47, February 2017.

[18] J. Becker Tjus, B. Eichmann, M. Kroll, and N. Nierstenhöfer. Gamma-ray emitting supernova remnants as the origin of Galactic cosmic rays? *Astroparticle Physics*, 81:1–11, August 2016.

[19] A. Bhattacharya, R. Gandhi, W. Rodejohann, and A. Watanabe. The Glashow resonance at IceCube: signatures, event rates and pp vs. pγ interactions. J. Cosmology Astropart. Phys., 10:017, October 2011.

[20] G. R. Blumenthal and R. J. Gould. Bremsstrahlung, Synchrotron Radiation, and Compton Scattering of High-Energy Electrons Traversing Dilute Gases. *Reviews of Modern Physics*, 42:237–271, 1970.

[21] NASA Goddard Space Flight Centre. Exploring active galactic nuclei, 2016.

[22] J. de Mello Neto and Pierre Auger Collaboration. Anisotropy studies with the Pierre Auger Observatory. In *Journal of Physics Conference Series*, volume 409 of *Journal of Physics Conference Series*, page 012108, February 2013.

[23] P. B. Denton and I. Tamborra. Exploring the Properties of Choked Gamma-Ray Bursts with IceCube's High Energy Neutrinos. *ArXiv e-prints*, November 2017.

[24] K. Emig, C. Lunardini, and R. Windhorst. Do high energy astrophysical neutrinos trace star formation? J. Cosmology Astropart. Phys., 12:029, December 2015.

[25] A. Faessler, R. Hodak, S. Kovalenko, and F. Simkovic. Search for the Cosmic Neutrino Background and KATRIN. *ArXiv e-prints*, April 2013.

[26] A. Faessler, R. Hodak, S. Kovalenko, and F. Simkovic. Search for the Cosmic Neutrino Background. In *Journal of Physics Conference Series*, volume 580 of *Journal of Physics Conference Series*, page 012040, February 2015.

[27] H. Fleischhack and for the VERITAS collaboration. Upper limits on the VHE γ-ray flux from the ULIRG Arp 220 and other galaxies with VERITAS. *ArXiv e-prints*, August 2015.

[28] J. A. Formaggio and G. P. Zeller. From eV to EeV: Neutrino cross sections across energy scales. *Reviews of Modern Physics*, 84:1307–1341, July 2012.

[29] L. Fullmer and C. J. Londsdale. *Cataloged galaxies and quasars observed in the IRAS survey.* 1989.

[30] T. Gaisser. *Cosmic Rays and Particle Physics.* Cambdrige University Press, 1990.

[31] J. García-González, A. Alonso-Herrero, A. Hernán-Caballero, M. Pereira-Santaella, C. Ramos-Almeida, J. A. Acosta-Pulido, T. Díaz-Santos, P. Esquej, O. González-Martín, K. Ichikawa, E. López-Rodríguez, M. Povic, P. F. Roche, and M. Sánchez-Portal. The nuclear and integrated far-infrared emission of nearby Seyfert galaxies. MNRAS, 458:4512–4529, June 2016.

[32] R. Gauld, J. Rojo, L. Rottoli, S. Sarkar, and J. Talbert. The prompt atmospheric neutrino flux in the light of LHCb. *Journal of High Energy Physics*, 2:130, February 2016.

[33] S. L. Glashow. Resonant Scattering of Antineutrinos. *Physical Review*, 118:316–317, April 1960.

[34] Jeremy J. Gray. Olinde rodrigues' paper of 1840 on transformation groups. *Archive for History of Exact Sciences*, 21(4):375–385, 1980.

[35] Kenneth Greisen. End to the cosmic-ray spectrum? *Phys. Rev. Lett.*, 16:748–750, Apr 1966.

[36] Claus Grupen. *Astroparticle Physics.* Springer, Berlin, Heidelberg, 2005.

[37] K. Hanson and O. Tarasova. Design and production of the IceCube digital optical module. *Nuclear Instruments and Methods in Physics Research A*, 567:214–217, November 2006.

[38] A. Heger, C. L. Fryer, S. E. Woosley, N. Langer, and D. H. Hartmann. How Massive Single Stars End Their Life. *The Astrophysical Journal*, 591:288–300, July 2003.

[39] A. M. Hillas. The Origin of Ultra-High-Energy Cosmic Rays. ARA&A, 22:425–444, 1984.

[40] HiRes Collaboration, R. U. Abbasi, T. Abu-Zayyad, M. Allen, and et al. Amman. First Observation of the Greisen-Zatsepin-Kuzmin Suppression. *Physical Review Letters*, 100(10):101101, March 2008.

[41] IceCube Collaboration. Evidence for High-Energy Extraterrestrial Neutrinos at the IceCube Detector. *Science*, 342:1242856, November 2013.

[42] IceCube Collaboration. Evidence for High-Energy Extraterrestrial Neutrinos at the IceCube Detector. *Science*, 342:1242856, November 2013.

[43] IceCube Collaboration, M. G. Aartsen, M. Ackermann, J. Adams, J. A. Aguilar, M. Ahlers, M. Ahrens, I. A. Samarai, D. Altmann, K. Andeen, and et al. Neutrinos and Cosmic Rays Observed by IceCube. *ArXiv e-prints*, January 2017.

[44] IceCube Collaboration, R. Abbasi, Y. Abdou, M. Ackermann, J. Adams, J. A. Aguilar, M. Ahlers, D. Altmann, K. Andeen, J. Auffenberg, and et al. IceTop: The surface component of IceCube. *ArXiv e-prints*, July 2012.

[45] IceCube Collaboration, A. Achterberg, M. Ackermann, J. Adams, J. Ahrens, K. Andeen, D. W. Atlee, J. Baccus, J. N. Bahcall, X. Bai, and et al. First year performance of the IceCube neutrino telescope. *Astroparticle Physics*, 26:155–173, October 2006.

[46] IceCube-Gen2 Collaboration, :, M. G. Aartsen, M. Ackermann, J. Adams, J. A. Aguilar, M. Ahlers, M. Ahrens, D. Altmann, T. Anderson, and et al. IceCube-Gen2: A Vision for the Future of Neutrino Astronomy in Antarctica. *ArXiv e-prints*, December 2014.

[47] Y. Inoue. High Energy Gamma-ray Absorption and Cascade Emission in Nearby Starburst Galaxies. *The Astrophysical Journal*, 728:11, February 2011.

[48] H.-T. Janka. Explosion Mechanisms of Core-Collapse Supernovae. *Annual Review of Nuclear and Particle Science*, 62:407–451, November 2012.

[49] U. F. Katz and C. Spiering. High-energy neutrino astrophysics: Status and perspectives. *Progress in Particle and Nuclear Physics*, 67:651–704, July 2012.

[50] R. C. Kennicutt, Jr. The Global Schmidt Law in Star-forming Galaxies. *The Astrophysical Journal*, 498:541–552, May 1998.

[51] S. S. Kimura, K. Murase, P. Mészáros, and K. Kiuchi. High-energy Neutrino Emission from Short Gamma-Ray Bursts: Prospects for Coincident Detection with Gravitational Waves. ApJ, 848:L4, October 2017.

[52] L. Köpke and IceCube Collaboration. Supernova Neutrino Detection with IceCube. In *Journal of Physics Conference Series*, volume 309 of *Journal of Physics Conference Series*, page 012029, August 2011.

[53] M. Kowalski. Status of High-Energy Neutrino Astronomy. In *Journal of Physics Conference Series*, volume 632 of *Journal of Physics Conference Series*, page 012039, August 2015.

[54] D. Kuempel. Search for ultra-high energy photons with the Pierre Auger observatory. In *6th International Symposium on High Energy Gamma-Ray Astronomy*, volume 1792 of *American Institute of Physics Conference Series*, page 070012, January 2017.

[55] D. Kuempel and for the Pierre Auger Collaboration. Search for Ultra-High Energy Photons with the Pierre Auger Observatory. *ArXiv e-prints*, November 2016.

[56] B. C. Lacki, T. A. Thompson, E. Quataert, A. Loeb, and E. Waxman. On the GeV and TeV Detections of the Starburst Galaxies M82 and NGC 253. *The Astrophysical Journal*, 734:107, June 2011.

[57] A. Lamastra, N. Menci, F. Fiore, and P. Santini. The interaction-driven starburst contribution to the cosmic star formation rate density. A&A, 552:A44, April 2013.

[58] M. Lemoine and G. Sigl. Physics and astrophysics of ultra-high-energy cosmic rays, springer lecture notes in physics, 2001.

[59] T. Linden. Star-forming galaxies significantly contribute to the isotropic gamma-ray background. Phys. Rev. D, 96(8):083001, October 2017.

[60] L. Lyons. Discovering the Significance of 5 sigma. *ArXiv e-prints*, October 2013.

[61] P. Madau and M. Dickinson. Cosmic Star-Formation History. ARA&A, 52:415–486, August 2014.

[62] J. Matthews. A Heitler model of extensive air showers. *Astroparticle Physics*, 22:387–397, January 2005.

[63] S. Mertens. Direct Neutrino Mass Experiments. In *Journal of Physics Conference Series*, volume 718 of *Journal of Physics Conference Series*, page 022013, May 2016.

[64] K. Murase and E. Waxman. Constraining high-energy cosmic neutrino sources: Implications and prospects. Phys. Rev. D, 94(10):103006, November 2016.

[65] P. L. Nolan, A. A. Abdo, M. Ackermann, M. Ajello, A. Allafort, E. Antolini, W. B. Atwood, M. Axelsson, L. Baldini, J. Ballet, and et al. Fermi Large Area Telescope Second Source Catalog. ApJS, 199:31, April 2012.

[66] University of Wisconsin-Madison Physical Sciences Lab. Digital optical modules, 2017.

[67] S. Ohm. Starburst galaxies as seen by gamma-ray telescopes. *Comptes Rendus Physique*, 17:585–593, June 2016.

[68] S. Palomares-Ruiz, O. Mena, and A. C. Vincent. On the flavor composition of the high-energy neutrinos in IceCube. *ArXiv e-prints*, November 2014.

[69] W. Pauli. Open letter to the group of radioactive people at the gauverein meeting in tbingen. 1930.

[70] Pierre Auger Collaboration. Measurement of the cosmic ray spectrum above 4 $\times 10^{18}$ eV using inclined events detected with the Pierre Auger Observatory. J. Cosmology Astropart. Phys., 8:049, August 2015.

[71] Pierre Auger Collaboration, J. Abraham, P. Abreu, M. Aglietta, C. Aguirre, D. Allard, I. Allekotte, J. Allen, P. Allison, C. Alvarez, and et al. Correlation of the Highest-Energy Cosmic Rays with Nearby Extragalactic Objects. *Science*, 318:938, November 2007.

[72] Planck Collaboration, P. A. R. Ade, N. Aghanim, M. Arnaud, M. Ashdown, J. Aumont, C. Baccigalupi, A. J. Banday, R. B. Barreiro, J. G. Bartlett, and et al. Planck 2015 results. XIII. Cosmological parameters. A&A, 594:A13, September 2016.

[73] M. Plum and for the Pierre Auger Collaboration. Measurement of the chemical composition of the ultra-high-energy cosmic rays with the Pierre Auger Observatory. *ArXiv e-prints*, January 2015.

[74] F. Reines, C. L. Cowan, F. B. Harrison, A. D. McGuire, and H. W. Kruse. Detection of the free antineutrino. *Phys. Rev.*, 117:159–173, Jan 1960.

[75] C. Rojas-Bravo and M. Araya. Search for gamma-ray emission from star-forming galaxies with Fermi LAT. MNRAS, 463:1068–1073, November 2016.

[76] G. B. Rybicki and A. P. Lightman. *Radiative Processes in Astrophysics*. June 1986.

[77] D. Sanders. Luminous infrared galaxies, 1996.

[78] D. B. Sanders, J. M. Mazzarella, D.-C. Kim, J. A. Surace, and B. T. Soifer. The IRAS Revised Bright Galaxy Sample. AJ, 126:1607–1664, October 2003.

[79] K. Scholberg. The SuperNova Early Warning System. *Astronomische Nachrichten*, 329:337, March 2008.

[80] K. Sekiguchi. IRAS observations of starburst and nonactive spiral galaxies. *The Astrophysical Journal*, 316:145–152, May 1987.

[81] Telescope Array Collaboration, T. Abu-Zayyad, R. Aida, M. Allen, R. Anderson, and R. et al. Azuma. The Cosmic-Ray Energy Spectrum Observed with the Surface Detector of the Telescope Array Experiment. ApJ, 768:L1, May 2013.

[82] The IceCube Collaboration, M. G. Aartsen, R. Abbasi, M. Ackermann, J. Adams, J. A. Aguilar, M. Ahlers, D. Altmann, C. Arguelles, T. C. Arlen, and et al. Search for a diffuse flux of astrophysical muon neutrinos with the IceCube 59-string configuration. *ArXiv e-prints*, November 2013.

[83] The IceCube-Gen2 Collaboration, :, M. G. Aartsen, K. Abraham, M. Ackermann, J. Adams, J. A. Aguilar, M. Ahlers, M. Ahrens, D. Altmann, and et al. IceCube-Gen2 - The Next Generation Neutrino Observatory at the South Pole: Contributions to ICRC 2015. *ArXiv e-prints*, October 2015.

[84] The Super-Kamiokande Collaboration. Search for nucleon decay into charged antilepton plus meson in 0.316 megaton·years exposure of the Super-Kamiokande water Cherenkov detector. *ArXiv e-prints*, May 2017.

[85] M.-P. Véron-Cetty and P. Véron. A catalogue of quasars and active nuclei: 13th edition. A&A, 518:A10, July 2010.

[86] Francesco Vissani and Francesco Lorenzo Villante. Cosmic rays and neutrinos from supernova remnants. *Nuclear Instruments and Methods in Physics Research Section A: Accelerators, Spectrometers, Detectors and Associated Equipment*, 588(1):123 – 129, 2008. Proceedings of the First International Conference on Astroparticle Physics.

[87] A. Watanabe. The spectrum and flavor composition of the astrophysical neutrinos in IceCube. J. Cosmology Astropart. Phys., 8:030, August 2015.

[88] E. Waxman. The origin of IceCube's neutrinos: Cosmic ray accelerators embedded in star forming calorimeters. *ArXiv e-prints*, November 2015.

[89] E. Waxman and J. Bahcall. High energy neutrinos from astrophysical sources: An upper bound. Phys. Rev. D, 59(2):023002, January 1999.

[90] T. M. Yoast-Hull, J. S. Gallagher, III, E. G. Zweibel, and J. E. Everett. Active Galactic Nuclei, Neutrinos, and Interacting Cosmic Rays in NGC 253 and NGC 1068. *The Astrophysical Journal*, 780:137, January 2014.

[91] G. T. Zatsepin and V. A. Kuz'min. Upper Limit of the Spectrum of Cosmic Rays. *Soviet Journal of Experimental and Theoretical Physics Letters*, 4:78, August 1966.